

Copyright
By
Wendy-Angela S. Agata
2021

Layer-by-Layer Synthesis of Polyamide Thin Film Composite Membranes for Desalination Applications

A Dissertation

Presented to the Faculty of the School of Engineering and Applied Science at the
University of Virginia

In Partial Fulfillment of the Requirements for the Degree of
Doctor of Philosophy in Chemical Engineering

By

Wendy-Angela S. Agata

July 2021

**The Dissertation Committee for Wendy-Angela Agata Certifies that this is the Approved
Version of the Following Dissertation:**

**Layer-by-Layer Synthesis of Polyamide Thin Film Composite
Membranes for Desalination Applications**

Committee:

Geoffrey M. Geise, Dissertation Advisor

Rachel Letteri

David L. Green

Gaurav Giri

William S. Epling

Dedication

To everyone who have supported me on my journey pursuing a Ph.D.– this is for you.

Acknowledgements

Throughout this journey towards a PhD I have had considerable support. There have been many triumphs, as well as downfalls during my pursuit of this degree and at times I felt as though I could not continue. However, it is through the tremendous support of the people below that I am at the position where I am able to not only sow the seeds of my labor but profusely thank all the wonderful people who have been instrumental in my success.

I would first like to thank Dr. Geoffrey Geise for reading my, definitely lengthy, application and advocating for my acceptance into the UVA Chemical Engineering PhD program. I had a lot of growing up to do, both personally and professionally, I have to attribute a large chunk of that to his dedication and persistence to get the best researcher out of me. The high standards he holds for himself and the group in its entirety regularly pushed me to do that additional experiment or read that extra paper on the days that it was a bit harder to push forward. I would also like to acknowledge the following funding sources that helped to support my dissertation research. This material is based upon work supported in part by the National Science Foundation under Grant Numbers CBET-1752048 and CMMI-2001624, the Virginia Space Grant Consortium, and the National GEM Consortium.

Next, I would like to thank the mentors I have found during my time at UVA, Dr. Shannon Barker and Dr. Amy Clobes. I found regular solace in the recruitment activities I did for the university both as a way to refresh my mind from research and a constant reminder of why I am a scientist. More importantly, though, I found fervent support and comradery from you both at times I reached a cross-roads in my research or the inevitable moments where imposter syndrome set in and I did not understand how to proceed. Thank you for your guidance both

personally and professionally and for reminding me that there is always another opportunity around the corner, even when it doesn't seem that way.

Next, I want to thank my fiancé, Ryan Moss. Though I have only known you for a portion of my PhD experience, you came into my life at a time when I really needed to remember my own strength. Your highly inquisitive mind forced me to question everything around me, reminding me of my love of understanding the unknown. Coupled with your kind but tough love, I was reminded of why I love science and that when times get difficult I must be resourceful and only focus on what I can change – the rest is just a distraction. Thank you and I can't wait to marry you next year!

Last, but certainly not least, I must thank my family. My mother's listening ear and truly infinite patience allowed me to work through all my professional frustrations as I pursued this area of uncharted waters. My brother's regular visits to my tiny Charlottesville apartment regularly brought me joy at the toughest times as he'd do his "dog uncle" duties to provide me a little extra time in the lab. Finally, my father's persistence in his own scientific career and unwavering support of mine always reminded me that not only does he have my back but that I will get it done because it "must get done." Dad, as I promised – here are the **results**.

Abstract

Understanding how polymer backbone structure effects water and salt transport is an essential part of designing efficient desalination membranes. Current commercialized ion exchange membranes contribute to the high cost of desalination process through both expensive synthesis processes and low energy efficiencies. Through the addition of selective fillers or fixed charge groups to well understood polyamide (PA)-based thin-film composite reverse osmosis membranes, we aim to take advantage of their low resistance while introducing Donnan exclusion or size sieving to facilitate the selective removal of impurities. We aim to shift “layer-by-layer” deposition of m-phenylenediamine and trimesoyl chloride onto microporous supports for composite membrane formation by priming supports with polyvinyl alcohol to seal defects formed in the PA layer as well as protect these polysulfone-based supports from continued organic solvent exposure. The application of layer-by-layer synthesis of selective polyamide layers will then be assessed for extension to both the incorporation of fixed charge groups, via the addition of a sulfonated co- monomer, as well nanofillers, via the addition of UiO66-NH₂, a metal organic framework. Water and solute transport information for the various composite membranes studied will be analyzed using a resistance in series model to elucidate key structure/property relationships important for further optimization of the polyamide layer for more efficient desalination.

Table of Contents

Chapter 1: Introduction

- 1.1. Water/Energy Nexus
- 1.2. Goals of Dissertation
- 1.3. References

Chapter 2: Background

- 2.1. Polyamide Thin Film Composite Membranes in Reverse Osmosis
- 2.2. Layer-by-Layer (LbL) Synthesis in Polymeric Membranes
- 2.3. Knowledge Gap
- 2.4. References

Chapter 3: Theoretical Methods

- 3.1. Solution-Diffusion Model
- 3.2. Resistance-in-Series Model
 - 3.2.1. Water Transport
 - 3.2.2. Salt Transport
- 3.3. References

Chapter 4: Materials and Methods

- 4.1. Layer-by-Layer Polymer Membranes
 - 4.1.1. PVA-Primed Substrate Preparation
 - 4.1.2. PA Selective Layer
 - 4.1.2.1. MPD/TMC-based PA Synthesis
 - 4.1.2.2. Sulfonated PA Synthesis
 - 4.1.2.3. UiO-66 NH₂ incorporated PA Synthesis
- 4.2. Electrolytes and Dyes
- 4.3. Experimental Methods
 - 4.3.1. Membrane and UiO-66 NH₂ Characterization
 - 4.3.1.1. Profilometry
 - 4.3.1.2. Atomic Force Microscopy (AFM)
 - 4.3.1.3. Scanning Electron Microscopy (SEM)
 - 4.3.1.4. BET Analysis
 - 4.3.1.5. X-Ray Diffraction (XRD)
 - 4.3.1.6. Thermogravimetric Analysis (TGA)
 - 4.3.1.7. Fourier Transfer Infrared Spectroscopy (FTIR)
 - 4.3.2. Performance Tests
 - 4.3.2.1. Water and Salt Transport
 - 4.3.2.2. Ionic Conductivity

4.3.2.3. Dye Rejection

4.4. References

Chapter 5: Layer-by-Layer Approach to Enable Polyamide Formation on Microporous Supports for Thin-Film Composite Membranes

5.1. Introduction

5.2. Results and Discussion

5.2.1. Growth Rate and Surface Roughness

5.2.2. Water Transport

5.2.3. Salt Transport and Water/Salt Selectivity

5.2.4. Charged Co-Monomer Incorporation

5.3. Conclusions

5.4. References

Chapter 6: Layer-by-Layer “Sandwiched” Synthesis of UiO66-NH₂- containing Polyamide Thin-Film Nanocomposite Membranes for Nanofiltration Applications

6.1. Introduction

6.2 Results and Discussion

6.2.1. UiO66-NH₂ Characterization

6.2.2. PA-TFN Characterization

6.2.3. Water Transport

6.2.4. Salt Transport and Permeability/Selectivity Tradeoff

6.2.5. Dye Rejection

6.2.6. Water/Solute Selectivity

6.2.7. Application of Resistance in Series Model and PVA Primer Layer Contribution to Mass Transfer of Water

6.3. Conclusions

6.4. References

Chapter 7: Conclusions and Recommendations

7.1. Conclusions

7.2. Significance

7.3. Recommendations for Future Work

7.4. References

Appendix A: List of Symbols

Appendix B: Supporting Information for Chapter 5

B.1. Discussion of Methanol and Acetone as Final Rinse Solvents

B.2. Data Summary

B.3. Dependence of the Overall Water Permeance on the Number of LbL Cycles

B.4. Analysis of Relative Mass Transfer Resistances (Water Transport)

B.5. Analysis of Relative Mass Transport Resistances (Salt Transport)

B.6. References

Appendix C: Supporting Information for Chapter 6

- C.1. Determining the MOF Loading in wt% via TGA
- C.2. Data Summary
- C.3. Series Resistance Model for Water Transport
- C.4. Determination of PVA Layer Contribution to Resistance to Water Transport
- C.5. References

Vita

Chapter 1: Introduction

1.1. Water/Energy Nexus

Approximately 2.3 billion people live without access to a consistent clean water supply.¹⁻
³ Researchers anticipate that this issue is going to become more prevalent as the population grows and subsequent economic development takes place. Though water scarcity is most commonly expected in naturally water-stricken areas, like deserts, high population areas of developing countries in Africa and the Middle East also fall into this category.¹⁻³ As it is predicted that 90% of the additional population will be in developing countries, the concern for more efficient desalination becomes even more pressing.^{2,3}

Large scale desalination techniques are typically divided into four categories: precipitation and coagulation, distillation, adsorption, and membrane-based separations. Of these, membrane-based separation tends to be preferred as it is energy efficient, has a small environmental footprint and is cost-effective.¹⁻³ However, it is hindered by membrane fouling, a result of the interaction between the polymer membrane separator and common desalination additives, and a permeability/selectivity tradeoff that results in difficulty maintaining high impurity rejection as well as high water permeance.^{2,3}

Within the membrane-based class of desalination processes, there are pressure-driven and electrically driven processes, each defined by their driving force for transport.^{2,4} For pressure-driven desalination, membrane-based desalination techniques are classified based on the size of solutes they are aimed to reject. Solutes of interest range greatly from monovalent/small divalent ions ($\sim 10^{-4} \mu m$) typically highly rejected by reverse osmosis membranes to bacteria and pollens ($\sim 10^2 \mu m$) typically rejected by conventional filtration membranes.² More specifically, the most common pressure-driven desalination techniques under this umbrella, reverse osmosis and nanofiltration, filter out solutes range 1-2 orders of magnitude in size yet have the same leading

membrane technology, the polyamide thin film composite membrane (PA-TFC).^{4,5} The thin selective polyamide layer atop a porous support allows for individual tuning of the layers based on the specific water and solute transport needs of the application. Membrane separators used in this class of desalination processes are thus designed to be high salt rejecting but also benefit from low resistance to provide the opportunity at challenging the water permeability/selectivity tradeoff.^{2-4,6} Understanding structure-property relationships of the polymer as they relate to the water and salt transport, allows us to interrogate this permeability/selectivity tradeoff for our desalination processes of interest as we make changes to the way the polymer is synthesized.^{2,4,6} More specifically gaining insight on the polyamide layer specific contribution to these structure-property relationships could provide a more specific tie between the synthesis and the performance further streamlining optimization of the membrane towards is specific applications.

5

This research study focusses on applying a layer-by-layer synthesis to the well-known polyamide thin film composite (PA-TFC) membrane to allow for easier incorporation of additional reactants (i.e. nanofillers and fixed charge groups). Through greater control of the growth of the polyamide layer, a more predictable incorporation of fixed charge groups and metal organic frameworks can be performed to introduce more interesting ion transport pathways for expansion of the PA-TFC membrane framework to other desalination applications.⁶⁻⁸

1.2. Goals and Organization of the Dissertation

The goal of this work is to show how layer-by-layer (LbL) synthesis of an aromatic polyamide for composite membrane formation allows for the incorporation of additional reactants that provide more interesting ion transport pathways. As this process has been mostly studied for the deposition of the polyamide layer to glass or silicon slides, we show how the use

of a polyvinyl alcohol (PVA) primer layer on a microporous support provides a reactive surface for the synthesis to take place as well as seals defects present within the polyamide layer when formed on a bare support. To ascertain the efficacy of this synthesis method, water permeance and salt rejection for these LbL-made membranes is compared to that of commercial RO membranes. Next, a sulfonated diamine is introduced to the reaction scheme using LbL and the incorporation of fixed charge groups into the PA layer is assessed using in-plane conductivity measurements. Finally, this procedure is applied in a “sandwich” reaction scheme to fully incorporate UiO-66-NH₂, a metal organic framework (MOF), into the polyamide layer and the water, salt, and dye transport of the PA layer is determined. These performance metrics will be used to determine how the addition of nanofillers, with fixed pore size, allows for a shift in the water/solute selectivity regime of the membrane.

This dissertation is composed of seven total chapters. Chapter 1 provides the broader impact context of this work for improved membrane design for enhanced desalination efficiency to address global water shortage issues. Chapter 2 reviews key background on PA-TFC membranes, our membrane system of interest, LbL synthesis of polymeric membranes, and the knowledge gaps we aim address with this work. Chapter 3 covers solution-diffusion and resistance-in-series, theoretical transport models that allow us to draw structure-property relationships between our LbL-made PA layers and key water/salt transport metrics. Chapter 4 describes the LbL synthesis method used in this work for baseline aromatic PA layers, sulfonated PA layers, and MOF-incorporated PA layers. Further, the characterization of the PA layers and the MOF are presented and the water, salt and dye transport performance metrics are described.

In order to apply LbL synthesis to the synthesis of PA layers with fixed charge groups and nanofillers, the method had to be successfully performed on microporous supports for

baseline aromatic PA layers. Chapter 5 evaluates the efficacy of this synthesis procedure for composite membrane formation through determining the bare support and PVA-primed support water and salt performance of LbL-made PA-TFC membranes. Further, the mass transfer resistance of the PVA primer is determined to confirm that the PA layer dictates the water and salt transport of the composite membrane. Finally, the incorporation of a sulfonated diamine is confirmed using in-plane conductivity measurements.

Chapter 6 evaluates the use of a “sandwich” LbL-based synthesis method to ensure incorporation of UiO66-NH₂ into the PA layer as well as ascertain the effect of nanofillers on the water, salt, and dye transport of the PA layer. This information qualitatively informs how the addition of size-sieving by the MOFs to the solution-diffusion transport mechanism of PA layer effects the membranes ability to selectivity remove larger solutes. Finally, Chapter 7 contains overall conclusions and future recommendations for extending this work motivated by this dissertation. Appendix A will cover the nomenclature used in this dissertation while Appendices B and C will contain the supporting discussions for Chapters 5 and 6 respectively.

1.3. References

- (1) Vörösmarty, C. J.; McIntyre, P. B.; Gessner, M. O.; Dudgeon, D.; Prusevich, A.; Green, P.; Glidden, S.; Bunn, S. E.; Sullivan, C. A.; Liermann, C. R.; Davies, P. M. Global Threats to Human Water Security and River Biodiversity. *Nature* **2010**, *467* (7315), 555–561. <https://doi.org/10.1038/nature09440>.
- (2) Geise, G. M.; Lee, H.-S.; Miller, D. J.; Freeman, B. D.; McGrath, J. E.; Paul, D. R. Water Purification by Membranes: The Role of Polymer Science. *J. Polym. Sci. Part B Polym. Phys.* **2010**, *48*, 1685–1711. <https://doi.org/10.1002/polb.22037>.
- (3) Ali, A.; Tufa, R. A.; Macedonio, F.; Curcio, E.; Drioli, E. Membrane Technology in Renewable-Energy-Driven Desalination. *Renewable and Sustainable Energy Reviews*. 2018, pp 1–21. <https://doi.org/10.1016/j.rser.2017.07.047>.
- (4) Geise, G. M.; Park, H. B.; Sagle, A. C.; Freeman, B. D.; McGrath, J. E. Water Permeability and Water/Salt Selectivity Tradeoff in Polymers for Desalination. *J. Memb. Sci.* **2011**, *369* (1–2), 130–138. <https://doi.org/10.1016/j.memsci.2010.11.054>.
- (5) Agata, W.-A. S.; Thompson, J.; Geise, G. M. Layer-by-Layer Approach to Enable Polyamide Formation on Microporous Supports for Thin-Film Composite Membranes. *J. Appl. Polym. Sci.* *n/a* (n/a), 51201. <https://doi.org/https://doi.org/10.1002/app.51201>.

- (6) Luo, H.; Agata, W.-A. S.; Geise, G. M. Connecting the Ion Separation Factor to the Sorption and Diffusion Selectivity of Ion Exchange Membranes. *Ind. Eng. Chem. Res.* **2020**. <https://doi.org/10.1021/acs.iecr.0c02457>.
- (7) Choi, W.; Gu, J. E.; Park, S. H.; Kim, S.; Bang, J.; Baek, K. Y.; Park, B.; Lee, J. S.; Chan, E. P.; Lee, J. H. Tailor-Made Polyamide Membranes for Water Desalination. *ACS Nano* **2015**, *9* (1), 345–355. <https://doi.org/10.1021/nn505318v>.
- (8) Gu, J. E.; Lee, S.; Stafford, C. M.; Lee, J. S.; Choi, W.; Kim, B. Y.; Baek, K. Y.; Chan, E. P.; Chung, J. Y.; Bang, J.; Lee, J. H. Molecular Layer-by-Layer Assembled Thin-Film Composite Membranes for Water Desalination. *Adv. Mater.* **2013**, *25* (34), 4778–4782. <https://doi.org/10.1002/adma.201302030>.

Chapter 2: Background

2.1. Polyamide Thin Film Composite Membranes in Reverse Osmosis

Polymer membranes for water purification and energy applications must be both thin and selective to minimize mass transfer resistance and maximize separation efficiency. One of the most commercially successful examples is the polyamide thin-film composite (PA-TFC) membrane used for desalination.¹⁻¹² These membranes are manufactured to feature a thin (order 100 nm) dense polyamide (PA) film that promotes water transport while minimizing salt transport.^{1,2,11,12,3-10} PA-TFC membranes are applied to both reverse osmosis and nanofiltration desalination processes. Reverse osmosis (RO) based PA-TFCs are typically made with an aromatic diamine, like m-phenylenediamine (MPD), and nanofiltration (NF) based PA-TFCs are synthesized using a linear diamine, like piperazine. Coupled with an acyl chloride, both reaction schemes yield polyamides with differing water permeance and salt rejection standards based on requirements for their application.^{1,13-16}

Though the performance of all desalination membranes is dictated by the ability to transport water sufficiently and reject impurities well, the standards based on the application differ and, as was mentioned earlier, an upper bound is reached for all membranes where at a certain water permeance, water/salt selectivity ceases to increase. Yang and coworkers were able to establish this upper bound for membrane permeability versus selectivity for desalination and highlight the performance regimes for RO and NF. Modeled off Robeson's inaugural upper bound for gas separation membranes, a log-log comparison of the water/salt permeance selectivity versus the water permeance for over three hundred RO and NF PA-TFC membranes, both commercial and in-house made, was used to develop the upper bound for desalination membranes. The upper bound for RO and NF desalination membranes acts as a standard

reference and guide for expected water and salt performance based on the application. With a continued understanding of structure-property relationships for PA-TFCs, a path is created to push against or even past this upper bound.

The RO-based PA layer typically is synthesized by interfacial polymerization (IP) of *m*-phenylenediamine (MPD) and a tri-functional acid chloride, trimesoyl chloride (TMC) that is dependent on fast reactivity of amines with acyl chlorides.¹⁷ The reaction is self-limiting, and the structure of the PA layer is primarily dictated by the reactivity, solubility, and diffusivity of the monomers.^{1,2,5-11} The IP reaction is fast, so solubility and diffusivity factors often control diamine transport to the reaction zone.^{3,4,12} As such, co-monomers with lower solubility and/or diffusivity compared to MPD may not incorporate in the PA layer prepared via IP.

2.2. Layer-by-Layer Synthesis in Polymeric Membranes

The LbL process was adopted for PA layer formation based on layer-by-layer assembly of polyelectrolytes. [9] In the context of polyamide desalination membranes, LbL can be used to deposit monomers onto the surface where a polycondensation reaction occurs to form a cross-linked PA network (**Figure 1**).^{3,4,10,11} Since LbL PA layer formation does not require the liquid-liquid interface that occurs in conventional IP, smoother membranes can be made compared to those prepared via IP because the LbL process brings monomers to the surface in a controlled manner. Smoother membranes often have advantages in applications due to, for example, reduced fouling propensity.^{1,2,11,12,3-10}

The inaugural work on molecular layer-by-layer deposition of PA layers by Johnson and coworkers shows that through this spin coater-based deposition technique, PA layers can be grown effectively monolayer by monolayer.¹⁰ With this level of controlled synthesis, the thickness of the PA layer can be determined directly using tapping profilometry and the smooth,

highly-crosslinked polyamide structure can be obtained.¹⁰ In addition to an automation of the molecular layer-by-layer process, Stafford and colleagues expanded this work to deposition onto polyelectrolyte-coated microporous supports.^{3,11,18} As the PA layer thickness is known, a resistance-in-series solution diffusion model was used to determine the PA layer specific water and salt permeability.^{3,18} Overall, this preliminary highlights the ability to remove the dependence of diffusion to the interface via a sequential deposition process as well as introduces a greater control of the PA layer growth.^{3,4,11,12,18,19}

2.3. Knowledge Gaps

Several challenges exist in gaining greater control of PA layer formation in an effort to introduce different ion transport properties. The first is that the most commonly used synthesis technique for PA formation, interfacial polymerization (IP), depends on many reaction parameters making it difficult to control. Further, the preliminary work on the more controlled LbL PA layer synthesis is predominantly on nonporous supports providing few reference points for the efficacy of this procedure for PA-TFC membrane production.

Shifting to the more controlled layer-by-layer sequential deposition process allows for the removal of the dependence on diamine diffusion to the reaction zone for dense PA layer formation. Previously to improve the efficacy of the IP reaction, researchers have varied the porous support, post-synthesis processing (i.e. heat curing, additives etc.), and manipulated the diamine concentration and/or reactivity.^{4,5,19–21} In Freger's commonly referenced schematic of the IP polycondensation reaction, the interface is located slightly more in the organic acyl chloride solution, rather than directly at its meeting point with the aqueous diamine solution.² Within this framework, the diffusion of the diamine is a key factor in determining the efficacy of the IP reaction as it must travel further to the interface than the acyl chloride – this is why the

diamine is typically in excess during IP. Layer-by-layer synthesis circumvents this dependence on the diamine diffusion by dissolving all monomers in the same dry organic solvent and alternatively depositing them to the substrate of interest.^{3,4,11} As TMC and MPD are highly reactive, the removal of this diffusion limitation allows for control of the chemistry of the PA film at the monomer length scale.

The preliminary work on layer-by-layer synthesis of PA on glass and silicon substrates has confirmed the ability to make smooth, defect free PA layers with known thickness.^{10,11} However, few papers have extended this same spin-coater based process to deposition on microporous supports. Further, the work that extends a similar sequential deposition technique to polyelectrolyte-coated supports, do not assess the contribution of the support coating to the overall mass transfer resistance of the composite membrane.^{3,4} The deposition of MPD/TMC-based PA layers using a layer-by-layer sequential spin coater-based synthesis on PVA primed supports discussed in this dissertation addresses this knowledge gap by assessing the comparative performance of bare support and PVA-primed LbL synthesized PA-TFCs. Further, the mass transfer resistance contribution of the PVA primer layer is assessed through a resistance-in-series model.

Though, sequential deposition techniques have been used to deposit PA layers with both linear and aromatic diamines, a second knowledge gap exists in the application of this spin coater-based process with additional reactants (i.e. charged monomers and nanofillers) that could provide more interesting ion transport pathways.⁴ Ion exchange membranes, polymer membranes containing either fixed negative (CEMs) or fixed positive (AEM) charge groups, are used in a variety of desalination applications. The presence of fixed charge groups allows them to take advantage of Donnan exclusion, the electrostatic repulsion of fixed charge groups and solution

ions, for improved salt rejection for nanofiltration, or facilitate ionic current, for improved efficiency and impurity removal for electrodialysis. Sulfonation of the PA layer has been successfully performed previously using IP through the use of PIP as a co-monomer to a sulfonated diamine or by replacing PIP or MPD with a bulky sulfonated diamine. However, there is little discussion on the effect of sulfonation on the PA layer specific ionic conductivity, a key parameter for electrically driven desalination applications.^{19,22–24} Through-plane analysis of layer-by-layer grown sulfonated PA layers on PVA-coated commercial CEMs will help in closing this knowledge gap as the known thickness of the PA layer and high ionic resistance of the PVA coating allows for the direct determination of ionic conductivity due to sulfonation.

In addition to fixed charge groups, there is an opportunity to expand this layer-by-layer sequential deposition process to the formation of thin-film nanocomposite membranes (TFNs). The addition of nanocomposites to the composite membrane framework allows for additional transport pathways to be introduced via the fixed pores within the MOF.^{25–31} A key shortcoming lies in the complete incorporation of the MOF into the PA-TFN structure as the typical 100-300 nm size of most MOFs is larger than the desired ~100 nm thickness of the PA layer.^{25,26,28,31} This is commonly addressed by either attempting to make smaller MOFs, incorporating MOFs into the ~10² μm thick microporous support, or incorporating an additional MOF sheet to the composite membrane structure.^{25,26,28,30,31} A modified “sandwiched” layer-by-layer synthesis procedure of PA-TFN membranes with UiO66-NH₂ of significantly smaller size (~20-50 nm) will address this knowledge gap by instituting MOF incorporation between two “layers” of PA. MOF incorporation is also encouraged by the added reactivity and size tuning available with the recently developed aqueous based UiO66-NH₂ synthesis technique by our collaborators.^{32,33} Attempting to add a smaller MOF to a dense PA layer of controllable thickness provides the

opportunity to similarly understand the contribution of the modified PA layer itself through a resistance in series model.²⁵ Evidence of reasonably controlled PA-TFN membrane growth in this way could therefore provide a framework for understanding how water, salt and other impurities move through the MOF embedded in the dense PA film.^{17,25,34,35} The application of a LbL “sandwiched” synthesis of a UiO66-NH₂ incorporated PA layer on a PVA-primed support address this knowledge gap by determining not only through the water and solute transport of composite membranes made with varying MOF loading, but by assessing these results in the context of a resistance in series model to ascertain the majority contribution of the PA layer to the composite resistance to mass transfer. With this information, we are able to elucidate important, PA layer specific structure/property relationships that inform further optimization of this process for NF applications.

2.4. References

- (1) Geise, G. M.; Lee, H.-S.; Miller, D. J.; Freeman, B. D.; McGrath, J. E.; Paul, D. R. Water Purification by Membranes: The Role of Polymer Science. *J. Polym. Sci. Part B Polym. Phys.* **2010**, *48*, 1685–1711. <https://doi.org/10.1002/polb.22037>.
- (2) Freger, V. Kinetics of Film Formation by Interfacial Polycondensation. *Langmuir* **2005**, *21* (5), 1884–1894. <https://doi.org/10.1021/la048085v>.
- (3) Gu, J. E.; Lee, S.; Stafford, C. M.; Lee, J. S.; Choi, W.; Kim, B. Y.; Baek, K. Y.; Chan, E. P.; Chung, J. Y.; Bang, J.; Lee, J. H. Molecular Layer-by-Layer Assembled Thin-Film Composite Membranes for Water Desalination. *Adv. Mater.* **2013**, *25* (34), 4778–4782. <https://doi.org/10.1002/adma.201302030>.
- (4) Choi, W.; Gu, J. E.; Park, S. H.; Kim, S.; Bang, J.; Baek, K. Y.; Park, B.; Lee, J. S.; Chan, E. P.; Lee, J. H. Tailor-Made Polyamide Membranes for Water Desalination. *ACS Nano* **2015**, *9* (1), 345–355. <https://doi.org/10.1021/nn505318v>.
- (5) Kong, C.; Shintani, T.; Kamada, T.; Freger, V.; Tsuru, T. Co-Solvent-Mediated Synthesis of Thin Polyamide Membranes. *J. Memb. Sci.* **2011**, *384* (1–2), 10–16. <https://doi.org/10.1016/j.memsci.2011.08.055>.
- (6) Saha, N. K.; Joshi, S. V. Performance Evaluation of Thin Film Composite Polyamide Nanofiltration Membrane with Variation in Monomer Type. *J. Memb. Sci.* **2009**, *342* (1–2), 60–69. <https://doi.org/10.1016/j.memsci.2009.06.025>.
- (7) Ghosh, A. K.; Jeong, B. H.; Huang, X.; Hoek, E. M. V. Impacts of Reaction and Curing Conditions on Polyamide Composite Reverse Osmosis Membrane Properties. *J. Memb.*

- Sci.* **2008**, *311* (1–2), 34–45. <https://doi.org/10.1016/j.memsci.2007.11.038>.
- (8) Ahmad, A. L.; Ooi, B. S. Properties-Performance of Thin Film Composites Membrane: Study on Trimesoyl Chloride Content and Polymerization Time. *J. Memb. Sci.* **2005**, *255* (1–2), 67–77. <https://doi.org/10.1016/j.memsci.2005.01.021>.
- (9) Hermans, S.; Bernstein, R.; Volodin, A.; Vankelecom, I. F. J. Study of Synthesis Parameters and Active Layer Morphology of Interfacially Polymerized Polyamide-Polysulfone Membranes. *React. Funct. Polym.* **2015**, *86*, 199–208. <https://doi.org/10.1016/j.reactfunctpolym.2014.09.013>.
- (10) Johnson, P. M.; Yoon, J.; Kelly, J. Y.; Howarter, J. A.; Stafford, C. M. Molecular Layer-by-Layer Deposition of Highly Crosslinked Polyamide Films. *J. Polym. Sci. Part B Polym. Phys.* **2012**, *50* (3), 168–173. <https://doi.org/10.1002/polb.23002>.
- (11) Chan, E. P.; Lee, J. H.; Chung, J. Y.; Stafford, C. M. An Automated Spin-Assisted Approach for Molecular Layer-by-Layer Assembly of Crosslinked Polymer Thin Films. *Rev. Sci. Instrum.* **2012**, *83* (11). <https://doi.org/10.1063/1.4767289>.
- (12) Chowdhury, M. R.; Steffes, J.; Huey, B. D.; McCutcheon, J. R. 3D Printed Polyamide Membranes for Desalination. *Science (80-.)*. **2018**, *361* (6403), 682–686. <https://doi.org/10.1126/science.aar2122>.
- (13) Yang, Z.; Guo, H.; Tang, C. Y. The Upper Bound of Thin-Film Composite (TFC) Polyamide Membranes for Desalination. *J. Memb. Sci.* **2019**. <https://doi.org/10.1016/j.memsci.2019.117297>.
- (14) Fridman-Bishop, N.; Freger, V. What Makes Aromatic Polyamide Membranes Superior: New Insights into Ion Transport and Membrane Structure. *J. Memb. Sci.* **2017**, *540*, 120–128. <https://doi.org/10.1016/j.memsci.2017.06.035>.
- (15) Eriksson, P. Water and Salt Transport through Two Types of Polyamide Composite Membranes. *J. Memb. Sci.* **1988**. [https://doi.org/10.1016/0376-7388\(88\)80024-3](https://doi.org/10.1016/0376-7388(88)80024-3).
- (16) Gohil, J. M.; Ray, P. A Review on Semi-Aromatic Polyamide TFC Membranes Prepared by Interfacial Polymerization: Potential for Water Treatment and Desalination. *Separation and Purification Technology*. 2017. <https://doi.org/10.1016/j.seppur.2017.03.020>.
- (17) Geise, G. M. Why Polyamide Reverse-Osmosis Membranes Work so Well. *Science (80-.)*. **2021**. <https://doi.org/10.1126/science.abe9741>.
- (18) Chan, E. P.; Young, A. P.; Lee, J. H.; Stafford, C. M. Swelling of Ultrathin Molecular Layer-by-Layer Polyamide Water Desalination Membranes. *J. Polym. Sci. Part B Polym. Phys.* **2013**. <https://doi.org/10.1002/polb.23380>.
- (19) Xie, W.; Geise, G. M.; Freeman, B. D.; Lee, H. S.; Byun, G.; McGrath, J. E. Polyamide Interfacial Composite Membranes Prepared from M-Phenylene Diamine, Trimesoyl Chloride and a New Disulfonated Diamine. *J. Memb. Sci.* **2012**, *403–404*, 152–161. <https://doi.org/10.1016/j.memsci.2012.02.038>.
- (20) Mansourpanah, Y.; Madaeni, S. S.; Rahimpour, A. Fabrication and Development of Interfacial Polymerized Thin-Film Composite Nanofiltration Membrane Using Different Surfactants in Organic Phase; Study of Morphology and Performance. *J. Memb. Sci.* **2009**.

- <https://doi.org/10.1016/j.memsci.2009.07.033>.
- (21) Li, M.; Lv, Z.; Zheng, J.; Hu, J.; Jiang, C.; Ueda, M.; Zhang, X.; Wang, L. Positively Charged Nanofiltration Membrane with Dendritic Surface for Toxic Element Removal. *ACS Sustain. Chem. Eng.* **2017**, *5* (1), 784–792. <https://doi.org/10.1021/acssuschemeng.6b02119>.
- (22) Akbari, A.; Aliyarizadeh, E.; Mojallali Rostami, S. M.; Homayoonfal, M. Novel Sulfonated Polyamide Thin-Film Composite Nanofiltration Membranes with Improved Water Flux and Anti-Fouling Properties. *Desalination* **2016**. <https://doi.org/10.1016/j.desal.2015.08.025>.
- (23) Liu, H.; Zhang, M.; Zhao, H.; Jiang, Y.; Liu, G.; Gao, J. Enhanced Dispersibility of Metal–Organic Frameworks (MOFs) in the Organic Phase via Surface Modification for TFN Nanofiltration Membrane Preparation. *RSC Adv.* **2020**, *10* (7), 4045–4057. <https://doi.org/10.1039/C9RA09672H>.
- (24) Deligöz, H.; Vatansever, S.; Öksüzömer, F.; Koç, S. N.; Özgümüş, S.; Gürkaynak, M. A. Synthesis and Characterization of Sulfonated Homo- and Co-Polyimides Based on 2,4 and 2,5-Diaminobenzenesulfonic Acid for Proton Exchange Membranes. *Polym. Adv. Technol.* **2008**. <https://doi.org/10.1002/pat.1196>.
- (25) Ng, Z. C.; Lau, W. J.; Matsuura, T.; Ismail, A. F. Thin Film Nanocomposite RO Membranes: Review on Fabrication Techniques and Impacts of Nanofiller Characteristics on Membrane Properties. *Chem. Eng. Res. Des.* **2021**, *165*, 81–105. <https://doi.org/10.1016/j.cherd.2020.10.003>.
- (26) Wen, Y.; Zhang, X.; Li, X.; Wang, Z.; Tang, C. Y. Metal-Organic Framework Nanosheets for Thin-Film Composite Membranes with Enhanced Permeability and Selectivity. *ACS Appl. Nano Mater.* **2020**. <https://doi.org/10.1021/acsanm.0c01860>.
- (27) Bagherzadeh, M.; Bayrami, A.; Amini, M. Thin-Film Nanocomposite Forward Osmosis Membranes Modified with Zr-Based Metal–Organic Framework to Improve Desalination Performance. *Appl. Organomet. Chem.* **2020**. <https://doi.org/10.1002/aoc.5339>.
- (28) Gong, Y.; Gao, S.; Tian, Y.; Zhu, Y.; Fang, W.; Wang, Z.; Jin, J. Thin-Film Nanocomposite Nanofiltration Membrane with an Ultrathin Polyamide/UIO-66-NH₂ Active Layer for High-Performance Desalination. *J. Memb. Sci.* **2020**. <https://doi.org/10.1016/j.memsci.2020.117874>.
- (29) Zhang, H.; Hou, J.; Hu, Y.; Wang, P.; Ou, R.; Jiang, L.; Zhe Liu, J.; Freeman, B. D.; Hill, A. J.; Wang, H. Ultrafast Selective Transport of Alkali Metal Ions in Metal Organic Frameworks with Subnanometer Pores. *Sci. Adv.* **2018**, *4* (2). <https://doi.org/10.1126/sciadv.aag0066>.
- (30) Fang, S. Y.; Zhang, P.; Gong, J. L.; Tang, L.; Zeng, G. M.; Song, B.; Cao, W. C.; Li, J.; Ye, J. Construction of Highly Water-Stable Metal-Organic Framework UiO-66 Thin-Film Composite Membrane for Dyes and Antibiotics Separation. *Chem. Eng. J.* **2020**, *385*, 123400. <https://doi.org/10.1016/j.cej.2019.123400>.
- (31) Zhao, D. L.; Yeung, W. S.; Zhao, Q.; Chung, T. S. Thin-Film Nanocomposite Membranes

- Incorporated with UiO-66-NH₂ Nanoparticles for Brackish Water and Seawater Desalination. *J. Memb. Sci.* **2020**. <https://doi.org/10.1016/j.memsci.2020.118039>.
- (32) Huelsenbeck, L.; Luo, H.; Verma, P.; Dane, J.; Ho, R.; Beyer, E.; Hall, H.; Geise, G. M.; Giri, G. Generalized Approach for Rapid Aqueous MOF Synthesis by Controlling Solution PH. *Cryst. Growth Des.* **2020**, *20* (10), 6787–6795. <https://doi.org/10.1021/acs.cgd.0c00895>.
- (33) Luo, H.; Cheng, F.; Huelsenbeck, L.; Smith, N. Comparison between Conventional Solvothermal and Aqueous Solution-Based Production of UiO-66-NH₂: Life Cycle Assessment, Techno-Economic Assessment, and Implications for CO₂capture and Storage. *J. Environ. Chem. Eng.* **2021**, *9* (2), 105159. <https://doi.org/10.1016/j.jece.2021.105159>.
- (34) Xu, G. R.; Xu, J. M.; Feng, H. J.; Zhao, H. L.; Wu, S. B. Tailoring Structures and Performance of Polyamide Thin Film Composite (PA-TFC) Desalination Membranes via Sublayers Adjustment-a Review. *Desalination*. 2017. <https://doi.org/10.1016/j.desal.2017.05.011>.
- (35) Alihemati, Z.; Hashemifard, S. A.; Matsuura, T.; Ismail, A. F.; Hilal, N. Current Status and Challenges of Fabricating Thin Film Composite Forward Osmosis Membrane: A Comprehensive Roadmap. *Desalination*. 2020. <https://doi.org/10.1016/j.desal.2020.114557>.

Chapter 3: Theoretical Models

3.1. Solution-Diffusion Resistance-in-Series Model

Layer-by-layer deposition allows for controlled growth of both our polymer primer and the PA layer. Since the thickness of both the PVA and PA layer is directly correlated with the number of cycles of LbL performed, a modified solution-diffusion model, considering the resistance of each layer, can be applied to understand the water and salt transport through the composite membrane. The following two sections will outline the solution-diffusion resistance-in-series model for water and salt transport through the generalized class of LbL-synthesized PA layers on PVA-primed polyethersulfone (PES) microporous supports discussed in this dissertation.

3.1.1. Water Transport

Water transport through the composite membranes prepared using the poly(vinyl alcohol) (PVA) primer and the LbL process can be analyzed using a series resistance model. As it is reasonable to assume that the microporous PES support does not contribute considerably to the overall resistance to water transport, two resistances can be considered for this system: the resistance to water transport through the PVA primed support and that of the polyamide (PA) layer.^{1,2} The water flux through the PVA primed support, $J_{w,0}$, is related to the water permeance through the PVA primed support, A_0 , as:

$$J_{w,0} = \frac{\Delta p - \Delta \pi}{A_0^{-1}} \quad (1)$$

where A_0^{-1} is the resistance to water transport through the PVA primed support. Accordingly, the water flux through the PA layer, $J_{w,x}$, is related to the water permeance through the PA layer, A_x , as:

$$J_{w,x} = \frac{\Delta p - \Delta \pi}{A_x^{-1}} \quad (2)$$

where A_x^{-1} is the resistance to water transport through the PA layer.^{1,2} Using the definitions in Equations 1 and 2 and the series resistance model, the water flux, J_w , and overall resistance to water transport, $A_{overall}^{-1}$, of the entire composite structure are:

$$J_w = \frac{\Delta p - \Delta \pi}{A_{overall}^{-1}} \quad (3)$$

$$A_{overall}^{-1} = A_0^{-1} + A_x^{-1} \quad (4)$$

If each layer has a uniform thickness, each resistance to water transport can be expressed in terms of an effective water permeability and layer thickness:

$$A_0 = \frac{\bar{V}_w P_{w,0}}{R_g T h_0} \quad (5)$$

$$A_x = \frac{\bar{V}_w P_{w,x}}{R_g T h_x} \quad (6)$$

where \bar{V}_w is the partial molar volume of water, R_g is the ideal gas constant, T is the absolute temperature, h_i is the layer thickness and $P_{w,i}$ is the effective water permeability of the layer. Here $i = 0$ for the PVA primed support, and $i = x$ for the PA layer.^{1,2} Equations 3-6 can be combined to relate the overall water flux to the water flux through the PVA primed support, the effective permeability values of the PVA primed support and the PA layer, the PVA primed support thickness, the PA layer thickness per LbL cycle, r , and the number of LbL cycles, x , as:

$$J_w = \frac{J_{w,0}}{1 + \frac{P_{w,0} r}{P_{w,x} h_0} x} = \frac{J_{w,0}}{1 + m_1 x} \quad (7)$$

The effective permeability values, growth rate, and PVA primed support thickness terms can be combined into m_1 .²

3.1.2. Salt Transport

Similarly, the series resistance model can be applied to analyze salt transport. The overall resistance to salt transport, $(B_{overall})^{-1}$, is:

$$(B_{overall})^{-1} = B_0^{-1} + B_x^{-1} \quad (8)$$

where $i = 0$ represents the contribution by the PVA layer and $i = x$ represents the contribution by the PA layer.^{1,2} Since the salt permeance, B , is typically calculated from the experimentally obtained salt rejection, R , and water permeance, A , data, the salt rejection can be analyzed for each layer of the composite membrane (i.e. PVA and PA layer) as the salt rejection of each layer depends on the resistances to water and salt transport (A and B respectively) of each layer.

First, the salt rejection that corresponds to the PVA primed support, R_0 , is related to the water and salt permeances of the PVA primed layer as:

$$R_0 = \frac{100\%}{1 + B_0 A_0^{-1} (\Delta p - \Delta \pi)^{-1}} \quad (9)$$

where B_0 is the salt permeance of the PVA primed support.² Likewise, the salt rejection that corresponds to the PA layer, $R_{s,x}$, is related to the water and salt permeances of the PA layer as:

$$R_{s,x} = \frac{100\%}{1 + B_x A_x^{-1} (\Delta p - \Delta \pi)^{-1}} \quad (10)$$

where B_x is the salt permeance of the PA layer.² Finally, the salt rejection, R_s , dependent on the overall resistances to both salt and water transport of the entire composite membrane, can be written as:

$$R_s = \frac{100\%}{1 + B_{overall} A_{overall}^{-1} (\Delta p - \Delta \pi)^{-1}} \quad (11)$$

For PA-TFC membranes, the salt permeance is typically calculated using Equation 11 and water permeance and salt rejection data measured using a pressurized filtration experiment.

The salt permeance is equivalent to the salt permeability divided by the layer thickness. As such, the relationships between the salt permeance and salt permeability for the two-layer system considered here are:

$$B_0 = \frac{P_{s,0}}{h_0} \quad (12)$$

$$B_x = \frac{P_{s,x}}{h_x} = \frac{P_{s,x}}{r x} \quad (13)$$

where $P_{s,i}$ is the salt permeability of the layer and h_i is the layer thickness. Here $i = 0$ for the PVA primed support, and $i = x$ for the PA layer. The PA layer thickness, h_x , is the product of the growth rate, r , and number of cycles, x .

3.2. References

- (1) Gu, J. E.; Lee, S.; Stafford, C. M.; Lee, J. S.; Choi, W.; Kim, B. Y.; Baek, K. Y.; Chan, E. P.; Chung, J. Y.; Bang, J.; Lee, J. H. Molecular Layer-by-Layer Assembled Thin-Film Composite Membranes for Water Desalination. *Adv. Mater.* **2013**, *25* (34), 4778–4782. <https://doi.org/10.1002/adma.201302030>.
- (2) Choi, W.; Gu, J. E.; Park, S. H.; Kim, S.; Bang, J.; Baek, K. Y.; Park, B.; Lee, J. S.; Chan, E. P.; Lee, J. H. Tailor-Made Polyamide Membranes for Water Desalination. *ACS Nano* **2015**, *9* (1), 345–355. <https://doi.org/10.1021/nn505318v>.

Chapter 4: Materials and Methods

4.1. Materials

4.1.1. Composite Membranes

Monomers and solvents were used as received from Sigma Aldrich. Trimesoyl chloride [98%] (TMC) and *m*-phenylenediamine [99%] (MPD) and were both dissolved in dry toluene [$\geq 99.5\%$] and used in Steps 1 and 5 (Figure 1), respectively, of the LbL PA preparation process. Methanol [$\geq 98\%$] was purchased from Sigma Aldrich and was used as the final rinse solvent in Step 7 of Figure 1. All solvents were dried with 3 Å molecular sieves prior to use.

Polyethersulfone (PES) support membranes, with a nominal 0.03 μm pore size, were purchased from Sterlitech Corporation and were cut to pressurized cell specifications prior to use.

Poly(vinyl alcohol) (PVA, molecular weight of 146,000 to 186,000 g/mol) polymer beads were purchased from Sigma Aldrich [catalog number: 363065].

4.1.2. UiO66-NH₂

All reagents were used as received with no further purification. Zirconyl chloride octahydrate ($\text{ZrOCl}_2 \cdot 8 \text{H}_2\text{O}$, 98% Alfa Aesar), acetic acid (Glacial Sigma Aldrich), sodium hydroxide pellets (NaOH, 98% Sigma Aldrich), 2-aminoterephthalic acid (H_2ATA , 99% Sigma Aldrich), and deionized water were used for the rapid synthesis of UiO-66-NH₂. Hydrochloric acid (37 wt%, Alfa Aesar) was used to prepare an aqueous solution of 0.01 M HCl. Dimethyl sulfoxide (DMSO, 99% Sigma Aldrich), ethanol (EtOH, 95% Koptec), and methanol (MeOH, 99.8% Sigma Aldrich) were used for washing and activating MOFs.¹

4.2. UiO66-NH₂ Synthesis

A metal solution was prepared following synthesis outlined by Szilagy *et al.*² Briefly, 1.2880 g $\text{ZrOCl}_2 \cdot 8\text{H}_2\text{O}$ was dissolved in 5 mL Acetic acid and 12 mL of DI water, placed in a Teflon

lined 20 mL scintillation vial, heated at 70 °C for two hours and allowed to cool to room temperature. The linker solution was prepared by mixing 0.7240 g of H₂ATA in a solution of 0.32 g NaOH in 20 mL DI water until dissolved. After centrifugation and drying, the solution was washed with a 0.01 M HCl solution, 0.001 M NaOH solution, DMSO and methanol to remove unreacted and soluble components of the precipitate. A solvent exchange with methanol was performed overnight before additional centrifugation and drying at 70 °C overnight.¹ UiO66-NH₂ solutions of varying concentration (0.2 mg/mL, 0.5 mg/mL, 1 mg/mL, and 1 mg/mL) were made in dry toluene and sonicated for 25 minutes prior to PA-TFN synthesis.

4.3. Layer-by-Layer Polymer Membranes

4.3.1. PVA-Primed Substrate Preparation

A layer of PVA was deposited onto either glass slide, microporous PES support, or silicon (Si) wafer substrates. A 2 wt% solution of PVA in water was prepared by mixing PVA with de-ionized (DI) water at 90°C until the PVA dissolved completely. For the glass slide substrate, a 500 µL aliquot of 2 wt% PVA in water was spin coated onto the substrate, using a spin rate of 3000 rpm for 30 sec. For PES support and Si wafer substrates, a 1.5 mL aliquot of 2 wt% PVA in water was spin coated at 3000 rpm for 30 sec, and this process was performed three times to form a thicker PVA layer. The area of the PES support and Si wafer substrates was the same, so the same deposition procedure was used for those two substrates. After deposition, all PVA-primed substrates were dried under vacuum at 70°C for at least 12 hours to dry the PVA layer.³

4.3.2. PA Selective Layer

4.3.2.1. MPD/TMC-based PA Synthesis

A layer-by-layer (LbL) sequential deposition method, similar to that of Johnson et al., was used with the exception that dry methanol, not dry acetone, was used as the rinse solvent that followed MPD deposition.⁴ Starting with either the bare (un-primed) or PVA-primed PES support, 900 μL of 1 wt% TMC in dry toluene was deposited on the substrate and left to rest for 10 sec (Figure 1, Step 1). The TMC monomer was used first so that reaction between the TMC acyl chloride groups and the PVA hydroxyl groups (Figure 1) could enhance attachment of the PA layer to the substrate when the PVA-primed microporous support was used. Then, the surface was spun at 3000 rpm for 20 sec (Figure 1, Step 2) to remove excess TMC solution. Next, 900 μL of dry toluene was deposited on the surface (Figure 1, Step 3) and immediately spun at 3000 rpm for 20 sec to further remove excess un-reacted TMC (Figure 1, Step 4). Subsequently, 900 μL of 1 wt% MPD in dry toluene was deposited onto the surface and allowed to react with the surface-bound TMC for 10 sec (Figure 1, Step 5). The substrate was then spun for 20 sec at 3000 rpm to remove excess solution (Figure 1, Step 6). The final rinse solvent, 900 μL of dry methanol, was deposited onto the surface (Figure 1, Step 7) and immediately spun at 3000 rpm

for 20 sec to remove excess un-reacted MPD (Figure 1, Step 8). Steps 1-8 symbolize one full cycle of LbL deposition.³

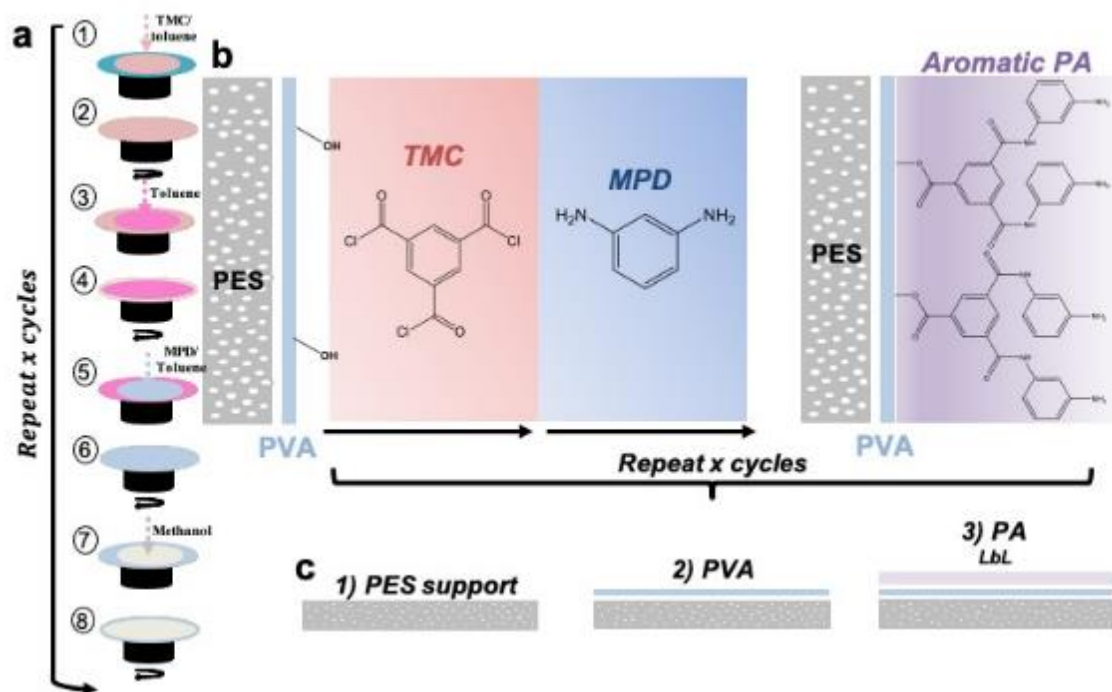


Figure 1. a) The LbL process proceeds in steps where solution deposition (odd steps) alternates with a spin-drying step at 3000 rpm (even steps). b) Schematic of LbL PA formation where TMC is deposited first followed by MPD. c) Schematic of the composite membrane formation process; PVA priming of the polyethersulfone, PES, support is followed by LbL to form the PA layer. Adapted from Ref. 11, with the permission of AIP Publishing.

The growth rate was defined as the PA layer thickness deposited per cycle. This growth rate was determined by characterizing PA layers deposited onto PVA-primed glass slide substrates, which were prepared as described in Chapter 5. The solution volumes used to deposit the PA layer onto the PVA-primed glass slide substrates were reduced from 900 μL to 500 μL to account for the smaller area of the glass slide substrate compared to the PES support and Si wafer substrates.³

4.3.2.2. Sulfonated PA Synthesis

A 0.4 wt/v% solution of 2,4-diaminobenzenesulfonic acid (MPDSA) in deionized water was made. An aliquot of 5 M potassium hydroxide was added to the MPDSA solution and mixed for 1 hour to neutralize the sulfonic acid groups on MPDSA resulting in potassium 2,4-diaminobenzenesulfonate (MPDSK). The volume of the aliquot was chosen to ensure complete neutralization of the sulfonic acid groups. The potassium salt form of this sulfonated diamine was used to increase the reactivity of the amine groups on the monomer. The resulting MPDSK solution was dried overnight at 110°C to recover the solid MPDSK product. A 0.07 wt/v% solution of MPDSK in dry tetrahydrofuran (THF) was mixed at 55°C until MPDSK completely dissolved (~2 hours). Finally, the MPDSK in THF solution was diluted with dry toluene to make the final 0.04 wt/v% MPDSK solution in 50:50 THF:toluene (by volume) used for sulfonated PA layer deposition.

Deposition of the sulfonated PA layer was done according to the LbL PA formation protocol described above with the following differences. The solution of MPDSK in THF:toluene was applied to the surface between steps 4 and 5 in Figure 1a. The MPDSK solution was allowed to contact the surface for 30 s before spinning off the excess solution. Then, the MPD solution was allowed to contact the surface for 5 s before proceeding with step 6 in Figure 1a.

4.3.2.3. UiO66-NH₂ Incorporated PA Synthesis

Deposition of the UiO66-NH₂-incorporated PA layer was done according to the LbL PA formation protocol described above with the following differences. After 15 cycles of LbL to form a PA layer of ~48 nm thick, a solution of 1 wt% TMC in dry toluene was deposited onto the surface and allowed to rest for 10 sec (Figure 2b, Step M1). Then, the surface was spun at 3000 rpm for 20 sec (Figure 2b, Step M2) to remove excess TMC solution. Next, UiO66-NH₂ in dry toluene of varied solution concentrations was deposited to the surface and allowed to react

with the surface-bound acyl chloride groups in TMC for 90 sec (Figure 2b, Step M3). The substrate was then spun for 20 sec at 3000 rpm to remove excess solution (Figure 2b, Step M4). Subsequently, 900 μL of 1 wt% MPD in dry toluene was deposited onto the surface and allowed to react with the surface-bound TMC for 10 sec (Figure 1, Step 5). The substrate was then spun for 20 sec at 3000 rpm to remove excess solution (Figure 1, Step 6). The LbL PA formation protocol was then continued as described in Section 4.2.1.2 for 15 cycles to cap off the composite membrane with ~ 48 nm of PA.³

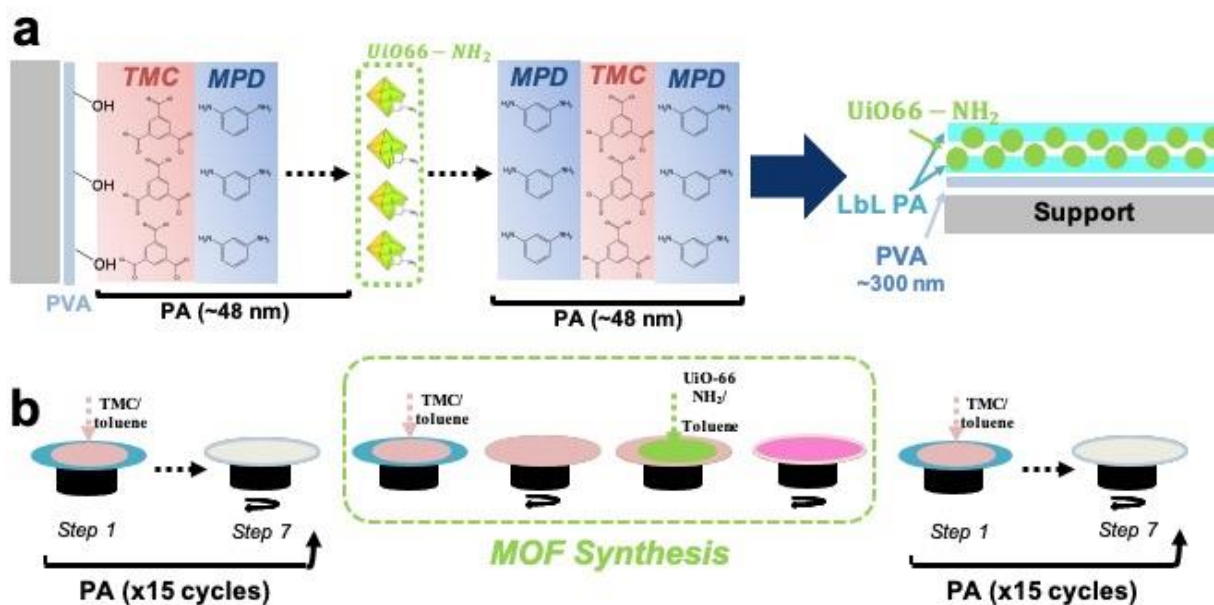


Figure 2. a) Schematic of LbL PA formation where TMC is deposited first followed by MPD repeatedly to form ~ 48 nm thick PA layers that “sandwich” UiO66-NH₂ for full incorporation. b) Schematic of LbL PA formation amended for MOF incorporation where the LbL MPD/TMC-based PA formation process is performed for 15 cycles to “sandwich” the deposition of MOF via a UiO66-NH₂ solution in dry toluene. Adapted from Ref. 11, with the permission of AIP Publishing.

4.4. Electrolytes and Dyes

Divalent electrolytes commonly used in RO and NF applications were used in this study. Sodium chloride (NaCl) was used as the salt of interest for membranes geared towards RO whereas magnesium sulfonate (MgSO₄) was used for membranes geared towards NF. Dyes of

different sizes were used as a metric for large impurity performance for membranes geared towards NF applications. In order of increasing atomic size, the following dyes were used in this study: methyl orange (MO), methylene blue (MB), and congo red (CR) . The molecular weight and atomic size of all dyes will be presented and discussed in the subsequent chapters.

4.5. Experimental Methods

4.5.1. Membrane and UiO66-NH₂ Characterization

4.5.1.1. Profilometry

The PVA and PA layer thicknesses were characterized using tapping profilometry. This method was chosen because it has been shown to be an accurate indicator of polyamide layer thickness.⁵ Tapping profilometry (Brüel DeltaXT Stylus Profiler) was performed using a 12.5 μm tip and a 2 mg stylus force. When measuring PVA layer thickness on PVA-primed glass slide and Si wafer substrates, a 60 μm/sec scan speed was used. When measuring the thickness of PA layers deposited on PVA-primed glass slide substrates, a 15-20 μm/s scan rate was used.

4.5.1.2. Atomic Force Microscopy (AFM)

Atomic Force Microscopy (AFM) was used to characterize the root mean square (RMS) roughness of the PVA and PA surfaces. Three samples were characterized using AFM: a PVA-primed glass slide, a PVA-primed glass slide with a PA layer deposited via LbL using acetone as the final rinse solvent, and a PVA-primed glass slide with a PA layer deposited via LbL using methanol as the final rinse solvent. The samples were prepared as described previously, and they were equilibrated at atmospheric conditions prior to characterization.

AFM micrographs were obtained using a Solver Nano Scanning Probe Microscope [Molecular Devices and Tools for NanoTechnology (MDT-NT)] placed on an isolation table (TS-150, Herzan) to damp vibrations in the environment.⁶ Measurements were performed using a

silicon-based cantilever and ultra-fine mechanical tip in tapping “SemiContact” mode through Nova software (ver. 1.0.26.1443). After the resonant frequency of the cantilever was found using the auto-tune function, the drive amplitude was adjusted until an oscillation amplitude of 24 nA was reached. The setpoint which dictates the average force between the probe tip and the sample, was then set at 12 nA to maintain low force on the soft polymer surface during measurements. Finally, 10 μm x 10 μm (1024 pixels x 1024 pixels) scans were made using a 1 Hz scan rate on atmospherically-equilibrated samples at room temperature. The uncertainty in the RMS roughness was taken to be one standard deviation of the RMS roughness values obtained from six scans of each sample.

4.5.1.3. Scanning Electron Microscopy (SEM)

Scanning Electron Microscopy (SEM) was used to cross-sectionally image the composite membranes. Five samples were imaged using SEM: PA-TFN made with 0.2 mg/mL UiO66-NH₂ solution, PA-TFN made with 0.5 mg/mL UiO66-NH₂ solution, PA-TFN made with 1 mg/mL UiO66-NH₂ solution, PA-TFN made with 2 mg/mL UiO66-NH₂ solution, and our baseline MPD/TMC-based PA-TFC membrane. These samples were imaged using field emission SEM after they were exposed to liquid nitrogen and cracked to form a clean cross-section for imaging. Cross-sectional SEM images were obtained using a Quanta 650 Schottky Field Emission SEM with a Secondary Electron (SE) backscattering detector. All images were taken with either 2.5 or 3.0 spot size resulting in similar resolution of images.

4.5.1.4. BET Analysis – N₂ Adsorption & Specific Surface Area

Nitrogen uptake isotherms were measured at 77 K with a Micromeritics ASAP 2020 Surface Area and Porosimetry analyzer. Data was analyzed using the ASAP 2020 V4.04 software. All gases used were high purity. Typically, 50-100 mg of MOF sample were dried

under vacuum at 80°C overnight before initiating previously reported degassing procedures for each MOF.¹

4.5.1.5. X-Ray Diffraction (XRD)

Powder x-ray diffraction (PXRD) patterns were collected using a PANalytical Empyrean X-ray Diffractometer (Malvern Panalytical, Egham, UK) with Cu K- α radiation. Scans were taken from $2\theta = 5^\circ$ - 20° for UiO-66-NH₂ and $2\theta = 5^\circ$ - 30° for UiO-66, HKUST-1, and ZIF-L. Diffraction patterns were analyzed using HighScore Plus X-ray Diffraction analysis software.¹

4.5.1.6. Thermogravimetric Analysis (TGA)

MOF loading of the membranes were determined using thermogravimetric analysis (TGA) [TA Instruments, Q50].⁷ Samples of PA layer coated PVA substrates synthesized with varying UiO66-NH₂ solution concentrations (0.2 mg/mL, 0.5 mg/mL, 1 mg/mL, and 2 mg/mL) were tested and compared a baseline membrane without UiO66-NH₂ as well as UiO66-NH₂ alone. Samples of membrane, sized 2.5 – 9 mg, were heated from room temperature to 1000C at a rate of 10C/min in a nitrogen atmosphere. As all organic components were expected to burn off prior to 1000C, the remaining mass fraction of material was assumed to be only UiO66-NH₂ providing the intrinsic MOF loading of the membrane in wt%.

4.5.1.7. Fourier Transform Infrared Spectroscopy (FTIR)

To confirm the polyamide structure of our membranes, PA layers of varying MOF loading deposited on PVA substrates were tested using Fourier Transform Infrared Spectroscopy (FTIR) [Perkin Elmer Frontier MIR/NIR].⁸ Samples were scanned with a total reflectance mode on a diamond/ZnSe crystal. After software normalization, a scan range of 4000 cm⁻¹ – 650 cm⁻¹ was applied to determine the transmittance of the PVA substrate baseline and PA-coated PVA

substrates made with varying MOF solution concentration (0 mg/mL, 0.2 mg/mL, 0.5 mg/mL, 1 mg/mL, 2 mg/mL).

4.5.2. Performance Tests

4.5.2.1. Water and Salt Transport

Water and salt transport properties were determined using a pressurized dead-end stainless-steel permeation cell (HP4750 stirred cell, Sterlitech Corp., Kent, WA).⁹⁻¹² The LbL PA-TFCs were soaked in DI water for at least 24 hr before testing. Each sample was placed onto a porous stainless-steel support and secured within the permeation cell. For both water and salt transport tests, approximately 250 mL of solution (DI water or 2000 mg/L NaCl solution, respectively) was used to fill the cell. The cell subsequently was sealed and pressurized with nitrogen gas at either 350 psi (24.1 bar) for PA-TFC tests or 50 psi (3.4 bar) for PVA-primed support tests.

To measure water permeance, A , the permeate flow rate was measured after stabilization (roughly an hour after the start of the measurement) using a 25 mL graduated cylinder to track the collected volume as a function of time. This flow rate information was normalized by the membrane area available for transport ($S_A = 0.00146 \text{ m}^2$) to obtain the water flux, J_w . This flux was normalized further by the applied pressure difference, Δp , minus the osmotic pressure difference, $\Delta\pi$, which was taken to be zero for pure water permeance measurements, to determine the water permeance as:¹³

$$A = \frac{J_w}{(\Delta p - \Delta\pi)} \quad (1)$$

Salt permeance was determined from measured water permeance and salt rejection data. A feed solution of 2000 mg/L salt solution was used in place of DI water to measure the permeance of the membrane exposed to salt solution. The osmotic pressure for each binary salt solution was calculated using the van't Hoff equation ($i = 2$; $T = 298 \text{ K}$; $R = 0.0821 \text{ L}\cdot\text{atm}/\text{mol}\cdot\text{K}$; $i = 2$; $T = 298 \text{ K}$; $R =$

0.0821 $\frac{L-atm}{K-mol}$) and scaled by the respective salt molecular weight (NaCl = 58.44 g/mol; MgSO₄ = 120.37 g/mol).¹⁴ Salt rejection, R , was determined, using measured feed, C_f , and permeate, C_p , concentrations as:¹⁵

$$\Pi = iMRT \quad (2)$$

$$R = \frac{C_f - C_p}{C_f} \times 100\% \quad (3)$$

Salt concentrations were measured, using a Mettler Toledo S470-Basic SevenExcellence conductivity meter, after 2 hr of stabilized permeation. Salt permeance, B , was calculated from water permeance and salt rejection data as:¹⁶

$$R = \frac{\frac{A}{B}(\Delta p - \Delta \pi)}{1 + \frac{A}{B}(\Delta p - \Delta \pi)} \times 100\% \quad (4)$$

4.5.2.2. Ionic Conductivity

Four probe in-plane conductivity measurements¹⁷ were made using a membrane conductivity clamp (Scribner Associates Inc., North Carolina). The bottom plate of this clamp contains 4 platinum electrodes and a platinum gauze that contact the membrane in a manner that facilitates the in-plane conductivity measurement when the membrane is secured by the top clamp. Direct current (DC) chronopotentiometry measurements were performed using a potentiostat and the associated automation and analysis software (SP-150 Potentiostat and EC-Lab Software, Biologic, France). The range of current used in the experiment was fixed at either 0.1 – 1.1 nA (for the PVA and MPD-based PA layers) or 0.1 mA – 1.1 mA (for the MPDSK-MPD-based PA layer). The potentiostat was used to set four different currents (within the ranges described above) between the outermost platinum electrodes. Each current was maintained for 120 s to ensure a pseudo steady state measurement. The corresponding voltage was measured, at each current, across the innermost platinum electrodes.

The data were analyzed using an IV curve, and the Ohmic resistance, was determined, in units of Ohms, as the slope of the voltage versus current data, and the conductivity was taken as the inverse of the resistance (in units of siemens). Samples were tested three times, and the cell was disassembled and reassembled between each measurement. The uncertainty in the measurement was taken as one standard deviation from the mean of these three conductivity measurements.

4.5.2.3. Dye Rejection

Dye permeance was determined from measured water permeance and dye rejection data. A feed solution of 10 mg/L dye solutions (Methyl Orange, Methylene Blue, and Congo Red) was used in place of DI water to measure the permeance of the membrane exposed to dye solution.¹⁸ The osmotic pressure for each dye solution was calculated using the van't Hoff equation (Eq 2) [$i = 1$; $T = 298 \text{ K}$; $R = 0.0821 \frac{\text{L-atm}}{\text{K-mol}}$] and scaled by the respective dye molecular weight (Methyl Orange = 327.33 g/mol; Methylene Blue = 319.85 g/mol; Congo Red = 696.67 g/mol).^{14,18} Dye rejection, R_{dye} , was determined, using measured feed, $C_{f,dye}$, and permeate, $C_{p,dye}$, concentrations as:¹⁵

$$R_{dye} = \frac{C_{f,dye} - C_{p,dye}}{C_{f,dye}} \times 100\% \quad (5)$$

Dye absorbances were measured, using a BioMate3S UV-Vis Spectrometer [ThermoFisher], after 2 hr of stabilized permeation. Concentration was calculated from the absorbance based on the Beer-Lambert law direct correlation. Dye permeance, B_{dye} , was calculated from water permeance and dye rejection data as:^{16,18}

$$R_{dye} = \frac{\frac{A}{B_{dye}}(\Delta p - \Delta \pi)}{1 + \frac{A}{B_{dye}}(\Delta p - \Delta \pi)} \times 100\% \quad (6)$$

4.6. References

1. Huelsenbeck L, Luo H, Verma P, et al. Generalized Approach for Rapid Aqueous MOF Synthesis by Controlling Solution pH. *Cryst Growth Des.* 2020;20(10):6787-6795. doi:10.1021/acs.cgd.0c00895
2. Pakamoré I, Rousseau J, Rousseau C, Monflier E, Szilágyi PÁ. An ambient-temperature aqueous synthesis of zirconium-based metal–organic frameworks. *Green Chem.* 2018;20(23):5292-5298. doi:10.1039/C8GC02312C
3. Agata W-AS, Thompson J, Geise GM. Layer-by-layer approach to enable polyamide formation on microporous supports for thin-film composite membranes. *J Appl Polym Sci.* n/a(n/a):51201. doi:https://doi.org/10.1002/app.51201
4. Johnson PM, Yoon J, Kelly JY, Howarter JA, Stafford CM. Molecular layer-by-layer deposition of highly crosslinked polyamide films. *J Polym Sci Part B Polym Phys.* 2012;50(3):168-173. doi:10.1002/polb.23002
5. Lin L, Feng C, Lopez R, Coronell O. Identifying facile and accurate methods to measure the thickness of the active layers of thin-film composite membranes - A comparison of seven characterization techniques. *J Memb Sci.* Published online 2016. doi:10.1016/j.memsci.2015.09.059
6. Freger V. Swelling and morphology of the skin layer of polyamide composite membranes: An atomic force microscopy study. *Environ Sci Technol.* Published online 2004. doi:10.1021/es034815u
7. McCormack PM, Luo H, Geise GM, Koenig GM. Conductivity, permeability, and stability properties of chemically tailored poly(phenylene oxide) membranes for Li⁺ conductive non-aqueous redox flow battery separators. *J Power Sources.* 2020;460:228107. doi:https://doi.org/10.1016/j.jpowsour.2020.228107
8. Jung S, Huelsenbeck L, Hu Q, Robinson S, Giri G. Conductive, Large-Area, and Continuous 7,7,8,8-Tetracyanoquinodimethane@HKUST-1 Thin Films Fabricated Using Solution Shearing. *ACS Appl Mater Interfaces.* 2021;13(8):10202-10209. doi:10.1021/acsami.1c00640
9. Gu JE, Lee S, Stafford CM, et al. Molecular layer-by-layer assembled thin-film composite membranes for water desalination. *Adv Mater.* 2013;25(34):4778-4782. doi:10.1002/adma.201302030
10. Chowdhury MR, Steffes J, Huey BD, McCutcheon JR. 3D printed polyamide membranes

- for desalination. *Science* (80-). 2018;361(6403):682-686. doi:10.1126/science.aar2122
11. Baker RW. *Membrane Technology and Applications.*; 2004. doi:10.1016/S0376-7388(00)83139-7
 12. Cussler EL. *Diffusion: Mass Transfer in Fluid Systems.* Vol Second.; 2009. doi:10.1017/CBO9780511805134.010
 13. Zhang H, Geise GM. Modeling the water permeability and water/salt selectivity tradeoff in polymer membranes. *J Memb Sci.* 2016;520:790-800. doi:10.1016/j.memsci.2016.08.035
 14. *Electrochemistry:* by Carl H. Hamann, Andrew Hamnet, Wolf Vielstich, Wiley–VCH, Weinheim, 2nd completely revised and updated edn, 2007, pp 550, ISBN 978-3-527-31069-2. Price: EUR 65.00, USD 95.00. *Chromatographia.* Published online 2010. doi:10.1365/s10337-009-1435-y
 15. Geise GM, Park HB, Sagle AC, Freeman BD, McGrath JE. Water permeability and water/salt selectivity tradeoff in polymers for desalination. *J Memb Sci.* 2011;369(1-2):130-138. doi:10.1016/j.memsci.2010.11.054
 16. Geise GM, Paul DR, Freeman BD. Fundamental water and salt transport properties of polymeric materials. *Prog Polym Sci.* 2014;39(1):1-42. doi:10.1016/j.progpolymsci.2013.07.001
 17. Shi S, Weber AZ, Kusoglu A. Structure/property relationship of Nafion XL composite membranes. *J Memb Sci.* 2016;516:123-134. doi:10.1016/j.memsci.2016.06.004
 18. Fang SY, Zhang P, Gong JL, et al. Construction of highly water-stable metal-organic framework UiO-66 thin-film composite membrane for dyes and antibiotics separation. *Chem Eng J.* 2020;385:123400. doi:10.1016/j.cej.2019.123400

Chapter 5: Layer-by-Layer Approach to Enable Polyamide Formation on Microporous Supports for Thin-Film Composite Membranes

This study investigates the application of a spin-coater based layer-by-layer synthesis of a polyamide selective layer on microporous supports. The main objective of this study is to assess the shift of this polyamide deposition process to PA-TFC membrane formation through RO-based water and salt transport tests. In addition, we assess the expansion of this polyamide synthesis technique for the incorporation of fixed charge groups to the PA layer via a sulfonated co-monomer.

5.1. Introduction

Polymer membranes for water purification and energy applications must be both thin and selective to minimize mass transfer resistance and maximize separation efficiency. One of the most commercially successful examples is the polyamide thin-film composite (PA-TFC) reverse osmosis membrane.^{1,2,11,12,3-10} These membranes are manufactured to feature a thin (order 100 nm) dense cross-linked aromatic polyamide (PA) film that promotes water transport while minimizing salt transport.^{1,2,11,12,3-10} The PA layer typically is synthesized by interfacial polymerization (IP) of *m*-phenylenediamine (MPD) and a tri-functional acid chloride, trimesoyl chloride (TMC).¹³

The reaction is self-limiting, and the structure of the PA layer is primarily dictated by the reactivity, solubility, and diffusivity of the monomers.¹⁻⁹ This characteristic of the IP process, which is central to the commercial success of PA-TFC membranes, also limits the use of other co-monomers. The IP reaction is fast, so solubility and diffusivity factors often control diamine transport to the reaction zone.¹⁰⁻¹² As such, co-monomers with lower solubility and/or diffusivity compared to MPD may not incorporate in the PA layer prepared via IP.

This limitation could hinder the use of IP to access unique combinations of PA-TFC transport properties by controlling the chemical composition of the PA layer.¹⁰⁻¹² Polyamide formation via a sequential deposition (or layer-by-layer, LbL) technique could circumvent this limitation by reducing the significance of the thermodynamic and kinetic factors that control film formation in the IP process.^{9,11,12} Therefore, LbL could facilitate the incorporation of multiple co-monomers (of varying composition) into the PA layer. By doing so, LbL could enable access to unique PA-TFC membrane transport properties.

The LbL process was adopted for PA layer formation based on layer-by-layer assembly of polyelectrolytes.⁹ In the context of polyamide desalination membranes, LbL can be used to deposit monomers onto the surface where a polycondensation reaction occurs to form a cross-linked PA network (**Figure 1 in Chapter 4**).^{8,9,11,12} Since LbL PA layer formation does not require the liquid-liquid interface that occurs in conventional IP, smoother membranes can be made compared to those prepared via IP because the LbL process brings monomers to the surface in a controlled manner. Smoother membranes often have advantages in applications due to, for example, reduced fouling propensity.^{1,2,11,12,3-10}

Additionally, by removing the diamine diffusion limitation and controlling the placement of co-monomers on the surface, LbL enables control over the chemistry of the PA film at the monomer length scale. This level of molecular control generally is not accessible using the IP process.^{8,9} Control over the PA film chemistry is facilitated by the LbL deposition process because reactions are limited to surface bound reactive sites. Since films can be grown via sequential deposition, monomer concentration and reactivity limitations (inherent to IP) may be overcome. Thus, LbL could allow for nanometer control over film thickness and local chemical and polymer composition.^{8,9}

The LbL approach to making PA layers, within the context of desalination membranes, largely has been studied using silicon or glass substrates.^{8,9} To be viable for separations, the selective membrane must be formed upon a microporous support. Doing so can be challenging because LbL deposition onto a microporous support can lead to defects in the selective membrane that compromise performance properties.^{11,12}

Here, we report an approach for priming the microporous support using poly(vinyl alcohol) (PVA), similar in principle to approaches that use a polyelectrolyte primer,^{11,12} to mitigate defect formation in LbL PA layers. The PVA layer was chosen because PVA adheres well to the support membrane surface, protects the microporous support (by reducing exposure to organic solvents during the polyamide deposition process), and provides a reactive surface to facilitate PA layer formation (the hydroxyl groups on the PVA surface can react with acid chloride functionality of the monomer used to start the PA layer deposition process).⁸ Importantly, the PVA layer appears to contribute negligibly to the overall mass transfer resistance of the membrane. Additionally, a sulfonated diamine monomer was incorporated into the polyamide layer suggesting that the LbL process could provide a viable pathway for incorporating a range of functional monomers into thin, defect free PA layers. As such, the combination of a primed support and the LbL process may enable access to an array of functional thin polymer films with unique separation properties.

5.2. Results and Discussion

5.2.1. Growth Rate and Surface Roughness

The growth rate of the PA layer was determined for PA layers deposited on a ~40 nm thick PVA layer that had been deposited onto a glass slide. As the number of LbL cycles increased, the PA layer thickness grew at an approximate rate of 3.2 nm/cycle and became more

variable (**Figure 1**). To put the growth rate into context, a theoretical minimum thickness for a single cycle can be estimated by assuming each monomer stacks orthogonally to the substrate (as suggested in Figure 1b in Chapter 4). The van der Waals volumes of each monomer, calculated using a group contribution method, suggest that a single LbL cycle (Figure 1a in Chapter 4) could cause the membrane thickness to increase by approximately 1.4 nm if a monolayer of acid chloride were to react with a monolayer of diamine in a manner that caused the molecules to stack orthogonally to the substrate. This group contribution value closely agrees with a comparable estimate of approximately 1.5 nm obtained using molar volumes determined from monomer density properties.^{14,15} Johnson et al. reported a growth rate of approximately 1 nm/cycle,⁸ and this result suggests that, in their process, the PA layer may not grow strictly orthogonally to the substrate, which would lead to a smaller increase in thickness per cycle compared to the estimated theoretical minimum thickness values.

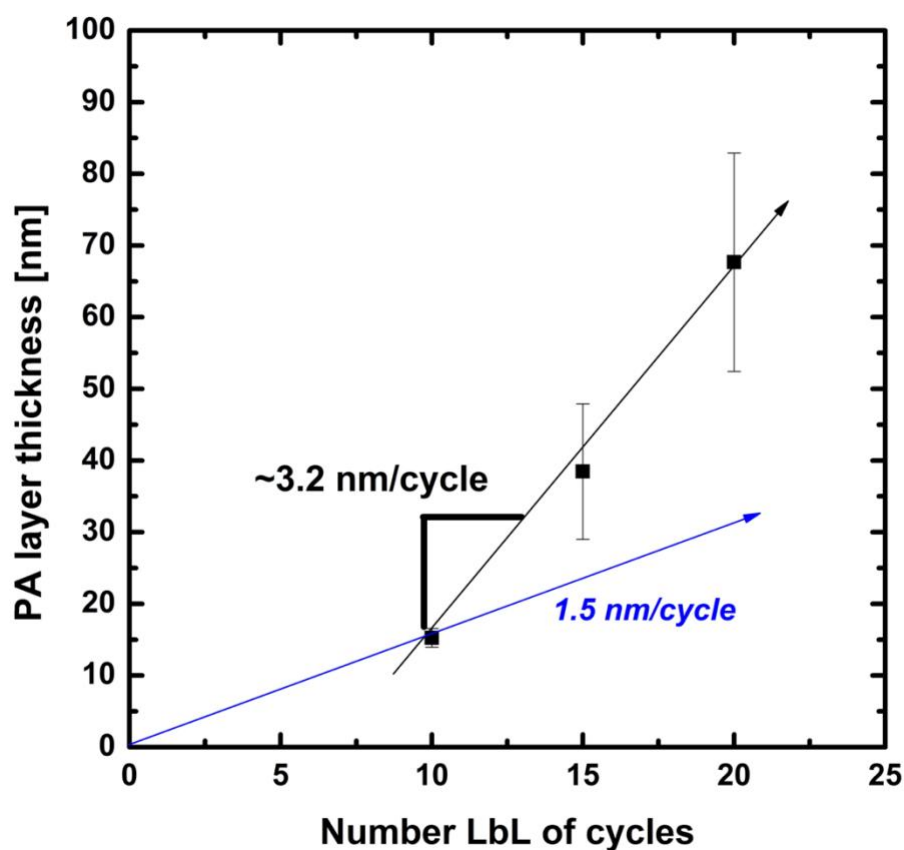


Figure 1. The PA layer thickness increased as the number of LbL cycles increased. All PA layers were deposited on PVA coated glass slides. The growth rate of approximately 3.2 nm/cycle was obtained via linear regression of the PA layer thickness data measured when 10, 15, or 20 LbL cycles were used. For comparison, a line is provided to illustrate a 1.5 nm/cycle growth rate starting from zero thickness in the absence of a PA layer (i.e., zero LbL cycles).

In this study, the observed growth rate of 3.2 nm/cycle, for PA layers prepared with 10, 15, or 20 LbL cycles (i.e., LbL₁₀, LbL₁₅, or LbL₂₀), was larger than the theoretical minimum and the work of Johnson et al.⁸ It was, however, comparable to the ~3 nm/pass growth rate reported for a monomer-by-monomer spray-coating PA layer formation technique.¹⁰ Interestingly, the thickness of the LbL₁₀ PA layer is consistent with a growth rate of 1.5 nm/cycle (Figure 1), which is the theoretical growth rate calculated using molar volume properties of the monomers (see discussion above).

Potential acceleration in the growth rate and increased variability as the number of LbL cycles increases (Figure 1) could stem from a number of factors. Film deposition processes are often highly sensitive to variability in processing parameters, so subtle changes in processing parameters can result in a wide range of coating thicknesses for a given material.¹⁶ Here we focus the discussion on the potential contributions from the rinse solvent. As discussed in Section 5.2.2, we used dry methanol as the final rinse solvent because acetone could dissolve the microporous PES support. As discussed in more detail in the Supporting Information, methanol and acetone appear to be comparable final rinse solvents from a miscibility and surface roughness perspective. Therefore, differences in the rinse solution volumes used and potential swelling of the polyamide may drive the increase in variability and growth rate acceleration observed as the number of LbL cycles increased from 10 to 20 cycles.

Sequential deposition techniques that do not depend on a spin coating or drying process, e.g., spray and dip coating, do not use a wash solvent between cycles.¹⁶ One such monomer by monomer spray-coating PA layer formation technique yielded a ~3 nm/pass growth rate.¹⁰ This reported growth rate is similar to the growth rate observed in this study between 10 and 20 LbL cycles. This similarity is reasonable given the relatively small volume of rinse solvent that was used in the deposition process in this study. In both this study and the spray coating report, residual monomer on the surface (due to the nature of the deposition process) could lead to a higher growth rate compared to the theoretical values based on monolayer monomer deposition.

Furthermore, continuous exposure to organic solvents can swell polymers, e.g., PA and PVA.^{17,18} Figure 1 shows the theoretically determined growth rate of 1.5 nm/cycle (blue line with the y-intercept set at the origin to indicate that at no growth had occurred at 0 cycles. Based on this trajectory, the growth of our PA layer via LbL with methanol as the final rinse solvent

produces the theoretically expected ~15 nm PA layer after 10 cycles. However, the growth rate accelerates as 10 to 20 LbL cycles are completed. Continued exposure to methanol, in addition to residual monomer on the surface (as discussed above) may contribute both to the accelerated growth rate and the additional variability in the thickness as the number of LbL cycles increases. PA layers are known to swell when exposed to methanol, and this process, known as “polyamide activation”, also affects the membrane’s water-salt permselectivity properties.¹⁷ Swelling of the PA layer, much like the PVA layer, is expected to occur predominantly in the direction perpendicular to the membrane surface due to the high surface area to volume ratio of the thin layers, and as such, lateral swelling is unlikely to be significant in these membranes.^{19,20}

The observation that PA layer thickness may follow the 1.5 nm/cycle theoretical prediction for 10 LbL cycles or less may be a result of the initial formation of the PA layer; the effects of swelling and residual monomer may become more pronounced as a more swollen PA layer forms on the surface. This can be understood in the context of Freger’s description of PA layer growth consisting of the initial rapid formation of a dense PA core layer surrounded by a looser polymer structure.² Though monomer diffusion factors should be minimized with LbL, the accelerated PA growth rate suggests that this swelling could lead to a similar slow-down of the initial reactivity profile and therefore a “fluffier” PA layer as the number of cycles increases.²

The methanol final rinse solvent is similarly capable of removing excess MPD compared to acetone. Therefore, acceleration of the PA layer growth rate, compared to the theoretical value (Figure 1), is most likely a result of the combined effects of PA layer swelling and residual monomer on the surface due to the rinse protocol used in this study.¹⁷ These factors appear to become more influential as the number of LbL cycles increases and greater exposure to methanol has occurred.^{8,17}

5.2.2. Water Transport

When the LbL approach is used to deposit a polyamide layer directly onto the microporous support, the water flux decreases as the number of LbL cycles increases (**Figure 2**), which is consistent with increased resistance to water transport as the PA layer thickness increases. Additionally, the water flux was approximately 1 to 2 orders of magnitude larger than that of a commercially available control membrane (DuPont FilmTec™ SW30XLE). Both the magnitude of the water flux and the functional relationship between water flux and the number of LbL cycles suggest that the PA layer, deposited on the bare (un-primed) support, is likely defective (i.e., the surface is not covered with a continuous layer of polyamide material). These results are discussed subsequently using a series resistance model.^{11,12}

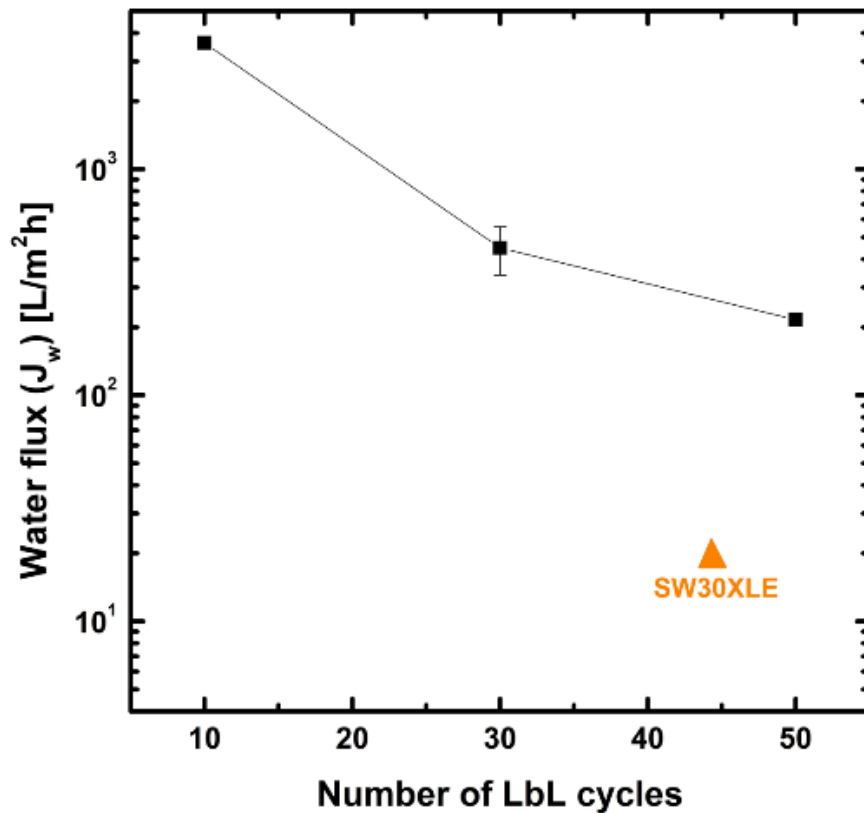


Figure 2. Water flux (J_w) as a function of the number of LbL cycles used to prepare the composite membranes (■). The LbL-prepared membranes are compared to water flux data for a commercially available membrane (DuPont FilmTec™ SW30XLE, ▲), which is positioned, on the horizontal axis, to reflect a typical ~150 nm thick PA layer and the reported LbL growth rate of 3.2 nm/cycle observed in this work. The water flux data were collected, at room temperature, using a pressurized dead-end cell method where the pressure applied to the DI water feed for all membranes was 24.1 bar (350 psi).

A series resistance model (described in more detail in Chapter 3 and Appendix B) suggests that, if the intrinsic water permeability of the polyamide is independent of thickness, the logarithm of the water permeance should decrease as the logarithm of the membrane thickness increases with a scaling relationship of -1 (Equation B2). This result is attributed simply to the fact that a thicker membrane provides higher resistance to mass transfer. Given the constant growth rate reported in Figure 1, water permeance data would be expected to exhibit this same scaling behavior with the number of LbL cycles.

The data, however, deviate from this scaling relationship (Figure B2). The interpretation shown in Figure B2 suggests that the membrane with the largest number of LbL cycles may be the most likely to be defect free. Then, as the number of LbL cycles is reduced, the water permeance increases to a greater extent than predicted by the series resistance model. This result suggests that membranes prepared using lower numbers of LbL cycles inherently may be more defective.^{8,10,12}

It is important to note that it is assumed (for the resistance in series model) that the PES microporous support does not contribute significantly to the overall resistance to transport (and thus is not included explicitly when considering the individual layers of the composite structure). This assumption is based on the PES support water permeance, which is two to four orders of magnitude greater ($\sim 10^3$ L/m²h – bar) than that of the PA-TFC membranes (10^{-1} to 10^1

L/m²h – bar, Table B2). Therefore, if the expression for the overall mass transfer resistance, $A_{overall}^{-1}$ (Equation 4 in Chapter 3), contained a contribution for the PES support, it would be small compared to that of the other layers.

Furthermore, the deviation from the –1 scaling relationship (Equation B2) suggests that, even with an increased growth rate, r , the water permeance and the estimated intrinsic water permeability of the LbL membranes would still be substantially greater than that of the control membrane. The deviation from the scaling relationship may also be a result of support membrane degradation due to the use of organic solvents during the LbL deposition process. Though PES is more chemically resistant to degradation by methanol as opposed to acetone (used in other LbL reports), increased exposure to toluene (the solvent for both monomers) as the number of LbL cycles increases, could contribute to degradation of the PES support membrane, which could lead to greater defect formation in the PA layer.^{8,9}

The discussion above points to a situation where the PA layer formed directly on a microporous support is likely defective and not suitable for use as a desalination membrane. Using a primer layer could help address these issues by providing a more uniform and chemically favorable surface at the beginning of the LbL process and/or by further protecting the PES support from potential degradation due to contact with organic solvents, as has been successfully demonstrated by the use of ceramic ultrafiltration supports for organic solvent nanofiltration applications.²¹ Next, we consider the use of a primer to facilitate LbL polyamide formation.

Using an approximately 288 nm layer of poly(vinyl alcohol) (PVA) to prime the support membrane before performing the LbL process causes an order of magnitude decrease in the water permeance relative to the membranes prepared on the bare (un-primed) support (**Figure 3**).

The water permeance, for example, of the LbL₃₀ membrane is reduced by approximately two orders of magnitude when the PVA primer layer is used, and the water permeance of this membrane is more consistent with that of the commercial SW30XLE membrane (Figure 3). These results are consistent with the idea that the PVA primer layer may address defect formation or other issues facing PA layer formation using LbL deposition on bare (un-primed) microporous supports.

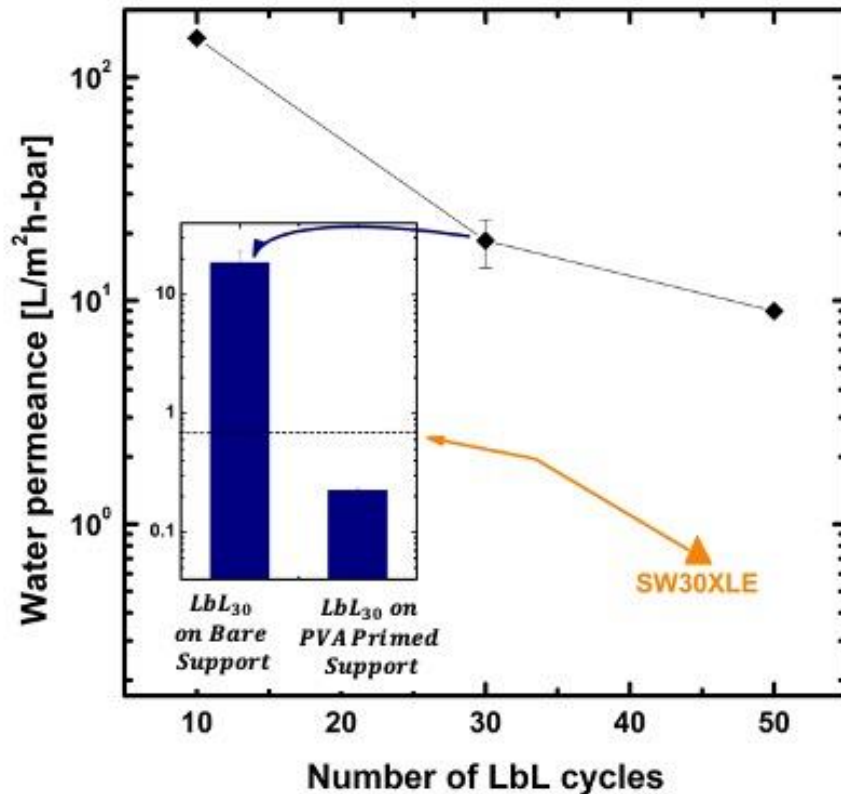


Figure 3. Water permeance data as a function of the number of LbL cycles used to prepare the membrane. Results are shown for PA-TFCs made on un-primed PES supports (◆), and the bar graph compares samples of similar thickness (30 LbL cycles = ~96 nm PA layer) formed on PVA-primed and bare (un-primed) PES supports. A measured water permeance of 0.7 L/m²h – bar for a commercially available membrane (DuPont FilmTec™ SW30XLE, ▲ and dotted line) is plotted for comparison.

Since an additional layer has been introduced to the typical two-layer PA-TFC structure, the series resistance model can be modified and used to deconvolute the contribution of each layer to the overall resistance to water transport, $A_{overall}^{-1}$ (Equation 4 in Chapter 3). By understanding the mass transfer contribution of each layer, we can determine whether the PVA primer facilitates defect-free PA formation without incurring a significant mass transfer penalty. Furthermore, the analysis could provide insight into how thick the PVA primer layer could be without introducing a significant mass transfer resistance. This insight would be particularly useful to efforts to extend this approach to different co-monomers.

The series resistance model (Chapter 3), applied to the PVA-primed PA-TFC system, can be used to isolate the contribution of each layer to the overall membrane water permeance, $A_{overall}$. The model accounts for mass transfer resistances due to the PVA-primed support, A_0 , and the PA layer, A_x .^{11,12} The explicit mass transfer resistance contribution of the PES support is neglected since, as discussed previously, the water permeance of the PES support membrane is at least an order of magnitude larger than that of the other membranes considered (Table B2) suggesting a negligible mass transfer resistance contribution in comparison to that of the membranes prepared with PVA and PA. Using expressions for water transport through the two-layered system of both the PVA-primed support and the PA layer (Equation 1, 2, 4-6 in Chapter 3), the contribution of the PVA-primed support was ascertained by determining the deviation of $A_x/A_{overall}$ (i.e., the fraction of the overall water permeance that results from the PA layer) from unity (Table B3). If reasonably close to unity, this ratio indicates that the majority of the resistance to water transport is provided by the PA layer, and this information can be used to determine how thick the PVA layer could be without significantly affecting mass transfer (e.g., a threshold of $\leq 5\%$ could be set to determine how thick the PVA layer could be before it

contributed more than 5% of the overall resistance to water transport). Context for calculations relating to the mass transfer contribution of the PVA layer can be found in Section B3 and B4.

The value of $A_s/A_{overall}$ for our LbL₃₀ PA layer on PVA-primed PES deviates from 1 by only 0.3% (Table B3). These results suggest that the ~288 nm thick PVA layer used to prime the microporous PES support does not contribute significantly to the overall resistance to water transport through the composite structure. Furthermore, this ratio indicates that a roughly 4 μm thick PVA layer may be able to be used without contributing more than a 5% loss in the overall resistance to water transport. With a PVA thickness of approximately 4 μm , a water permeance of 35 $\text{L}/\text{m}^2\text{h} - \text{bar}$ would be expected for the composite membrane. This value is an order of magnitude less than the experimentally determined PVA-primed support water permeance of 496 $\text{L}/\text{m}^2\text{h} - \text{bar}$. The wide range of thicknesses possible for the primer PVA layer allows for flexibility when considering membrane applications that require a thinner selective layer, where thicker PVA would prove useful for thinner defect free PA layers ($< 100 \text{ nm}$) and the expansion to unique ion transport pathways by incorporating charged monomers into the polyamide. It is important to note that though the overall water permeance of LbL₃₀ on a PVA-primed support is less than that of the commercial SW30XLE membrane, additives and further LbL process optimization may provide opportunities to access water permeance values of a similar order of magnitude.

From a water transport perspective, the PVA primer layer may address defects that form during LbL and/or other issues that result when LbL is performed on a bare (un-primed) microporous support. The significant observed decrease in $A_{overall}$ from 18 $\text{L}/\text{m}^2\text{h} - \text{bar}$ to 0.2 $\text{L}/\text{m}^2\text{h} - \text{bar}$ after the addition of the PVA primer layer, provides evidence to support this physical picture. By providing both a reactive surface to facilitate PA layer growth and

microporous support membrane protection from the organic solvents used in the LbL process, the PVA primer facilitated preparation of LbL composite membranes without introducing a significant additional mass transfer resistance. Furthermore, we did not see evidence of dimensional stability issues associated with excessive swelling of PVA (at the room temperature conditions of our experiments). If dimensional stability became a concern, the PVA primer layer could be crosslinked using glutaraldehyde or bicarboxylic acids.^{22,23} A series resistance model analysis suggested that PVA layers of up to 4 μm in thickness could be used without increasing the resistance to water transport by more than 5%. Ultimately, the addition of the PVA layer could provide insight into the relationship between water transport and the number of LbL cycles (Figure S3), insight into the intrinsic membrane water permeability, and a pathway for preparing polyamides containing different monomer building blocks.

5.2.3. Salt Transport and Water/Salt Selectivity

A similar approach can be used to analyze salt transport properties (Chapter 3 and Section B6). The series resistance model can be applied to salt transport and salt rejection (Equation 8-13 in Chapter 3). As salt rejection depends on the relative rates of water and salt transport, salt rejection trends can be related to both water (A) and salt (B) permeance parameters. In the absence of the PVA primer layer, the overall resistance to salt transport is solely due to the PA layer ($B_{\text{overall}} = B_x$).

Salt rejection values for bare (un-primed) support LbL PA-TFCs are well below half that of the commercial SW30XLE membrane (**Figure 4b**). This result is consistent with the water permeance results that, for the bare (un-primed) support membranes, were much greater than that of the commercial SW30XLE membrane and suggested the defect formation. Figure 4a shows an expected negative correlation between salt permeance, B , and number of LbL cycles, and these

values all are at least 3 orders of magnitude greater than that of the commercial SW30XLE membrane. As water and salt transport are linked, the combined effect of the increased water (*A*) and salt (*B*) permeance values of these bare (un-primed) support PA-TFCs translates into lower salt rejection values (Figure 4b). These low salt rejections are an indicator of defects in the PA layer due to poor membrane formation without the presence of a support primer.

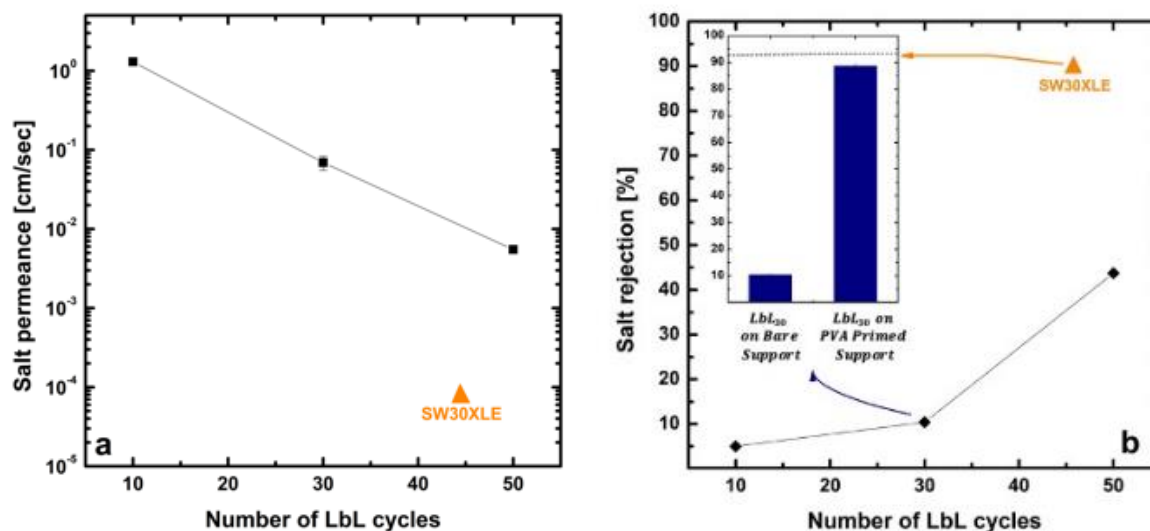


Figure 4. a) Salt permeance of un-primed support PA-TFCs a function of the number of LbL cycles calculated based on salt rejection experiments using a 2000 ppm NaCl feed solution at 24.1 bar (350 psi) (■). b) Salt rejection as a function of the number of LbL cycles performed using a 2000 ppm NaCl feed solution at 24.1 bar (350 psi) (◆). The diamond markers indicate results for PA-TFCs made on un-primed PES supports while the bar graph compares samples of similar thickness (30 LbL cycles results in an approximately 96 nm PA layer) formed on PVA-primed and bare (un-primed) PES supports. A salt rejection of 93% was measured for a commercially available membrane (DuPont FilmTec™ SW30XLE, ▲ and dotted line) and is plotted for comparison.

Using the PVA primer drove an increase in the salt rejection to within 6% of the commercial PA-TFC salt rejection (Figure 4b). Similar to the situation observed for water transport, this result suggests that the use of the PVA primer helps to mitigate defect formation and/or support degradation that may occur when LbL is performed on a bare (un-primed) microporous support. The LbL₃₀ on the PVA-primed support did not exhibit $\geq 95\%$ salt rejection

like the commercial PA-TFCs, but this observation may be related to specifics (e.g., use of additives or reaction conditions) of the industrial process.^{10,12} Further, continued methanol exposure during deposition may cause the polyamide to swell, which would result in a reduction in salt rejection.¹⁷ While additional data at lower cycles would inform the minimum number of cycles needed to form defect free membranes, 30 cycles deposited on the PVA layer may promote defect free PA layer formation.

From a practical perspective, increasing the resistance to salt transport is beneficial for desalination membrane development. Therefore, analyzing the contribution of the PVA layer to the resistance to salt transport is less critical compared to the situation for water transport. The small deviation between overall water permeance and PA layer water permeance noted previously (Table B3) likely would translate into a similar, if not smaller, situation with regard to salt transport because hydrated ions are larger than water molecules.

The use of a PVA primer when preparing LbL PA-TFC membranes may facilitate the PA layer formation process in a manner that is favorable to the separation properties of the membrane. In desalination, the combination of (or tradeoff between) water/salt selectivity (often taken to be the ratio of the water permeance to the salt permeance or A/B) and water permeance characteristics are important for the overall performance of the membrane. When the A and B values for the membranes considered here were analyzed, the water/salt (A/B) selectivity increased from $\sim 10^{-3}$ (LbL membranes prepared on the bare (un-primed) support) to 10^0 - 10^1 for LbL membranes prepared on PVA-primed supports. The selectivity values for the membranes made using the PVA primer were comparable to that of the commercially available SW30XLE membrane ($\sim 10^1$). With access to water/salt selectivity values that are more comparable to that of commercial membranes, the use of PVA-primed supports could provide an opportunity for

further investigation of structure-property relationships for PA-TFCs, and this approach could be critical for expanding such studies to incorporate different co-monomers as illustrated subsequently.

5.2.4. Charged Co-Monomer Incorporation

A potential benefit of LbL sequential deposition is that the approach may circumvent some of the thermodynamic and/or kinetic limitations that are inherent to the conventional interfacial polymerization process. These limitations may restrict options for incorporating different monomers or mixtures of co-monomers into the PA selective layer.²⁴ For example, a sulfonated polyamide, in principle, could be prepared via interfacial polymerization using a mixture of MPD and MPDSK diamines in the aqueous phase along with TMC in the organic phase.

Such an approach, however, could be subject to competition between the diamine co-monomers. The polyamide formation reaction occurs as amine- and acid chloride-containing molecules reach the reaction zone.² Therefore, the process is sensitive to mass transfer of co-monomers to the phase boundary, the solubility properties of the co-monomers, and the relative reactivity of the amine-containing co-monomers. The sulfonated diamine (MPDSK) is bulkier (i.e., mass transfer is slower), less soluble in organic solvent, and less reactive than MPD. Thus, by changing the diamine recipe, competition between the diamines could be introduced. These factors suggest that an attempt to use a mixture of MPDSK and MPD co-monomers along with TMC in a conventional interfacial polymerization process will likely result in a membrane containing few, if any, sulfonated co-monomers. Alternatively, the LbL sequential deposition process may alleviate some of the competition between the diamine co-monomers due to the fact that monomers are brought directly into contact with the reactive surface. Further, control over

the exposure time of each “layer” to the respective diamines (i.e. MPDSK or MPD) could allow the sulfonated diamine the appropriate time to interact with the exposed TMC contained primed support for higher likelihood of sulfonate group incorporation. To investigate this possibility, we prepared a sulfonated polyamide layer on a PVA surface by using both MPD and MPDSK diamines in the aqueous phase during the LbL polyamide sequential deposition process.

The choice to prepare a sulfonated polyamide layer was made because the incorporation of sulfonate groups in the membrane will drive an increase in the conductivity of the layer. Therefore, the presence of sulfonate groups in the polyamide layer can be verified via an in-plane conductivity measurement made on the membrane made using a mixture of MPD and MPDSK diamines. As PVA has a high ionic resistance (**Table 1**), the measured ionic resistance properties of the polyamide layers can be attributed solely to ion transport through the polyamide layer.

Table 1. In-plane ionic resistance and conductivity properties of membrane surfaces. The PVA layer has a very low conductivity, so conductivity increases (relative to that of PVA) following deposition of a polyamide layer on top of PVA can be attributed to the properties of the polyamide layer, as a negligible amount of current is expected to be pass through PVA.

Membrane Surface	Ionic Resistance [Ω]	Ionic Conductivity [mS]
PVA	$6.4 (\pm 0.2) \times 10^8$	$1.56 (\pm 0.05) \times 10^{-6}$
MPD-TMC Polyamide	1700 ± 49	0.59 ± 0.02
MPDSK-MPD-TMC Polyamide	902 ± 33	1.11 ± 0.04

The ionic conductivity of the MPD-TMC polyamide layer was orders of magnitude greater than that of the PVA layer (Table 1). When the LbL sequential deposition process was used with a mixture of MPDSK and MPD in the aqueous phase, the ionic conductivity of the polyamide layer increased (and the resistance decreased) relative to that of the un-sulfonated MPD-TMC polyamide membrane (Table 1). This proof-of-concept result suggests that the

sulfonated co-monomer (MPDSK) successfully incorporated into the polyamide layer prepared on PVA via the LbL sequential deposition process.

The viability of membranes made using different co-monomers (such as the example shown here for the sulfonated co-monomer) may depend on an ability to prepare a defect free selective layer on a support membrane. The use of LbL sequential deposition combined with the use of a PVA primer could be one approach to reaching that goal. Furthermore, it complements other studies where, for example, polyelectrolytes have been used as a primer layer for sequential deposition of polyamide selective layers.

5.3. Conclusions

In the absence of the PVA primer, LbL deposition of a PA layer on microporous supports likely leads to defective membranes. By priming the support using PVA, we demonstrate a promising method for controlled PA-TFC membrane formation. Priming the microporous support with PVA both protects the microporous support from the organic solvents used in the process and provides a reactive surface for PA layer growth. Furthermore, the PVA priming process could enable the use of polyamide barrier layers with a range of different supports because the presence of PVA could make the polyamide deposition process less sensitive to the specific underlying support membrane. A series resistance model suggests that the contribution of the PVA primer to the overall mass transfer resistance of the composite membrane is relatively small. Therefore, a combination of the LbL sequential deposition process and PVA-primed microporous supports may enable co-monomer incorporation into the PA layer that would otherwise not be feasible using the traditional IP process because of solubility, diffusivity, and/or reactivity limitations.

5.4. References

- (1) Geise, G. M.; Lee, H.-S.; Miller, D. J.; Freeman, B. D.; McGrath, J. E.; Paul, D. R. Water Purification by Membranes: The Role of Polymer Science. *J. Polym. Sci. Part B Polym. Phys.* **2010**, *48*, 1685–1711. <https://doi.org/10.1002/polb.22037>.
- (2) Freger, V. Kinetics of Film Formation by Interfacial Polycondensation. *Langmuir* **2005**, *21* (5), 1884–1894. <https://doi.org/10.1021/la048085v>.
- (3) Kong, C.; Shintani, T.; Kamada, T.; Freger, V.; Tsuru, T. Co-Solvent-Mediated Synthesis of Thin Polyamide Membranes. *J. Memb. Sci.* **2011**, *384* (1–2), 10–16. <https://doi.org/10.1016/j.memsci.2011.08.055>.
- (4) Saha, N. K.; Joshi, S. V. Performance Evaluation of Thin Film Composite Polyamide Nanofiltration Membrane with Variation in Monomer Type. *J. Memb. Sci.* **2009**, *342* (1–2), 60–69. <https://doi.org/10.1016/j.memsci.2009.06.025>.
- (5) Ghosh, A. K.; Jeong, B. H.; Huang, X.; Hoek, E. M. V. Impacts of Reaction and Curing Conditions on Polyamide Composite Reverse Osmosis Membrane Properties. *J. Memb. Sci.* **2008**, *311* (1–2), 34–45. <https://doi.org/10.1016/j.memsci.2007.11.038>.
- (6) Ahmad, A. L.; Ooi, B. S. Properties-Performance of Thin Film Composites Membrane: Study on Trimesoyl Chloride Content and Polymerization Time. *J. Memb. Sci.* **2005**, *255* (1–2), 67–77. <https://doi.org/10.1016/j.memsci.2005.01.021>.
- (7) Hermans, S.; Bernstein, R.; Volodin, A.; Vankelecom, I. F. J. Study of Synthesis Parameters and Active Layer Morphology of Interfacially Polymerized Polyamide-Polysulfone Membranes. *React. Funct. Polym.* **2015**, *86*, 199–208. <https://doi.org/10.1016/j.reactfunctpolym.2014.09.013>.
- (8) Johnson, P. M.; Yoon, J.; Kelly, J. Y.; Howarter, J. A.; Stafford, C. M. Molecular Layer-by-Layer Deposition of Highly Crosslinked Polyamide Films. *J. Polym. Sci. Part B Polym. Phys.* **2012**, *50* (3), 168–173. <https://doi.org/10.1002/polb.23002>.
- (9) Chan, E. P.; Lee, J. H.; Chung, J. Y.; Stafford, C. M. An Automated Spin-Assisted Approach for Molecular Layer-by-Layer Assembly of Crosslinked Polymer Thin Films. *Rev. Sci. Instrum.* **2012**, *83* (11). <https://doi.org/10.1063/1.4767289>.
- (10) Chowdhury, M. R.; Steffes, J.; Huey, B. D.; McCutcheon, J. R. 3D Printed Polyamide Membranes for Desalination. *Science (80-.)*. **2018**, *361* (6403), 682–686.

<https://doi.org/10.1126/science.aar2122>.

- (11) Gu, J. E.; Lee, S.; Stafford, C. M.; Lee, J. S.; Choi, W.; Kim, B. Y.; Baek, K. Y.; Chan, E. P.; Chung, J. Y.; Bang, J.; Lee, J. H. Molecular Layer-by-Layer Assembled Thin-Film Composite Membranes for Water Desalination. *Adv. Mater.* **2013**, *25* (34), 4778–4782. <https://doi.org/10.1002/adma.201302030>.
- (12) Choi, W.; Gu, J. E.; Park, S. H.; Kim, S.; Bang, J.; Baek, K. Y.; Park, B.; Lee, J. S.; Chan, E. P.; Lee, J. H. Tailor-Made Polyamide Membranes for Water Desalination. *ACS Nano* **2015**, *9* (1), 345–355. <https://doi.org/10.1021/nn505318v>.
- (13) Geise, G. M. Why Polyamide Reverse-Osmosis Membranes Work so Well. *Science* (80-.). **2021**. <https://doi.org/10.1126/science.abe9741>.
- (14) Van Krevelen, D. W.; Te Nijenhuis, K. Properties of Polymers. In *Properties of Polymers*; 2009; pp 71–107. <https://doi.org/10.1016/B978-0-08-054819-7.X0001-5>.
- (15) Bondi, A. Van Der Waals Volumes and Radii. *J. Phys. Chem.* **1964**, *68* (3), 441–451. <https://doi.org/10.1021/j100785a001>.
- (16) Mavukkandy, M. O.; McBride, S. A.; Warsinger, D. M.; Dizge, N.; Hasan, S. W.; Arafat, H. A. Thin Film Deposition Techniques for Polymeric Membranes– A Review. *J. Memb. Sci.* **2020**. <https://doi.org/10.1016/j.memsci.2020.118258>.
- (17) Xia, L.; McCutcheon, J. R. Understanding the Influence of Solvents on the Intrinsic Properties and Performance of Polyamide Thin Film Composite Membranes. *Sep. Purif. Technol.* **2020**. <https://doi.org/10.1016/j.seppur.2019.116398>.
- (18) Bolto, B.; Tran, T.; Hoang, M.; Xie, Z. Crosslinked Poly(Vinyl Alcohol) Membranes. *Progress in Polymer Science (Oxford)*. 2009. <https://doi.org/10.1016/j.progpolymsci.2009.05.003>.
- (19) Freger, V. Swelling and Morphology of the Skin Layer of Polyamide Composite Membranes: An Atomic Force Microscopy Study. *Environ. Sci. Technol.* **2004**. <https://doi.org/10.1021/es034815u>.
- (20) Mulhearn, W. D.; Oleshko, V. P.; Stafford, C. M. Thickness-Dependent Permeance of Molecular Layer-by-Layer Polyamide Membranes. *J. Memb. Sci.* **2021**, *618*, 118637. <https://doi.org/10.1016/j.memsci.2020.118637>.
- (21) Xia, L.; Ren, J.; Weyd, M.; McCutcheon, J. R. Ceramic-Supported Thin Film Composite Membrane for Organic Solvent Nanofiltration. *J. Memb. Sci.* **2018**, *563*, 857–863.

<https://doi.org/10.1016/j.memsci.2018.05.069>.

- (22) Wang, Y.; Hsieh, Y.-L. Crosslinking of Polyvinyl Alcohol (PVA) Fibrous Membranes with Glutaraldehyde and PEG Diacylchloride. *J. Appl. Polym. Sci.* **2010**, *116* (6), 3249–3255. <https://doi.org/https://doi.org/10.1002/app.31750>.
- (23) Jian, S.; Xiao Ming, S. Crosslinked PVA-PS Thin-Film Composite Membrane for Reverse Osmosis. *Desalination* **1987**, *62* (C), 395–403. [https://doi.org/10.1016/0011-9164\(87\)87040-6](https://doi.org/10.1016/0011-9164(87)87040-6).
- (24) Sosa-González, W. E.; Palí-Casanova, R. del J.; Pérez-Padilla, Y.; Loría-Bastarrachea, M. I.; Santiago-García, J. L.; Aguilar-Vega, M. de J. Sulfonated Aromatic Copoly(Ether–Amide) Membranes II: Influence of Chain Length and Sulfonic Groups Concentration on Membrane Ionic Conductivity and Mechanical Properties. *High Perform. Polym.* **2018**. <https://doi.org/10.1177/0954008317699863>.

Chapter 6: Layer-by-Layer “Sandwiched” Synthesis of UiO66-NH₂-containing Polyamide Thin-Film Nanocomposite Membranes for Nanofiltration Applications

In the previous project, the extension of LbL synthesis of the PA on microporous supports was assessed via RO-based water and salt transport as well as through a series resistance model analysis of the individual layer the resistances to mass transfer. This study assesses the application of a similar spin-coater based sequential deposition technique for the full encapsulation of UiO66-NH₂ into the PA layer through water, salt, and dye transport measurements. Further, a similar series resistance model is applied to draw PA layer specific structure/property relationships geared towards NF applications.

6.1. Introduction

Nanofiltration is a pressure-driven membrane-based separation and purification technique used for drinking water treatment, dye separation, pharmaceuticals, and heavy removal and organic solute removal.¹⁻⁶ Polyamide thin-film composite (PA-TFC) membranes are the leading membrane technology for nanofiltration (NF) as the thin selective polyamide layer can be tuned individually to optimize membrane performance for high water transport and solute rejection.^{2-4,7,8} This is particularly useful in combatting the well-known selectivity/permeability tradeoff for water and solute transport observed for polymer membranes in this space.^{1,4,5,7,9,10} The development of polyamide thin film nanocomposite (PA-TFN) membranes via the incorporation of metal organic frameworks (MOFs) has progressed significantly over the past decade years to combat the selectivity/permeability tradeoff observed for commercial PA-TFC membranes used in NF. The interruption of an originally highly cross-linked polyamide structure with an organometal compound facilitates increased water transport through interrupting the polymer matrix, creating increased polyamide free volume as well as instituting distinct pores, through

the metal node, that provide additional water transport pathways.^{1,4,5,7-9} Further, the introduction of the MOF to the polymer matrix, provides an opportunity to expand diffusion/sorption based solute rejection to distinct size-sieving through the well-defined pores of the metal node, maintaining, if not exceeding, current standards for NF solute rejection.^{1,4,5,7-9} Researchers have successfully incorporated a number of porous nanomaterials such as ZIF-8 and UiO-66 and shown that with these MOFs in the composite structure an increase in water permeance with comparable, if not higher, large solute rejection can be obtained.^{1,3-5,7-13}

However, there are two key obstacles for the optimization of PA-TFN membrane synthesis for NF: aggregation of the MOF particles within the polyamide layer and particle leaching.^{1-4,7-10,14} PA-TFN membranes are typically synthesized via interfacial polymerization of *m*-phenylene diamine (MPD) and trimesoyl chloride (TMC) with the zeolite-based nanoparticle suspended in either the organic or aqueous solution phase. Poor dispersion of the MOF particles in the respective reaction phase can result in high surface energy induced particle-particle aggregation. Further, poor chemical compatibility between the MOF and the polymer backbone can also promote aggregation resulting in decreased separation performance.^{4,7,8} MOF leaching is typically a result of both poor compatibility between the MOF and the polymer backbone as well as size-matching between the MOF and the PA layer.^{1,3,4,7-10,14} Interfacial polymerization typically requires the removal of excess monomer solution to maintain a consistent PA layer so in addition to poor chemical attachment of the MOF particles into the composite structure, MOF particles that are too large can also contribute to a reduction in separation performance due to poor MOF incorporation in the PA layer.⁴

Besides the introduction of additional pre-synthesis MOF solution processing, researchers have explored functionalized versions of typical MOFs, like UiO66-NH₂, to address aggregation

and leaching through improving the reactivity of the MOF itself. The amino-functional group acts as an anchor for the MOF to the greater polyamide structure by covalently bonding to it creating a preference for MOF-polymer interaction rather than the MOF-MOF interaction.^{3,4,7-10,12-14} Researchers have been successful in incorporating UiO66-NH₂ in both the polyamide layer itself as well as anchored to the support and subsequently observed increased water transport as well as superior multivalent ion and organic dye rejection.^{3,4,7-10,12-14} However, the use of interfacial polymerization for PA-TFN synthesis of UiO66-NH₂ membranes restricts the ability to speak to the structure/property relationships of the PA layer specifically. Further, the larger body of work in this area works with MOF particles ~ 100 nm in size, making size-matching for good particle embedding more difficult.^{7,9,10}

Here, we discuss the synthesis of a UiO66-NH₂-containing PA-TFN membrane via a controlled spin-coater based layer-by-layer “sandwiched” synthesis on a PVA-primed support to assess the PA layer specific performance as a result of incorporating the MOF. Through this sequential deposition process, assessed for RO-made PA layers in Chapter 5, we take advantage of the known high reactivity of UiO66-NH₂ and known thickness per cycle growth pattern of the PA layer to ensure full encapsulation of these 20-50 nm MOF particles.¹⁵ The NF performance is assessed through pressure-driven water permeance, multivalent rejection (i.e. MgSO₄) and dye rejection (i.e. congo red, methylene blue, methyl orange). This analysis is extended, similar to prior work, through the application of a resistance in series model to determine the contribution to mass transfer resistance of each composite layer and elucidate meaningful structure/property relationships for the PA layer.¹⁵

6.2. Results and Discussion

6.2.1. UiO66-NH₂ Characterization

UiO66-NH₂ particles were characterized through scanning electron microscopy (SEM), X-ray Diffraction (XRD), and Brunauer-Emmett-Teller (BET) surface area and N₂ adsorption analysis. MOF particles were synthesized via an optimized aqueous UiO66- NH₂ synthesis procedure, described elsewhere.¹⁶ Figure 1A shows a similar XRD pattern to that of previous literature where peaks at 7, 8, and 25 degrees were observed representing the (111), (002) and (006) planes of UiO66-NH₂.^{4,7,10,12,13,16-18} SEM imaging of UiO66-NH₂ (Figure 1B) show crystalline particles of approximately 20-50 nm suggesting full encapsulation in the “sandwiched” PA layer is possible between PA layers of known thickness’ of ~48 nm each. It is important to note that the range of particle sizes could be due to aggregation of MOF common at high membrane loadings.^{1,7,17,19,20} These small crystalline particles are able to maintain a large surface area of 870.46 m²/g with a pore size of 5.9 Å (Figure 1C) suitable for transport of water molecules (2.7 Å) as well as selective to dye transport (11.84 Å – 23.13 Å) while sustaining a comparable N₂ adsorption of 328 cm³/g STP (Figure 1D).^{10,13,17}

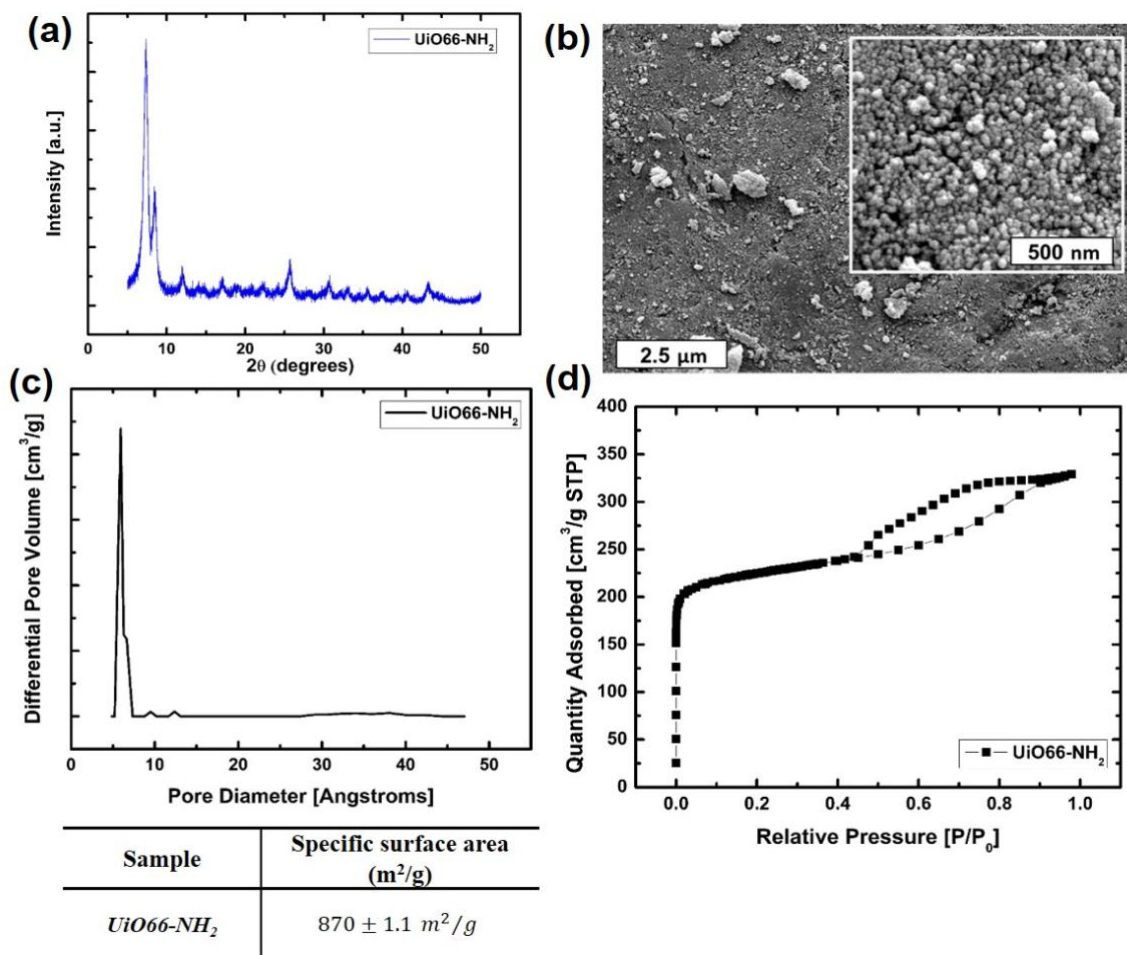


Figure 1: UiO66-NH₂ characterization a) XRD scans of UiO66-NH₂; b) SEM imaging of synthesized UiO66-NH₂; c) Pore Size distribution obtained via BET highlighting 5.9 Å pore size of MOF particles; specific surface area of UiO66-NH₂ = 870 ± 1.1 m²/g; d) N₂ adsorption trend with relative pressure for UiO66-NH₂

6.2.2. PA-TFN Membrane Characterization

After “sandwiched” LbL synthesis (Figure 2 in Chapter 4), thermogravimetric analysis (TGA) and Fourier-transform infrared spectroscopy (FTIR) were used to respectively determine the MOF loading and confirm the formation of the polyamide.^{7,21} As only Zr from the MOF should remain after 800C, the final weight percent of material was assumed to represent the MOF loading in the membrane and related to the MOF solution concentration (Table 1).²¹ The MOF loadings represented in Table 1 suggest that between the MOF solution concentration (in

mg/mL) does not scale directly to the MOF loading in the membrane (wt%) suggesting that as the MOF solution concentration increases, the way the MOF incorporates into the PA layer changes. This is observed similarly through the slight decrease in MOF loading from 0.5 mg/mL MOF solution concentration to 1 mg/mL suggesting a difference in the mechanism in which the MOF incorporates into the PA layer.

MOF Solution Concentration (mg/mL)	Measured MOF Loading via TGA (wt%)
<i>0.2 mg/mL</i>	0.058 ± 0.006 wt%
<i>0.5 mg/mL</i>	0.41 ± 0.004 wt%
<i>1.0 mg/mL</i>	0.36 ± 0.003 wt%
<i>2.0 mg/mL</i>	1.1 ± 0.002 wt%

Table 1: MOF solution concentration in mg/mL with corresponding measured MOF loading determined using TGA scans shown in Figure C.1.

The formation of the PA layer in the presence of UiO66-NH₂ was confirmed using FTIR (Figure 2).⁷ Figure 2A shows that in comparison to the baseline PVA substrate, key peaks between 1680 cm⁻¹-1630 cm⁻¹, consistent with Amide I, C=O stretching for the secondary amine, 1640 cm⁻¹- 1600 cm⁻¹, representing the hydrogen-bonded C=O bond, and between 1570 cm⁻¹-1515 cm⁻¹, representing amide II, N-H in-plane bending consistent with NH₂ deformation are present, consistent with the formation of the aromatic polyamide. A suppression of the PA peaks is observed after the addition of UiO66-NH₂ (Figure 2B), however the subtle return in the amide II peak (1570 cm⁻¹ – 1515 cm⁻¹) could suggest the incorporation of the NH₂ functionalized MOF into the PA layer.⁷

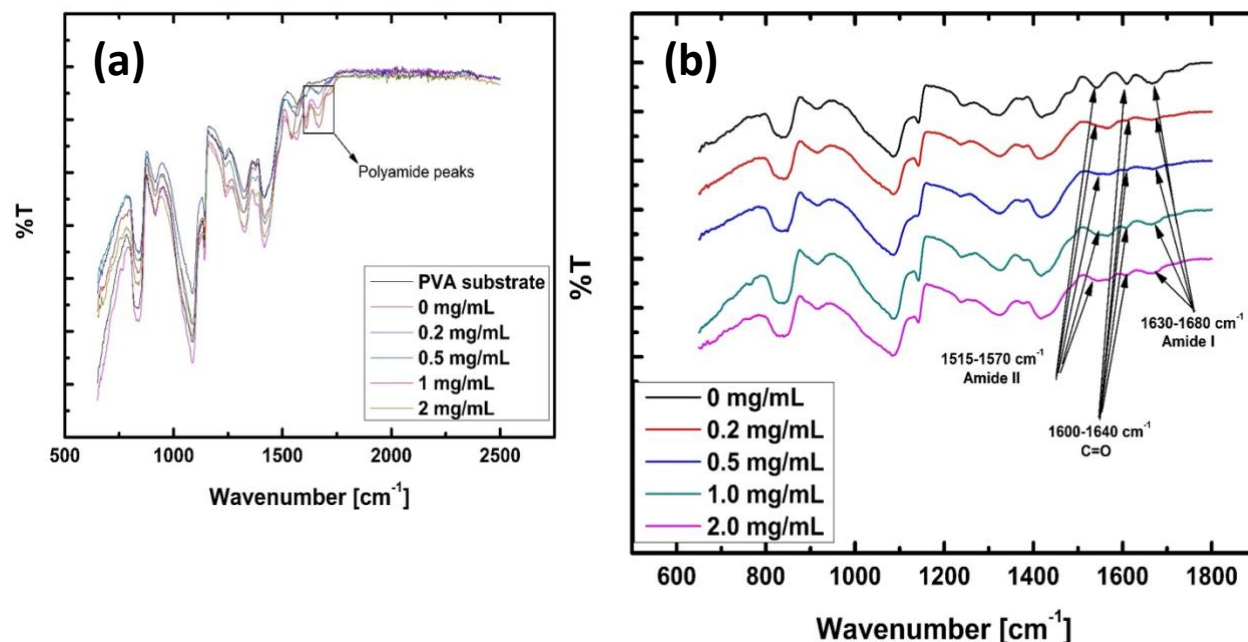


Figure 2: FTIR scans for a) baseline PVA substrate, used for characterization, and the PA coated PVA substrates made with varying MOF solution concentration; b) just the PA coated PVA substrates made with varying MOF solution concentrations zoomed in to highlight key polyamide peaks.

Finally, cross-sectional SEM images of PA-TFC and PA-TFN membranes were used to observe the changes in the PA layer as the MOF solution concentration increases (Figure 3).^{7,14,20,22,23} Overall, after the addition of UiO66-NH₂, that yields to less uniformly dense PA layer.^{1,7,10,17,19,24} This is a reasonable observation as the increased addition of the NH₂-functionalized MOF is expected to interfere with the polyamide chain packing, opening the pore structure of the selective layer.⁷ However, the “openness” of the PA layer does not scale directly with the MOF solution concentration. More specifically, at 1 mg/mL (Figure 3D) there seems to be a more open pore structure than at 2 mg/mL (Figure 3E). Further, a densely packed PA layer is observed at 0.5 mg/mL (Figure 3C) while at a similar MOF loading, Figure 3D shows an almost 30 nm pore structure in the PA layer of the PA-TFN with 1 mg/mL MOF solution concentration. These observations suggests that as the MOF is incorporated into the PA layer, the

structure of the PA layer itself changes and is most settled at very low or very high MOF loadings. This observation could be a result of the initial interference in the polyamide chain packing that results in inconsistent PA layer growth at low to moderate MOF loadings.⁷

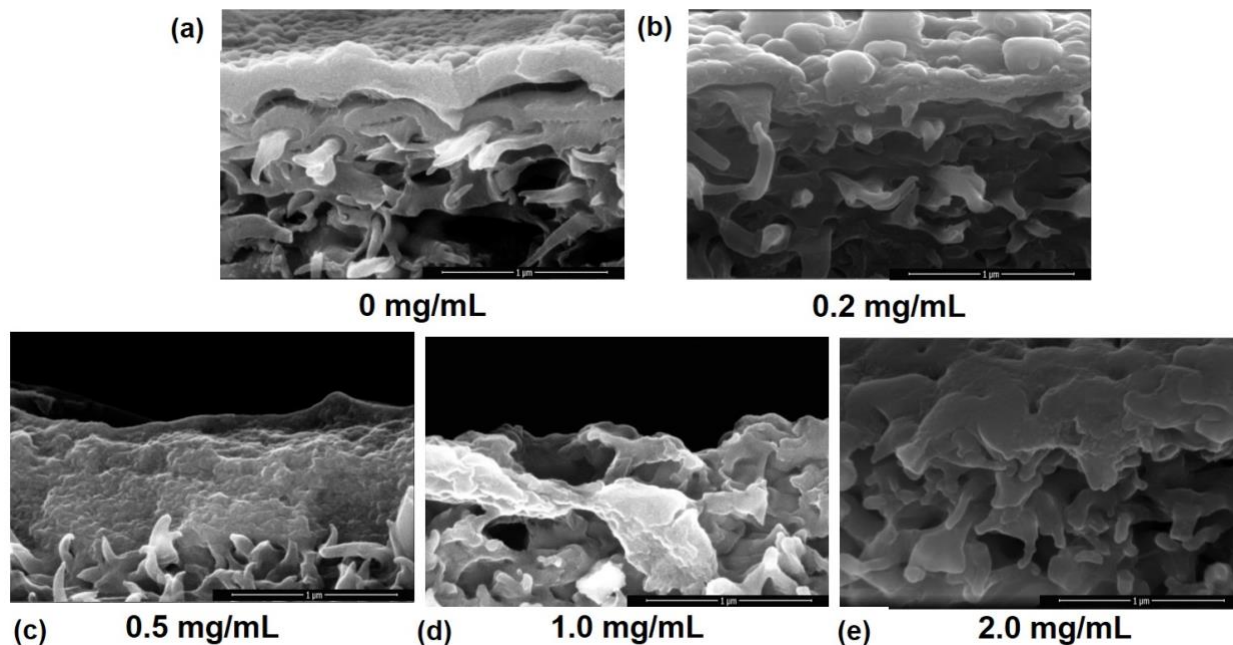


Figure 3: SEM imaging for the UiO66-NH₂ containing PA-TFN of varying MOF solution concentration a) 0 mg/mL; b) 0.2 mg/mL; c) 0.5 mg/mL; d) 1 mg/mL; e) 2 mg/mL

In addition to confirming the formation of UiO66-NH₂-containing PA-TFN membranes with varying loadings, the above characterization implies that the PA layer structure is changing both chemically and visually. With the changing PA layer structure it would be reasonable to expect a change in the composite membrane performance as the MOF loading increases. Further, the indirect scaling relationship between MOF solution concentration (mg/mL) and loading (wt%), Table 1, paired with varied opening of the PA pore structure as the solution concentration increases suggests greater variability in the incorporation of the MOF at low to moderate MOF loadings. This suggests that there may be a settling point for MOF loading where a more consistent incorporation of the MOF, similar to that observed in Figure 3E, and therefore more consistent composite membrane performance.

The water and salt transport of the LbL-made PA-TFN membranes were assessed via the water permeance (Figure 4) and the MgSO_4 rejection (Figure 5A). The water permeance data and additional NaCl permeance data were then used to determine the water/salt selectivity, A/B, (Figure 5B). These preliminary results suggest that not only does the water permeance of all LbL-based PA-TFN membranes exceed that of the baseline LbL-made PA-TFC membrane, but, this synthesis has allowed us to shift the performance of our previously studied reverse osmosis composite membrane (Figure 6B – star) to the nanofiltration regime performance.¹⁵

6.2.3. Water Transport

Figure 4A shows the increasing water permeance for LbL-made PA composite membranes of as MOF loading increasing. It is important to note that as TGA confirmed a higher MOF loading at 0.5 mg/mL MOF solution concentration, it is been represented as such in the graph. To more accurately compare the membrane synthesized without the MOF and our “sandwiched” PA-TFN synthesis reported here, PA-TFN membrane water permeance values normalized to the baseline PA-TFC membrane, discussed in Chapter 5.¹⁵ In alignment with our initial hypothesis, a significant increase in water permeance is observed for all composite membranes containing MOF when compared to the baseline PA-TFC membrane. This is consistent with previous literature of both general nanoparticle incorporation via interfacial polymerization as well as previous work specifically with UiO66-NH_2 .^{19,24,13,17} Figure 4B shows that for MOF loadings above 0.4 wt%, the water permeance is increased by at least four times the baseline LbL-made PA-TFC membrane, exceeded the approximate two-fold increase in water permeance observed by Zhang et al. with their UiO66-NH_2 coated substrate-based PA-TFN membranes.²⁵

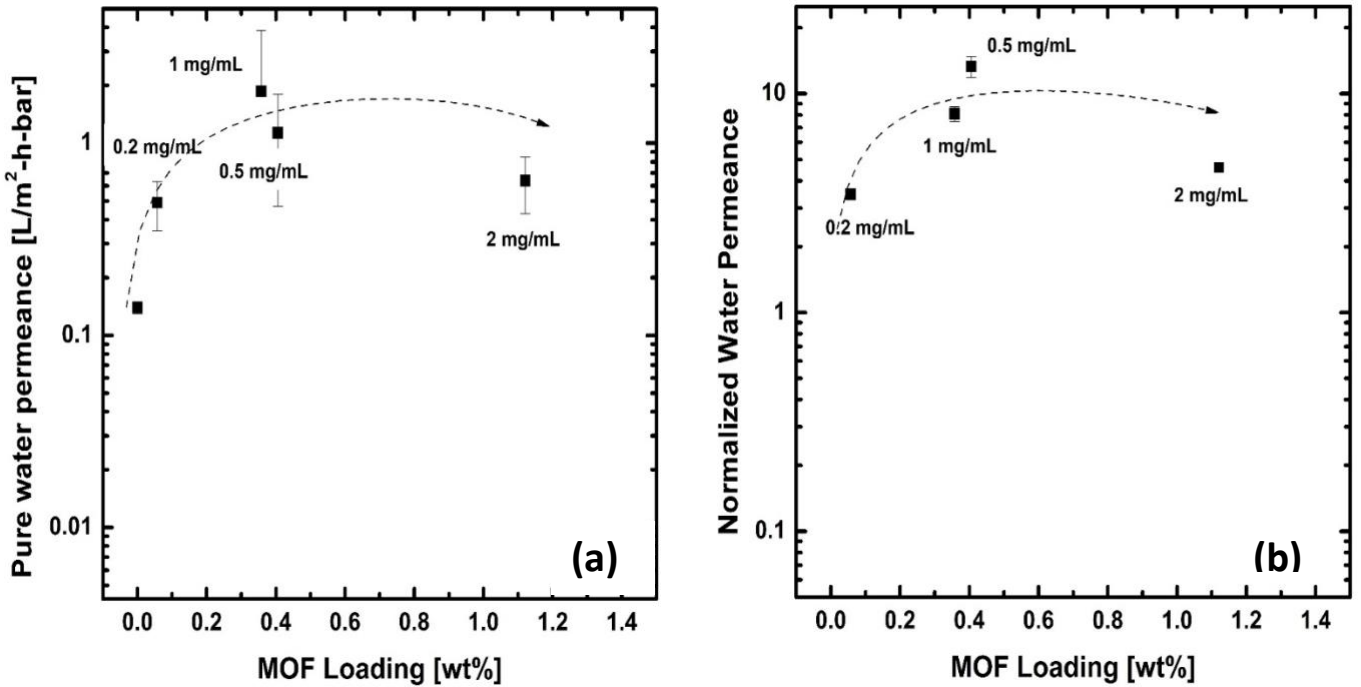


Figure 4: a) Pure water permeance versus MOF loading in wt% b) pure water permeance for PA-TFN samples normalized by 0 mg/mL PA-TFC membrane sample versus MOF loading in wt%

The increase in water permeance after the addition of UiO66-NH₂ can be attributed to the incorporation of additional water channels through the MOF coupled with the more open pore structure of the PA layer due to a disruption of polymer chain packing during synthesis.^{1,7,14,17,20} This is reasonable as the known UiO66-NH₂ particle 5.9 Å pore size will facilitate transport of water molecules (2.76 Å) while selectively transport multivalent salt and organic impurities (> 5.9 Å).¹⁷ However, the addition of increased transport channels resulting in increased water permeance seems to plateau as more MOF is added, evidenced by its logarithmic trajectory with MOF loading. Further, at the highest MOF loading of 1.12 wt%, the water permeance drops from 1.86 L/m²h – bar to 0.64 L/m²h – bar suggesting particle-particle affinity driven aggregation blocking the MOF pores could be taking place.²⁰

It has been shown that the distribution of the MOF in the PA layer can contribute to the institution of these transport channels and therefore the mass transport of the composite membrane. More specifically, MOF that is more well-distributed within the PA layer has been shown to result in higher membrane water permeance and multivalent salt rejection.²⁵ Though LbL is a spin coater-based process known for even distribution of deposited solutions and the dependence on diffusion of the MOF to a reaction interface is circumvented via use of the same organic solvents for all reactants, increased MOF loading can nevertheless result in poor distribution of the MOF with the PA layer resulting in aggregation. These trends imply that there is an initial MOF loading regime where the performance improves significantly, followed by a range of loadings of similar performance suggesting a sort of “settling” of the modified PA layer and finally a drop in performance at relatively high loadings due to aggregation.²⁰ However, within all MOF loading regimes, full incorporation of the MOF into the composite structure is paramount as it allows for the specific effect of MOF addition to the PA layer to be elucidated.

Full incorporation of the MOF into the composite membrane structure results in both a less wasteful synthesis process and minimized particle-particle aggregation responsible for the reduction of water transport pathways.^{13,20,25,26} Further, PA-TFN membranes containing well embedded MOFs provide the ability to more readily tie the membrane synthesis conditions (i.e. MOF solution concentration in mg/mL) to the membrane structure characteristics (i.e. MOF loading in wt%) to derive meaningful trends in performance (water and solute transport). The amine functional group in UiO66-NH₂ increases the reactivity of the MOF with the acyl chlorides present during PA layer synthesis resulting in better incorporation within the PA layer, when compared with UiO66, evidenced in a greater increase in water transport for composite membranes.^{13,20,25,26} However, prior work with UiO66-NH₂-containing PA-TFN membranes

suggest that a similar drop in water permeance at relatively high MOF loading could be the result of particle-particle aggregation previously observed with non-functionalized MOF-containing composite membranes.^{13,20,25,26}

Researchers have combatted UiO66-NH₂ aggregation in IP-based synthesis techniques through sonication of the MOF solution, to initially minimize particle-particle interactions, and direct deposition of the MOF to a modified porous support prior to IP.^{13,20,25,26} Though these methods have been shown to minimize aggregation and show promising NF performance, sonication alone only delays aggregation and the modification of the porous support with MOF particles hinders the capability to deconvolute the effect on composite membrane performance of the modified PA layer itself, making it difficult to derive meaningful structure-property relationships. LbL “sandwiched” deposition employs sonication of the MOF solution prior to synthesis while allowing for full “sandwich” incorporation of the MOFs between PA layers of known thickness through a centrifugal force-driven deposition process. By leveraging the consistent radial outflow of the spin coater-based process, LbL “sandwiched” deposition evenly distributes the MOF solution on a reactive PA-coated primed support, reducing the likelihood of particle-particle aggregation at moderate MOF loadings. [dip vs. spin coater process source]

Though the drop in water permeance at 1.12 wt% suggests particle-particle aggregation could be blocking the additional water transport pathways within the porous MOF particles, further optimization of the LbL “sandwiched” synthesis procedure for higher MOF loadings could provide the opportunity to further expand the range of loadings in which aggregation is minimized. More specifically, the application of multiple MOF cycles separated by PA “buffer” layers could provide additional distance between MOF particles while allowing for higher MOF loadings to be obtained with lower MOF solution concentration. With a known MOF-containing

PA layer thickness, we can derive PA layer specific structure/property relationships for further minimization of particle-particle aggregation within the PA layer. This information can then be used to consider the tradeoff between improved water transport due to increased MOF loading and the reduction in water transport due to increased PA layer thickness.

6.2.4. Salt Transport and Permeability/Selectivity Tradeoff

Figure 5A shows the MgSO_4 rejection of ranging MOF loading (0 – 1.12 wt%) as compared to commercial NF PA-TFC membrane standard (Synder NFG). These results show that with the addition of UiO66-NH₂ to the PA layer a similar mass permeance trend is observed: an initial spike in mass permeance (drop in solute rejection) followed by a plateau and finally drop in mass permeance (increase in solute rejection). All PA-TFN membrane samples maintained values of MgSO_4 rejection comparable to the commercial NF standard. Figure 5B shows the water/NaCl permeance selectivity versus water permeance for the baseline LbL-made PA-TFC membrane and all PA-TFN membranes. These points are plotted on a log-log scale to compare to the well-defined “upper-bound” of PA-TFC membrane performance divided into regimes based on specific membrane-based separation process.²⁷ The significant shift in water/salt selectivity observed for PA-TFN membranes tested coupled with their comparable MgSO_4 rejection to an NF standard suggests that this LbL “sandwiched” synthesis process has enabled the shift of an RO PA layer to that fitting with water/salt selectivity metrics of NF.

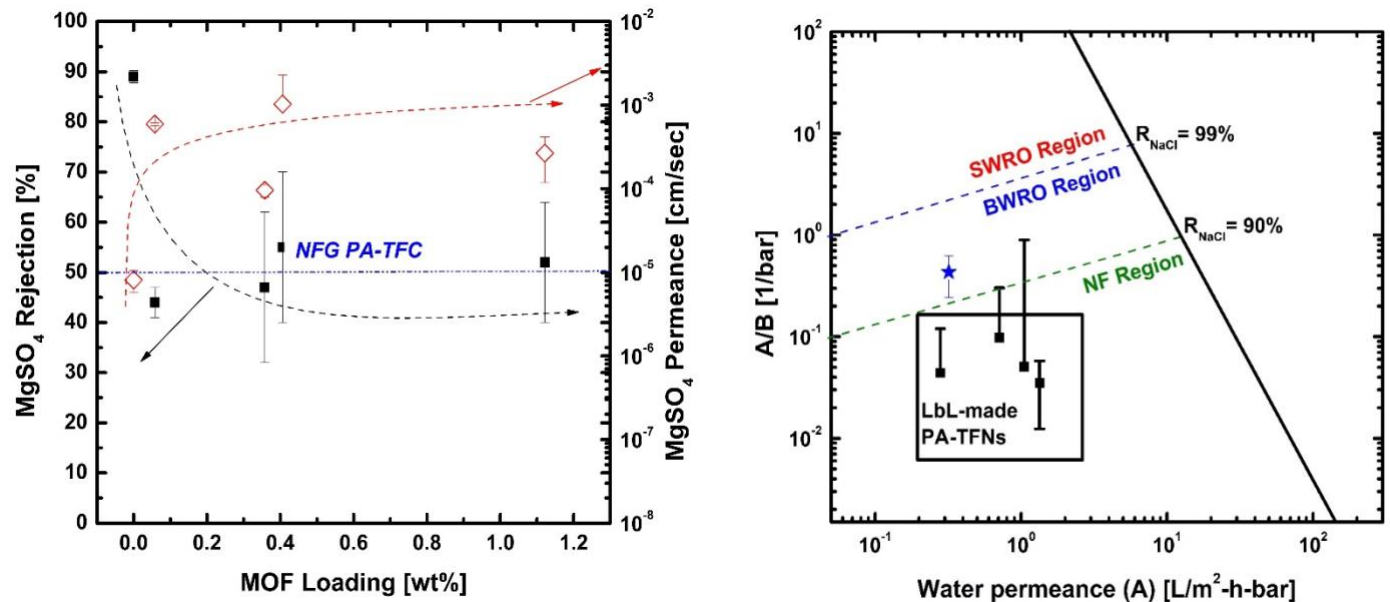


Figure 5: a) MgSO₄ rejection (%) [black squares] and permeance (cm/sec) [red open diamond] versus MOF loading in wt%; b) water/NaCl selectivity (1/bar) versus water permeance (L/m²h – bar) for the baseline PA-TFC membrane without MOF [blue star] and MOF-containing PA-TFN membranes [black squares]

NF-based desalination is used for multivalent brackish water desalination, water softening, and heavy-metal/organic matter removal and as such the rejection of divalent salts is an important metric of efficiency.^{7,12,13,26} Figure 5A shows that after the addition of MOF to the PA layer, the MgSO₄ rejection of the composite membrane drops from 89% to 44% - 55%). This observation is reasonable as the interruption of polymer chain packing as a result of the MOF addition creates a more open pore structure and, similar to water transport, increases solute transport, subsequently decreasing solute rejection.⁷ Also similar to water transport, after the initial increase in solute permeance (decrease in solute rejection) a plateau reached where, as described above, the MOF seems to “settle” into the PA layer. Finally, an order of magnitude drop in MgSO₄ permeance from 21 L/m²h to 9.6 L/m²h is observed due to aggregation in higher MOF loadings. It is important to note that though aggregation improves the salt rejection performance, it is also most likely contributing to the higher variability in salt rejection at higher

MOF loading suggesting less controlled MOF incorporation is taking place.¹⁷ An LbL “sandwiched” synthesis procedure involving multiple low MOF solution concentration cycles and possible PA ‘buffer’ layers could separate MOF particles, delaying aggregation, yet take advantage of their moderate loading size sieving capabilities.

The intrinsic water transport properties of PA-TFC membranes are evaluated using a “performance trade-off” plot comparing the water/NaCl permeance-selectivity (A/B) and the water permeance (A).⁵ Using performance data for both reverse osmosis and nanofiltration PA-TFC membranes, Yang et al defined an “upper-bound” for this trade-off relationship and divided it into regimes specific to the membrane-based desalination process. Figure 5B shows an order of magnitude shift in A/B selectivity from 0.43 1/bar to 0.03-0.09 1/bar after the addition of MOF to the PA layer. These results suggest that with the addition of MOF to the PA layer the initially RO composite membrane has been tuned to the NF regime.

A drop in A/B selectivity for NF membranes overall is reasonable as they are designed with a more open PA pore structure. The open polymer pore structure facilitates greater water transport, and thus PA-TFC membranes made for NF are expected to have a lower threshold of monovalent salt rejection (~90% NaCl rejection) when compared to PA-TFC membranes designed for RO (~99% NaCl rejection).²⁷ Further, as A/B selectivity is directly related to salt rejection, the lower monovalent salt rejection threshold for NF membranes corresponds to a lower regime of expected A/B selectivity. Within each separation process regime, a higher A/B selectivity is directly correlated with a higher salt rejection and thus suggests a more efficient purification process will take place as the monovalent salt rejection threshold is approached.²⁷ Water/salt permeance selectivity is typically improved by amending polymer synthesis to either increase water permeance or reduce salt permeance.²⁷ However, the upper-bound curve for PA-

TFC membranes highlights the tradeoff between these two goals as the addition of transport pathways yielding to higher water permeance directly counters the need for a dense and highly-crosslinked polymer structure for reduced salt permeance.²⁷

The addition of size selective MOFs like UiO66-NH₂ provides the opportunity to tune within this tradeoff relationship as the fixed pores within the MOF are designed to be large enough to allow water molecules through (> 2.76 Å) but small enough to keep multivalent ions and organic pollutants out. Within PA-TFN membrane results shown, a greater percentage change in A/B selectivity of 308% is observed when compared to the percentage change in water permeance of 178% over MOF loadings tested (Figure 5B). These results suggest a greater change in NaCl transport than water transport is occurring over the range of MOF loadings tested. The ability to conceivably control the solute transport with MOF loading, further emphasizes our ability to tune the PA layer to the NF regime. Additionally, as the PA-TFN membranes tested have been shown to be within the NF regime, it is reasonable to expect an even greater difference in percent change of A/B selectivity when compared to water permeance when larger organic pollutants, like dyes are considered.

In summary, the NF-range MgSO₄ rejection and A/B selectivity values of the all MOF loadings tested suggest that the addition of MOF via LbL “sandwiched” synthesis of the polyamide results in a shift in the originally RO geared PA layer to the NF regime. More specifically, a greater percentage change in water/NaCl permeance-selectivity than water permeance suggesting the ability to maintain high water transport while tuning for improved solute removal. With this pattern observed for NaCl, a monovalent salt with a significantly smaller hydrated diameter than organic pollutant dyes, a greater difference between A/B selectivity and water permeance change with increasing MOF loading is expected. With the

greater ability to size sieve for large organic pollutants as MOF loading increases, A/B selectivity can be optimized via both high water permeance and low solute permeance.

6.2.5. Dye Rejection

Nanofiltration is an important step in the removal of organic components for large organic water purification and pharmaceutical production.^{18,28} Rejection of dyes [Methyl Orange (MO), Methylene Blue (MB), and Congo Red (CR)] is a preliminary indicator of nanofiltration performance as they are a safer experimental alternative to harmful organic endocrine disruptors and pharmaceuticals of comparable molecular size.²⁸ Figure 6 shows that the addition of MOF results in both higher solute rejection for dyes than multivalent ions as well as more efficient large organic impurity removal, when compared to a lab-made PA-TFC membrane baseline, when incorporated via LbL “sandwiched” synthesis.

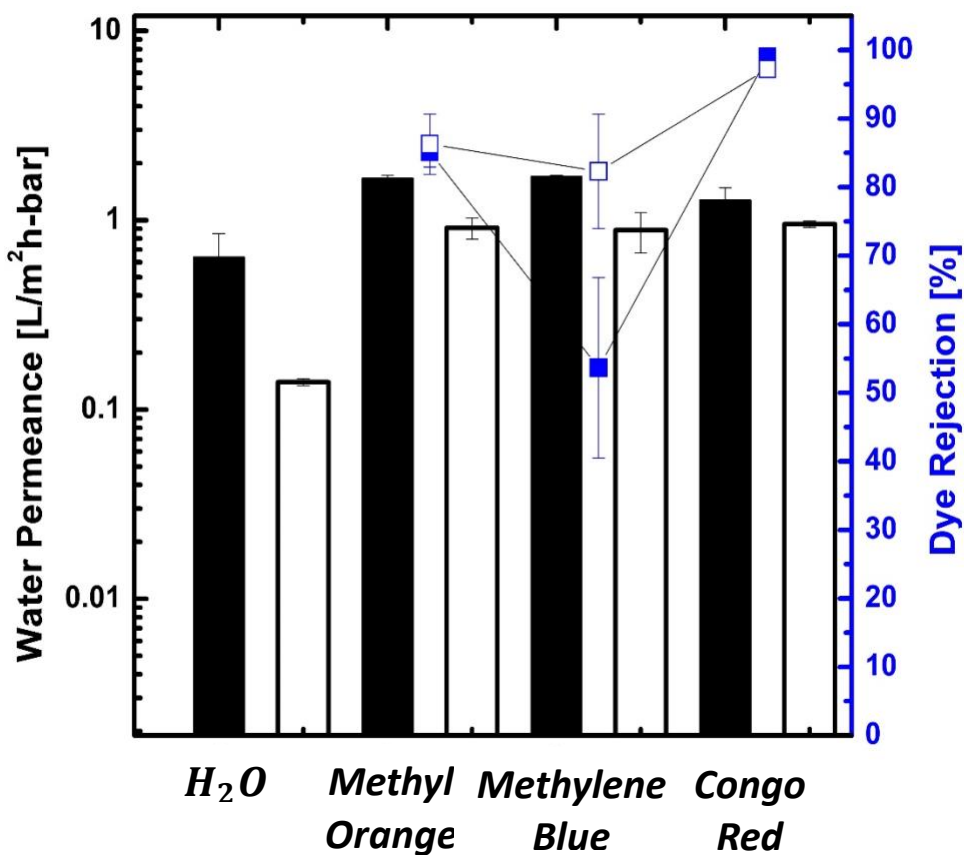


Figure 6: Water permeance (L/m²h – bar) [black bars] and Dye rejection (%) [blue squares] for PA-TFN- 1.12 wt% UiO66-NH₂ [filled symbols] and the baseline PA-TFC membrane without MOF [open symbols]

Figure 6 shows the water permeance for both pure water and all dyes of interest for the highest MOF loading tested (1.12 wt%). These results show that with the addition of MOF to the PA structure high large impurity rejection can be obtained while maintain high water permeance. This suggests that, as was similarly shown for NaCl, solute removal of organic solutes may be able to be tuned while maintaining high water permeance. Figure 6 shows higher rejection values for all dyes tested at 1.12 wt% MOF loading than that of MgSO₄ rejection. This is a reasonable observation as methyl orange (11.84 Å), methylene blue (12.26 Å) and congo red (23.13 Å) all have significantly higher molecular sizes than the reported hydrated diameter of Mg²⁺ (8.6 Å) resulting in better molecular size-based exclusion.^{19,24,29} However, it is interesting to note that the dye rejection does not directly increase with increasing molecular size and in fact drops from methyl orange to methylene blue and subsequently spikes at congo red. The U-shaped dye rejection trend from methyl orange to congo red can mostly likely be attributed to a combined effect of molecular weight driven exclusion and electrostatic interactions with the polyamide surface.

The initial drop from methyl orange to methylene blue can most likely be attributed to the difference in charge between methyl orange (negative) and methylene blue (positive).²⁴ Prior work with ZIF-8 incorporated PA-TFNs have shown that in addition to higher molecular weight, negatively charged dyes tend to have higher rejection due to electrostatic repulsion with the slightly negatively charged polyamide surface.²⁴ In this work, the comparison of methylene blue (373.9 g/mol – negative) and methyl orange (327.3 g/mol – positive), dyes of similar size but

different charge, highlights a similar conclusion as the significant drop in dye rejection [and subsequent jump in solute permeance (Table C1)] suggests that both size-sieving and electrostatic charge effects are important for rejection analysis.^{14,24} The following spike in dye rejection for congo red can thus be attributed to the combined presence of MOF with its distinct 5.9 Å, negative dye charge, and the known aggregation of Congo Red to itself resulting in molecular sizes larger than the reported 23.13 Å, further promoting dye rejection. As the mechanism in which the MOF incorporates into the PA layer is still unknown, it is important to note that the ~50 nm UiO66-NH₂ and known total PA layer thickness of ~ 96 nm suggests complete incorporation of the MOF into the PA layer takes place via the LbL “sandwiched” synthesis procedure. As pressure-driven rejection methods such as this are known to be dependent on procedural characteristics (applied pressure, solution concentration etc.) it useful to have more intrinsic polymer property information, such as water and solute permeance, to elucidate structure/property relationships that can inform future design of these membranes.¹⁸

At 1.12 wt% UiO66-NH₂ loading, little change in water permeance between pure water and the dyes of interest can be observed (Figure 6) over a range of highly varying dye rejections. As trends with water and salt transport as pressure increases have been well studied previously for PA-TFN membranes, it would be reasonable to initially assume the relatively stable water permeance after the introduction of different dyes to solution could be a result of the high pressure applied during testing.⁷ As membranes in this study were tested at 7-10 bar (higher than the typical NF range of 2-6 bar), the formation of voids at the PA/nanoparticle interface at high pressures, shown to previously be responsible for a slight increase in solute water permeance (and therefore a decrease in rejection), could also be responsible for the consistently high water permeances observed.^{7,26} However, the unusually high dye water permeances observed, when

compared to the pure water permeance, rather point to a similar “settling” of the PA structure as observed with the plateauing trend in pure water permeance and MgSO_4 rejection.

It has been shown for normal PA-TFC membranes that though the salt rejection tends to continually increase as the applied pressure increases, the water flux reaches a cap as the applied pressure continues to increase.³⁰ In this case, the addition of the MOF institutes additional water transport channels through distinct pores and the strategic interruption of the polyamide matrix resulting in the higher normalized pure water permeance values reported in Figure 4B. With the water flux cap at high applied pressure in mind, the plateaued pure water permeance (Figure 4B) coupled with stabilized water permeance after the introduction of all dyes, suggests that we may have reached this applied pressure cap as a result of a more settled polyamide matrix at the highest MOF loading. More specifically, the 96% change in solute permeance from smallest (Methyl Orange) to largest (Congo Red) dye compared to the water permeance change, 23%, highlights that the water transport is significantly less dependent on polymer structure than the solute transport.⁵ This means that with a greater impact of polymer structure on solute transport than water transport, we are able to tune the solute transport for the organic pollutant of interest while maintaining high water permeance.

6.2.6. Water/Solute Selectivity

Though the mechanism of the addition of the MOF to the PA layer is not fully understood, the above results imply that at the highest loading tested, a stable PA layer containing UiO66-NH_2 is formed. The stable water permeance coupled with variable solute permeance suggest that a high water permeance can be maintained while providing the opportunity to tune the solute transport. As the water permeance was shown to plateau after 0.4 wt% (Figure 4), this suggests the solute transport can be tuned at or above a MOF loading of 0.4

wt% if dispersion in the PA layer can be maintained. To gain further insight on how the water and dye transport results translate to the efficiency of the NF process in removing these large organic impurities, the water/solute selectivity information is needed.

As described above, dye rejection can depend on both the experimental conditions and the solute characteristics (charge, size, hydrophilicity etc.) so the water/solute permeance-based selectivity is used as a fundamental polymer property-based efficiency metric.^{27,28,30} Similar to A/B selectivity derived for NaCl transport, the dye solution water permeance (A) and dye rejection, obtained experimentally, can be used to determine the solute permeance (B) and thus A/B selectivity for the dyes of interest.^{5,15,22} Figure 7 shows the A/B selectivity with changing water permeance for our baseline LbL-made PA-TFC membrane (open symbols) and the highest MOF loading tested (1.12 wt%) PA-TFN membrane (filled symbols). For the PA-TFN membrane sample, A/B selectivity for increases directly with solute size while remaining within the same order of magnitude for water permeance (Figure 7). Further, the highest A/B selectivity is obtained for our PA-TFN sample for Congo Red (23.13A) suggesting superior removal of large organic impurities when the MOF is present in the PA layer.

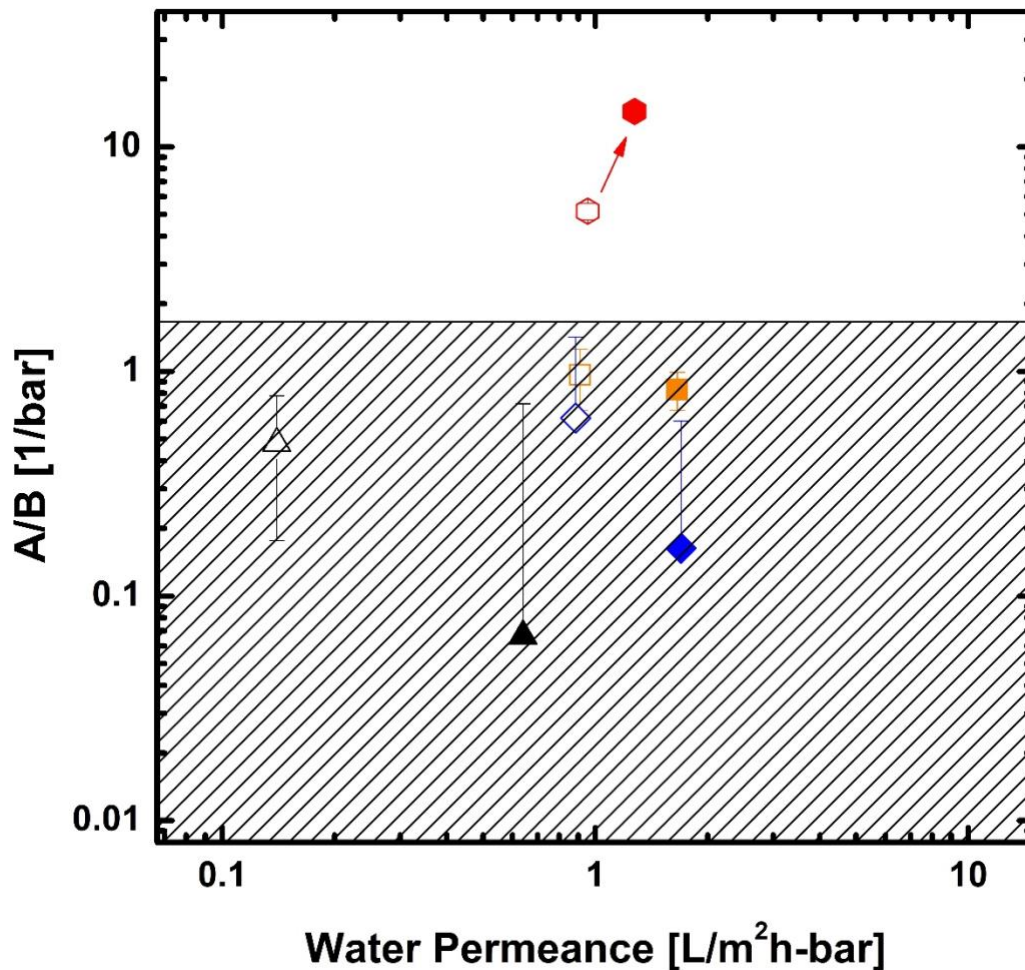


Figure 7: Water/solute selectivity (1/bar) versus water permeance (L/m²h – bar) for PA-TFN-1.12 wt% UiO66-NH₂ [filled symbols] and the baseline PA-TFC membrane without MOF [open symbols] for varying solutes: MgSO₄ [black triangle], methyl orange [orange square], methylene blue [blue diamond], and congo red [red hexagon]. Points above the shaded regime highlight the points where the MOF-containing composite membrane performance surpasses that of the PA-TFC membrane without the MOF.

Water/solute permeance-based selectivity provides an efficiency metric for nanofiltration performance through speaking to the tradeoff between water and solute transport.^{27,30} Further, it allows for direct comparison of water permeance (A) and solute permeance (B) for different membranes as these transport values are normalized to the polymer thickness allowing for easy comparison between different polymer types if their individual trends can be deconvoluted.²⁷ A/B selectivity versus A results shown in Figure 8 highlight the greater percentage change in

A/B selectivity (214%) than water permeance (98%) for all solutes presented suggesting a greater dependence on polymer structure for solute transport than water transport, as observed above. In fact, this gap widens when only the dyes are considered where the A/B percentage change (95%) is approximately three times that of the percentage change in water permeance (31%). These results suggest a greater level of control is accessible for solute transport as the solute of interest increases in molecular size which aligns with NF high retention of solutes from 200 – 1000 g/mol.^{1,6} Further, LbL “sandwiched” synthesis allows for control of MOF loading through both solution concentration and number cycles providing a vehicle in which to control polymer structure and therefore tune to specific large solute transport.

Though useful for continued NF membrane development, water/solute permeance-based selectivity information for solutes other than NaCl is not readily available in literature. However, it is reasonable to predict that for larger solutes, A/B will be lower than the expected $\sim 10^0$ order of magnitude upper-bound for the NF PA-TFC NaCl-based regime as the solubility of many of these organic molecules in synthetic polymers tends to be higher than highly hydrophilic ions resulting in lower sorption selectivity and thus a lower A/B selectivity ($< 10^0$).²⁸ This trend aligns with the observation that both the baseline PA-TFC membrane and the MOF-containing PA-TFN membrane have A/B values below $\sim 10^0$ for all solutes other than congo red (Figure 7). More specifically, for all solutes other than congo red, the A/B selectivity for the MOF-containing sample was lower than that of the baseline PA-TFC membrane.

However, congo red A/B selectivity data shows a higher A/B selectivity for the MOF-containing PA-TFN when compared to the baseline LbL-made PA-TFC membrane. This suggests that not only does the dominance of the increased interaction between the dye and the polymer reduce for congo red, but that with the addition of the MOF, superior A/B selectivity can

be obtained. Since the solute permeance has been shown to change ~3 times more over the range of dye solutes tested, than the water permeance, for our PA-TFN membrane, this suggests that the presence of the MOF enhances the composite membranes' ability to restrict large solute permeance, like congo red. Further, the presence of the MOF results in a 95% drop in dye permeance (*B*) from methyl orange to congo red over only a 23% change in water permeance which suggests that UiO66-NH₂ has been well embedded into the polyamide matrix and at 1.12 wt% consistent distribution of the MOF within the PA layer has taken place. These results mirror the previously observed plateau trend observed for pure water permeance and MgSO₄ rejection suggesting a similar “settling” of the PA structure at or above 0.4 wt% MOF loading. This successful formation of a dense polyamide with UiO66-NH₂ allows for both the size-sieving nature of the MOF and the high water/solute selectivity of the polyamide to be leveraged for highly efficient removal of large organic pollutants via NF.

Overall, the above results imply that the addition of UiO66-NH₂ to the composite structure, allows for high water permeance to be maintained while increasing the efficiency of solute removal as solute size increases. The flip in the A/B selectivity trend between the baseline PA-TFC membrane and the MOF-incorporated PA-TFN membrane for congo red further suggests that at higher MOF loading, LbL “sandwiched”-made PA-TFN membranes can maintain relatively little change in water permeance while providing the opportunity to tune solute transport for very large organic pollutants. As this synthesis technique ensures full embedding of the MOF into the PA layer through a sequential spin-coater based process, it is necessary to both assess the contribution of the addition of the MOF to the specific PA layer performance as well as ensure the performance of the composite membrane discussed above is majorly due to the altered PA layer through a PVA primer layer contribution analysis. Through

setting a 5% resistance-to-mass-transfer cap on the allotted contribution of the PVA primer layer, a similar resistance-in-series model as discussed elsewhere can be applied to determine where the PVA primer layer's percentage contribution to overall mass transfer resistance falls for all MOF loadings and solutes of interest.

6.3.5. Application of Resistance in Series Model and PVA Primer Layer Contribution to Mass Transfer of Water

To ascertain the majority contribution of the PA layer to the overall resistance to mass transfer for water, a resistance-in-series model was applied to our 1.12 wt% UiO66-NH₂ PA-TFN membrane system to determine the individual PA layer water transport performance (Section C3).^{15,23} This information was then compared to the previously discussed water permeance data for the composite membrane (Figure C2 and C3) to determine if the experimentally determined water permeance accurately represents the performance of the PA layer (i.e. is $A_{PA-TFN} \approx A_{PA}$). Finally, a comparison of the PA layer specific resistance to mass transfer (A_{PA}^{-1}) and the composite membrane resistance to mass transfer (A_{PA-TFN}^{-1}) was used to determine the percentage contribution of the PVA primer layer to the overall mass transfer resistance (Figure C4). A previously set cap of 5% PVA primer layer contribution (i.e. $\frac{A_{PA}^{-1}}{A_{PA-TFN}^{-1}} \leq 5\%$) was used to determine if the PA layer dominates the resistance to mass transfer for the solutes of interest (MgSO₄, Methyl Orange, Methylene Blue, and Congo Red).¹⁵ It is important to note that the data for the highest MOF loading was chosen as it is expected that agreement between individual PA layer and composite membrane values using a resistance-in-series model will be more likely at lower MOF loadings due to their proximity in water permeance performance to the baseline LbL made PA-TFC membrane. This means that if high agreement

can be achieved at high MOF loadings the trends discussed below will persist at lower MOF loadings.

Figure C2 shows good agreement between the experimentally-obtained PA-TFN membrane water permeance results and the calculated individual PA layer water permeance. Figure C3 shows similar agreement between the composite and individual layer water permeance values when extended to the dye solutions. These results suggest that at a known PA layer thickness of ~96 nm and a maximum additional thickness of 50 nm from the MOF (assuming incomplete embedding into the PA layer), the experimentally obtained water permeance for the composite can provide preliminary information about the PA layer itself, as was similarly observed in previous work with our baseline LbL-made PA-TFC membrane. [30] However, even though all calculated PA layer values (A_{PA}) fall into the standard deviation of the experimentally obtained composite membrane values (A_{PA-TFN}), the higher water permeance observed for the MOF-incorporated PA layers when compared to the baseline LbL-made PA suggests a reduction in its contribution to the overall mass transfer resistance. More specifically, as the same ~288 nm thick PVA primer layer is instituted, the increase in water permeance (and therefore decrease in resistance to mass transfer for water) observed for the MOF-containing PA layers would suggest a larger percentage contribution to the overall resistance to mass transfer by the PVA primer layer than previously reported.

When employing a primed porous support, its contribution to overall mass transfer resistance is often not completely insignificant relative to the active layer.²⁸ By determining the mass transfer contribution of the PVA layer to the overall mass transfer resistance to water, we can observe how it changes with both our polymer structure (through MOF loading) and our solute of interest.¹⁵ Figure C4 shows the PVA layer percentage contribution for varying solutes

of interest as MOF loading is increased. These results show a PVA layer percentage contribution to mass transfer for water less than 5% for all points suggesting that the PA layer maintains a majority mass transfer resistance contribution within this range of MOF loadings. In fact, spanning the order of magnitude change in MOF loading and solute size, a PVA layer percentage contribution of at or below 3% is obtained suggesting that there is a lot of room for structure tuning within a regime that still maintains a majority mass transfer resistance contribution of the PA layer.

More specifically, the PVA layer percentage contribution increases with both solute size and MOF loading. The direct relationship between PVA layer percentage contribution and MOF loading can be tied directly to the increasing water permeance with MOF loading observed in Figure 4. As the composite water permeance (A_{PA-TFN}) increases, the resistance to mass transfer for water (A_{PA-TFN}^{-1}) decreases suggesting that the same resistance to mass transfer for the PVA layer (A_0^{-1}) would thus represent a larger percentage of the overall mass transfer resistance for the PA-TFN membrane than the baseline LbL-made PA-TFC membrane. On the contrary, the increase in PVA layer percentage contribution for water with increase solute size cannot be tied directly to experimentally obtained values and is instead a result of the greater change in solute permeance than water permeance over the MOF loadings tested.

Preliminarily, an increase in the contribution to resistance to mass transfer by the PVA layer with solute size can be predicted through the experimentally obtained congo red rejection comparison of the PVA-primed support (93%) and the 1.12 wt% PA-TFN membrane (99%). The close dye rejections of the primed support and the composite membrane suggest that the PVA layer has a similar ability to reject congo red as the PA layer itself, as we have shown we are able to reasonably equate the performance of the composite membrane with the individual MOF-

incorporated PA layer. However, the $\sim 10^2$ magnitude difference in the calculated intrinsic congo red permeance for the PVA primed support ($B = 3.21 \times 10^{-4} \text{ cm/s}$) and the composite membrane ($B = 2.48 \times 10^{-6} \text{ cm/s}$), approximately equal to that of the MOF-incorporated PA layer, shown in Table S1, more readily yields to the $\sim 3\%$ contribution of the PVA layer to the overall mass transfer resistance to water. This further emphasizes the value of intrinsic membrane values, specifically for PA layer, to elucidate structure/property relationships needed to tune for more efficient desalination processes.

The agreement between the calculated PA layer and experimentally obtained PA-TFN composite membrane water permeance implies that the resistance-in-series model, reported previously for LbL-made PA-TFC membranes can similar be applied for membranes made via LbL “sandwiched” synthesis for UiO66-NH₂ incorporation. Further, though higher water permeance values for the PA-TFN membranes tested reasonably results in a reductio in mass transfer resistance to water, the PVA layer contribution to mass transfer resistance remains at or below 3% suggesting a majority contribution by the MOF-incorporated PA layer is maintained. When expanding studies to higher MOF loadings and larger solutes, the change in calculated solute permeance (B) between the PVA primed support and the composite membrane will need to be considered as this has been shown to more closely tie to the change in PVA layer percentage contribution than the experimentally obtained dye rejection.

6.3. Conclusion

Through an LbL “sandwiched” synthesis of the selective PA layer, a PA-TFN membrane containing varying loadings of UiO66-NH₂ was successfully formed. With a known PA layer thickness and full encapsulation of the UiO66-NH₂ during synthesis, we were able to not only gain insight about the composite membrane performance as it compares to key baseline

membranes, but similarly obtain PA layer specific transport data and assess the relative contributions to mass transfer resistance of each layer as reported previously. More specifically, the water/solute selectivity trends discussed above suggest the ability to shift the previously studied RO-designed PA layer to the NF performance regime by improving water transport and increasing congo red rejection. The controlled growth of the PA layer coupled with the intentional “sandwiching” of the MOF particles provides an avenue for expansion of this process to both other similarly sized MOFs as well as the introduction of additional PA binder layers of known thickness to tune water and solute transport.

6.4. References

- (1) Wu, X.; Yang, L.; Meng, F.; Shao, W.; Liu, X.; Li, M. ZIF-8-Incorporated Thin-Film Nanocomposite (TFN) Nanofiltration Membranes: Importance of Particle Deposition Methods on Structure and Performance. *J. Memb. Sci.* **2021**, *632*, 119356. <https://doi.org/10.1016/j.memsci.2021.119356>.
- (2) Wang, L.; Fang, M.; Liu, J.; He, J.; Deng, L.; Li, J.; Lei, J. The Influence of Dispersed Phases on Polyamide/ZIF-8 Nanofiltration Membranes for Dye Removal from Water. *RSC Adv.* **2015**, *5* (63), 50942–50954. <https://doi.org/10.1039/C5RA06185G>.
- (3) Gong, Y.; Gao, S.; Tian, Y.; Zhu, Y.; Fang, W.; Wang, Z.; Jin, J. Thin-Film Nanocomposite Nanofiltration Membrane with an Ultrathin Polyamide/UiO-66-NH₂ Active Layer for High-Performance Desalination. *J. Memb. Sci.* **2020**. <https://doi.org/10.1016/j.memsci.2020.117874>.
- (4) Liu, H.; Zhang, M.; Zhao, H.; Jiang, Y.; Liu, G.; Gao, J. Enhanced Dispersibility of Metal–Organic Frameworks (MOFs) in the Organic Phase via Surface Modification for TFN Nanofiltration Membrane Preparation. *RSC Adv.* **2020**, *10* (7), 4045–4057. <https://doi.org/10.1039/C9RA09672H>.
- (5) Fang, S. Y.; Zhang, P.; Gong, J. L.; Tang, L.; Zeng, G. M.; Song, B.; Cao, W. C.; Li, J.; Ye, J. Construction of Highly Water-Stable Metal–Organic Framework UiO-66 Thin-Film Composite Membrane for Dyes and Antibiotics Separation. *Chem. Eng. J.* **2020**, *385*, 123400. <https://doi.org/10.1016/j.cej.2019.123400>.
- (6) Zhang, H.; Bin Li; Pan, J.; Qi, Y.; Shen, J.; Gao, C.; Van der Bruggen, B. Carboxyl-Functionalized Graphene Oxide Polyamide Nanofiltration Membrane for Desalination of Dye Solutions Containing Monovalent Salt. *J. Memb. Sci.* **2017**, *539*, 128–137. <https://doi.org/10.1016/j.memsci.2017.05.075>.
- (7) Zhang, X.; Zhang, Y.; Wang, T.; Fan, Z.; Zhang, G. A Thin Film Nanocomposite Membrane with Pre-Immobilized UiO-66-NH₂ toward Enhanced Nanofiltration Performance. *RSC Adv.* **2019**, *9* (43), 24802–24810. <https://doi.org/10.1039/C9RA04714J>.
- (8) Zhao, D. L.; Yeung, W. S.; Zhao, Q.; Chung, T. S. Thin-Film Nanocomposite Membranes Incorporated with UiO-66-NH₂ Nanoparticles for Brackish Water and Seawater

- Desalination. *J. Memb. Sci.* **2020**. <https://doi.org/10.1016/j.memsci.2020.118039>.
- (9) Ni, L.; Liao, Z.; Chen, K.; Xie, J.; Li, Q.; Qi, J.; Sun, X.; Wang, L.; Li, J. Defect-Engineered UiO-66-NH₂modified Thin Film Nanocomposite Membrane with Enhanced Nanofiltration Performance. *Chem. Commun.* **2020**. <https://doi.org/10.1039/d0cc01556c>.
- (10) Zhu, J.; Hou, J.; Yuan, S.; Zhao, Y.; Li, Y.; Zhang, R.; Tian, M.; Li, J.; Wang, J.; der Bruggen, B. MOF-Positioned Polyamide Membranes with a Fishnet-like Structure for Elevated Nanofiltration Performance. *J. Mater. Chem. A* **2019**, *7* (27), 16313–16322. <https://doi.org/10.1039/C9TA02299F>.
- (11) Lv, Z.; Hu, J.; Zhang, X.; Wang, L. Enhanced Surface Hydrophilicity of Thin-Film Composite Membranes for Nanofiltration: An Experimental and DFT Study. *Phys. Chem. Chem. Phys.* **2015**, *17* (37), 24201–24209. <https://doi.org/10.1039/C5CP04105H>.
- (12) Aghili, F.; Ghoreyshi, A. A.; Van der Bruggen, B.; Rahimpour, A. Introducing Gel-Based UiO-66-NH₂ into Polyamide Matrix for Preparation of New Super Hydrophilic Membrane with Superior Performance in Dyeing Wastewater Treatment. *J. Environ. Chem. Eng.* **2021**, *9* (4), 105484. <https://doi.org/https://doi.org/10.1016/j.jece.2021.105484>.
- (13) Al-Shaeli, M.; Smith, S. J. D.; Jiang, S.; Wang, H.; Zhang, K.; Ladewig, B. P. Long-Term Stable Metal Organic Framework (MOF) Based Mixed Matrix Membranes for Ultrafiltration. *J. Memb. Sci.* **2021**, *635*, 119339. <https://doi.org/https://doi.org/10.1016/j.memsci.2021.119339>.
- (14) Aghili, F.; Ghoreyshi, A. A.; Van der Bruggen, B.; Rahimpour, A. A Highly Permeable UiO-66-NH₂/Polyethyleneimine Thin-Film Nanocomposite Membrane for Recovery of Valuable Metal Ions from Brackish Water. *Process Saf. Environ. Prot.* **2021**, *151*, 244–256. <https://doi.org/https://doi.org/10.1016/j.psep.2021.05.022>.
- (15) Agata, W.-A. S.; Thompson, J.; Geise, G. M. Layer-by-Layer Approach to Enable Polyamide Formation on Microporous Supports for Thin-Film Composite Membranes. *J. Appl. Polym. Sci.* *n/a* (n/a), 51201. <https://doi.org/https://doi.org/10.1002/app.51201>.
- (16) Huelsenbeck, L.; Luo, H.; Verma, P.; Dane, J.; Ho, R.; Beyer, E.; Hall, H.; Geise, G. M.; Giri, G. Generalized Approach for Rapid Aqueous MOF Synthesis by Controlling Solution PH. *Cryst. Growth Des.* **2020**, *20* (10), 6787–6795. <https://doi.org/10.1021/acs.cgd.0c00895>.
- (17) Luo, H.; Cheng, F.; Huelsenbeck, L.; Smith, N. Comparison between Conventional Solvothermal and Aqueous Solution-Based Production of UiO-66-NH₂: Life Cycle Assessment, Techno-Economic Assessment, and Implications for CO₂capture and Storage. *J. Environ. Chem. Eng.* **2021**, *9* (2), 105159. <https://doi.org/10.1016/j.jece.2021.105159>.
- (18) Geise, G. M. Why Polyamide Reverse-Osmosis Membranes Work so Well. *Science* (80-.). **2021**. <https://doi.org/10.1126/science.abe9741>.
- (19) Wang, L.; Fang, M.; Liu, J.; He, J.; Li, J.; Lei, J. Layer-by-Layer Fabrication of High-Performance Polyamide/ZIF-8 Nanocomposite Membrane for Nanofiltration Applications. *ACS Appl. Mater. Interfaces* **2015**, *7* (43), 24082–24093. <https://doi.org/10.1021/acsami.5b07128>.
- (20) Geise, G. M.; Park, H. B.; Sagle, A. C.; Freeman, B. D.; McGrath, J. E. Water Permeability and Water/Salt Selectivity Tradeoff in Polymers for Desalination. *J. Memb. Sci.* **2011**, *369* (1–2), 130–138. <https://doi.org/10.1016/j.memsci.2010.11.054>.
- (21) Choi, W.; Gu, J. E.; Park, S. H.; Kim, S.; Bang, J.; Baek, K. Y.; Park, B.; Lee, J. S.; Chan,

- E. P.; Lee, J. H. Tailor-Made Polyamide Membranes for Water Desalination. *ACS Nano* **2015**, *9* (1), 345–355. <https://doi.org/10.1021/nn505318v>.
- (22) Gu, J. E.; Lee, S.; Stafford, C. M.; Lee, J. S.; Choi, W.; Kim, B. Y.; Baek, K. Y.; Chan, E. P.; Chung, J. Y.; Bang, J.; Lee, J. H. Molecular Layer-by-Layer Assembled Thin-Film Composite Membranes for Water Desalination. *Adv. Mater.* **2013**, *25* (34), 4778–4782. <https://doi.org/10.1002/adma.201302030>.
- (23) Yang, Z.; Guo, H.; Tang, C. Y. The Upper Bound of Thin-Film Composite (TFC) Polyamide Membranes for Desalination. *J. Memb. Sci.* **2019**. <https://doi.org/10.1016/j.memsci.2019.117297>.
- (24) Zhang, H.; Geise, G. M. Modeling the Water Permeability and Water/Salt Selectivity Tradeoff in Polymer Membranes. *J. Memb. Sci.* **2016**, *520*, 790–800. <https://doi.org/10.1016/j.memsci.2016.08.035>.
- (25) Chowdhury, M. R.; Steffes, J.; Huey, B. D.; McCutcheon, J. R. 3D Printed Polyamide Membranes for Desalination. *Science (80-.)*. **2018**, *361* (6403), 682–686. <https://doi.org/10.1126/science.aar2122>.
- (26) Jian, S.; Xiao Ming, S. Crosslinked PVA-PS Thin-Film Composite Membrane for Reverse Osmosis. *Desalination* **1987**, *62* (C), 395–403. [https://doi.org/10.1016/0011-9164\(87\)87040-6](https://doi.org/10.1016/0011-9164(87)87040-6).
- (27) Liu, Y.; Zhang, S.; Zhou, Z.; Ren, J.; Geng, Z.; Luan, J.; Wang, G. Novel Sulfonated Thin-Film Composite Nanofiltration Membranes with Improved Water Flux for Treatment of Dye Solutions. *J. Memb. Sci.* **2012**, *394–395*, 218–229. <https://doi.org/10.1016/j.memsci.2011.12.045>.
- (28) Luo, H.; Agata, W.-A. S.; Geise, G. M. Connecting the Ion Separation Factor to the Sorption and Diffusion Selectivity of Ion Exchange Membranes. *Ind. Eng. Chem. Res.* **2020**. <https://doi.org/10.1021/acs.iecr.0c02457>.
- (29) Xia, L.; Ren, J.; Weyd, M.; McCutcheon, J. R. Ceramic-Supported Thin Film Composite Membrane for Organic Solvent Nanofiltration. *J. Memb. Sci.* **2018**, *563*, 857–863. <https://doi.org/10.1016/j.memsci.2018.05.069>.
- (30) Geise, G. M.; Paul, D. R.; Freeman, B. D. Fundamental Water and Salt Transport Properties of Polymeric Materials. *Progress in Polymer Science*. 2014, pp 1–42. <https://doi.org/10.1016/j.progpolymsci.2013.07.001>.

Chapter 7: Conclusions and Recommendations

This dissertation has provided knowledge on the application of a layer-by-layer sequential deposition synthesis for polyamide thin film composite membranes. The verification of this procedure for both MPD/TMC-based and UiO66-NH₂-containing PA layers has been confirmed using key water and solute transport metrics for RO-driven and NF-driven applications, respectively. Further, a resistance in series model has been applied to assess the individual composite layer contributions to mass transfer resistance and thus provide unique insight on the specific effects of altered PA layer synthesis on the intrinsic PA layer performance. This chapter summarizes the results of Chapters 5 and 6 and provides recommendations for future research.

7.1. Conclusions

In Chapter 5, the application of layer-by-layer sequential deposition of MPD/TMC-based polyamides was assessed via synthesis onto a PVA primed support. The formation of a smooth polyamide layer of known thickness was confirmed by determining the polyamide growth rate with cycle number (3.2 nm/cycle) and confirming a comparable surface roughness can be obtained after the replacement of the final wash solvent with methanol. Water and NaCl transport tests on composite membranes made with and without the PVA primer layer showed that the presence of the PVA primer ensures a defect free PA layer is synthesized while protecting the porous support from organic solvent degradation. Further, comparable water permeance and salt rejection to a commercial RO PA-TFC membrane standard can be obtained after 30 cycles on the PVA-primed support. Analysis of these composite membranes was extended using a series resistance model to assess the contribution of PA layers to the overall resistance to mass transfer for water and NaCl. A deviation of less than 5% between the

composite membrane and PA layer specific water and salt permeance showed that not only does the PA layer maintain a majority contribution to mass transfer resistance after 30 cycles on the PVA-primed support but the PVA primer layer does not incur significant mass transfer resistance to the system. Finally, successful application of LbL synthesis to the addition of co-monomers was confirmed through an order of magnitude drop in ionic resistance (i.e. increase in ionic conductivity) of sulfonated PA layer deposited on a commercial CEM.

In Chapter 6, the extension of the LbL sequential deposition process to incorporate MOFs was assessed via a “sandwiched” synthesis of the PA layer with UiO66-NH₂. The synthesis of a PA layer containing UiO66-NH₂ was confirmed using TGA scans, spanning from room temperature to 1000C, to obtain the intrinsic membrane MOF loading in wt% and relate it to the experimentally used MOF solution concentration (mg/mL). Water transport tests of these LbL “sandwiched” -made PA-TFNs further confirmed the presence of MOF in the composite membrane up to ~10 times the water permeance was obtained with increasing MOF loading as a result of the fixed pores and resultant open polyamide pore structure attributed to the addition of UiO66-NH₂ to the PA layer. Comparable MgSO₄ rejection to a commercial NF PA-TFC membrane and water/NaCl selectivity data show that all MOF-incorporated samples fall into the NF regime suggested the ability to shift an RO PA layer to an NF one. Though the mechanism in which the MOF incorporates into the PA layer is still unknown, complete encapsulation of the nanoparticles this synthesis method aims toward through the “sandwiching” of small MOF between PA layers of known thickness, is further confirmed through the log-shaped trend of both pure water permeance and water permeance in dye solutions. More specifically, little change in water permeance of dye solutions coupled with higher dye rejection than salt rejection suggests an ability to tune the solute transport via MOF loading without sacrificing the improved water

permeance. This is further confirmed through water/solute selectivity data at the highest loading where the highest selectivity was obtained for the congo red, the largest solute while little change water permeance was observed over the solutes tested. Finally, an application of the series resistance model yielded a less than 3% contribution to mass transfer by the PVA layer for all solutes tested suggesting that, similar to the baseline LbL-made PA-TFC membrane, experimentally obtained composite membrane transport data can reasonably predict the individual PA layer performance.

7.2. Significance

In addition to the extension of synthesis of LbL-made PA layers onto PVA-primed supports through characterization and preliminary water and salt transport tests, our study in Chapter 5 addressed the knowledge gap of the effect of the primer layer on the performance and overall resistance to mass transfer of the composite membrane. Further, it confirmed the ability to expand this technique for the addition of fixed charge groups to the PA layer, for the first time, highlighting the opportunities LbL offers for both expanded PA layer synthesis and the development of PA layer specific structure/property relationships. The expansion of this sequential deposition process from PA-TFC membrane formation to PA-TFN membrane formation, discussed in Chapter 6, addressed the typical PA-TFN drawback of MOF leaching after synthesis through “sandwiching” an allotted amount of UiO66-NH₂ between PA layers of known thickness. In addition to being able to obtain water and solute transport performance comparable to NF standards, this work employed a resistance in series-based analysis to show that through growing the modified PA layer in this way, we can directly compare the PA layer specific water and solute permeance for samples with or without the MOF. By addressing the knowledge gaps highlighted in Chapter 2 through this dissertation, we have allowed for more PA

layer specific structure/property relationships to be drawn for both typically studied MPD/TMC-based PA layers as well as modified (i.e. fixed charge groups and nanofillers) PA layers allowing for more informed membrane design.

7.3. Recommendations for Future Work

7.3.1. Expansion of Sulfonated PA-TFC Study to Sulfonated Monomers with Greater Distance from Benzene Ring

The research in Chapter 5 set the state for the application of LbL synthesis for sulfonated PA layers made for a functionalized MPD-based monomer.¹ However, there is an opportunity to gain greater control of the ionic conductivity of the sulfonated PA layer not only through changing monomer concentration but through changing the monomer structure and in turn reactivity of the monomer. Prior work by Nsegiumva et al. showed that for polyester-based polymers, the yield of charge group incorporation increases with the distance between the charged monomer functional group from the aromatic ring due to a shift in its steric nature.² An extension of the proof-of-concept study on sulfonated MPD (i.e. MPDSK) can be done through an evaluation of sulfonated PA layers made with similarly oriented monomers with differing distance between the MPD-benzene ring and the sulfonate group. The prior work with the functionalization of polyester-based polymers suggests that the ability to add sulfonate groups at the same monomer concentration and reaction time will change with the distance between the sulfonated group and the benzene. The application of LbL synthesis for these varied sulfonated PA layers will provide a unique opportunity to obtain PA layer specific structure/property relationships geared towards electro dialysis applications.³

7.3.2. Development of Counter-ion/Counter-ion Selectivity in Mixed Electrolytes for Expansion to Electro dialysis

Counter-ion/Counter-ion selectivity is an important metric for electro dialysis as, similar to water/solute selectivity for pressure-driven desalination, it acts as a performance efficiency metric for electrically-driven desalination techniques.^{4,5} However, to perform this electrically-driven measurement for PA-TFC membranes, a large current density would need to be applied to overcome the relatively low degree of sulfonation currently accessible using IP-based synthesis. The research in chapter 5 shows successful sulfonation of the PA layer via LbL and through the extension of this work to varied sulfonated monomers and monomer concentrations, access to higher degree of sulfonation could be possible with the removal of the oil-water reaction interface of IP. In addition, the ion flux-based counter-ion/counter-ion selectivity can be obtained for the PA layer specifically through the application of a mixed electrolyte three-chamber microfluidic system as has been previously reported.⁵ This work would allow us to extend the structure/property relationships we have previously derived for the sulfonated PA layer to a direct metric of electro dialysis efficiency.

7.3.3. Expansion of MOF-incorporated PA-TFN to tuning Solute/Solute Selectivity Procedure

The research in Chapter 6 sets the stage for the application of LbL synthesis for the incorporation of MOFs into the PA layer. As this work is the first effort in applying this type of “sandwiching” sequential deposition to the incorporation of MOF into the PA layer, there is an opportunity to further tune the synthesis to assess the prior conclusion that high solute transport tunability is accessible. Through the incorporation of additional MOF cycles alone or possibly PA buffer layers between additional MOF cycles, work can be done to evaluate the A/B selectivity for a greater range of MOF loadings and solutes of interest to pressure test the previous observation of consistently high water permeance with greater change in solute permeance. Further, this data can then be extended to compare solute/solute selectivity (B_1/B_2) to

more specifically interrogate the structure/property relationships driving the ability to control solute transport for NF applications.

7.4. References

- (1) Agata, W.-A. S.; Thompson, J.; Geise, G. M. Layer-by-Layer Approach to Enable Polyamide Formation on Microporous Supports for Thin-Film Composite Membranes. *J. Appl. Polym. Sci.* *n/a* (n/a), 51201. <https://doi.org/https://doi.org/10.1002/app.51201>.
- (2) Nsengiyumva, O.; Miller, S. A. Synthesis, Characterization, and Water-Degradation of Biorenewable Polyesters Derived from Natural Camphoric Acid. *Green Chem.* **2019**. <https://doi.org/10.1039/c8gc03990a>.
- (3) Yang, L.; Tang, C.; Ahmad, M.; Yaroshchuk, A.; Bruening, M. L. High Selectivities among Monovalent Cations in Dialysis through Cation-Exchange Membranes Coated with Polyelectrolyte Multilayers. *ACS Appl. Mater. Interfaces* **2018**, *10* (50), 44134–44143. <https://doi.org/10.1021/acsami.8b16434>.
- (4) Ji, Y.; Geise, G. M. The Role of Experimental Factors in Membrane Permselectivity Measurements. *Ind. Eng. Chem. Res.* **2017**, *56* (26), 7559–7566. <https://doi.org/10.1021/acs.iecr.7b01512>.
- (5) Vardner, J. T.; Ling, T.; Russell, S. T.; Perakis, A. M.; He, Y.; Brady, N. W.; Kumar, S. K.; West, A. C. Method of Measuring Salt Transference Numbers in Ion-Selective Membranes. *J. Electrochem. Soc.* **2017**. <https://doi.org/10.1149/2.0321713jes>.

Appendix A: List of Symbols

Table A.1. Nomenclature

PA-TFC	Polyamide thin-film composite membrane
LbL	Layer-by-layer
PVA	Poly-vinyl alcohol
RO	Reverse osmosis
MOF	Metal organic framework
PA	Polyamide
MPD	M-phenylenediamine
NF	Nanofiltration
TMC	Trimesoyl chloride
IP	Interfacial polymerization
IEM	Ion exchange membrane
CEM	Cation exchange membrane
AEM	Anion exchange membrane
PIP	Piperazine
PA-TFN	Polyamide thin-film nanocomposite membrane
$J_{w,0}$	Water flux for the PVA-primed support
A_0	Water permeance for the PVA-primed support
A_0^{-1}	Resistance to mass transfer for water for the PVA-primed support
$J_{w,x}$	Water flux for the PA layer
A_x	Water permeance for the PA layer
A_x^{-1}	Resistance to mass transfer for water for the PA layer
J_w	Water flux for the composite layer
$A_{overall}^{-1}$	Water permeance for the composite membrane
\bar{V}_w	Partial molar volume of water
R_g	Ideal gas constant
T	Absolute temperature
h_i	Layer thickness
$P_{w,i}$	Effective water permeability of the layer
$B_{overall}$	Salt permeance for the composite membrane
B_0^{-1}	Resistance to mass transfer for salt for the PVA-primed support
B_x^{-1}	Resistance to mass transfer for salt for the PA layer
R_0	Salt rejection of the PVA-primed support
$R_{s,x}$	Salt rejection of the PA layer
R_s	Salt rejection of the composite membrane
$P_{s,i}$	Effective salt permeability of the layer
PES	Polyethersulfone
MPDSA	2,4-diaminobenzenesulfonic acid
MPDSK	potassium 2,4-diaminobenzenesulfonate
THF	Tetrahydrofuran
R_{dye}	Dye rejection

$C_{f,dye}$	Final dye concentration
$C_{i,dye}$	Initial dye concentration
B_{dye}	Dye permeance
LbLx	PA layer made via LbL with x cycles

Appendix B: Supporting Information for Chapter 5

B.1. Discussion of Methanol and Acetone as Final Rinse Solvents

The rinse solvents used in the LbL deposition process influence film growth by removing excess unreacted monomer at the end of each cycle,¹ and removal of excess MPD from the surface is key to obtaining a consistent PA thickness.²⁻⁵ The final rinse solvent is primarily responsible for removing excess unreacted MPD at the end of each deposition cycle. Critical considerations for choosing a rinse solvent are solubility/miscibility and volatility properties, and these considerations are even more important when performing the LbL process on a microporous support because it can dictate the quality of the PA layer formed atop the support.¹ The volatility of the rinse solvent must be balanced: sufficiently volatile to allow excess rinse solvent to evaporate from the surface after the spin-drying step but not so volatile that the rinse solvent evaporates before removing unreacted monomers from the surface.

Acetone has been used as a suitable final rinse solvent previously.^{1,5,6} In our LbL process, using acetone as the final rinse solvent could dissolve the PES microporous support. Chan et al. found that methanol could be used as the final rinse solvent to produce PA membranes that were comparable, in terms of consistent growth rate and minimal roughness, to those membranes prepared using acetone as the final rinse solvent.¹ Methanol is expected to be significantly less detrimental to the PES microporous support, so we used methanol as the final rinse solvent in this study.

One potential disadvantage to using methanol as the final rinse solvent is that methanol may not be as good of a solvent for toluene compared to acetone. The difference in the solubility parameters of methanol and toluene (approximately 10 mPa) is larger than that of acetone and toluene (approximately 1 mPa). Therefore, using methanol as the final rinse solvent (to protect the

PES microporous support) may be less effective, compared to acetone, at removing unreacted monomers from the surface at the end of each cycle.

Other sequential PA formation techniques such as dip coating and spray coating correlate low surface roughness with thickness control.^{7,8} As such, low surface roughness can be an indicator of good removal of excess MPD, as the ridge-and-valley surface structure and resultant high surface roughness of IP-made PA layers is typically attributed to greater excess MPD remaining on the surface.⁹ To investigate further the influence of the final rinse solvent on surface roughness, AFM was used to characterize the surface roughness of a control PVA layer (coated on a glass slide) and PA layers formed using 30 LbL cycles (LbL₃₀) on a PVA coated glass slide and either methanol or acetone as the final rinse solvent. The micrographs and surface roughness values are reported as Figure B1 and Table B1, respectively.

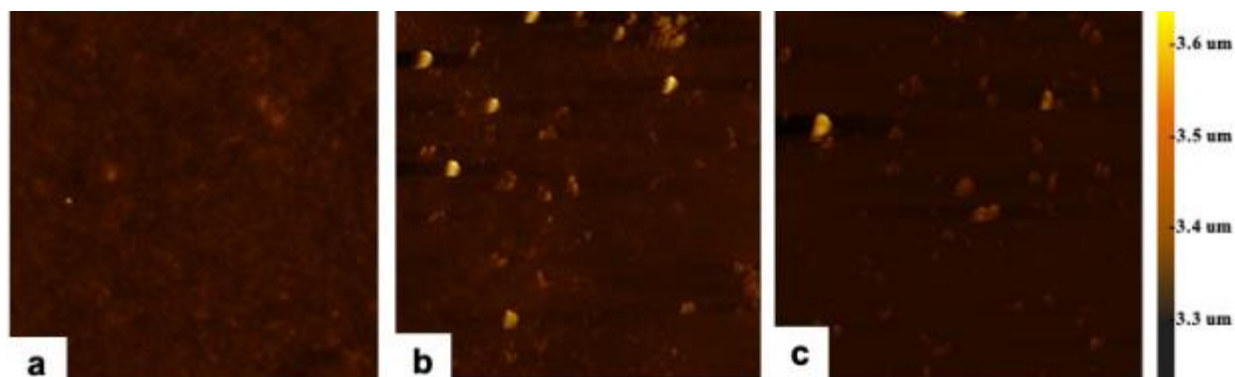


Figure B.1.: AFM images (10 μm x 10 μm area) of a PVA coated glass slide (a), a LbL₃₀ PA layer deposited, on a PVA coated glass slide, using acetone as the final wash solvent (b), and a LbL₃₀ PA layer deposited, on a PVA coated glass slide, using methanol as the final wash solvent (c).

Table B.1.: Surface roughness data, obtained via AFM, for the samples reported in Figure S1. The LbL₃₀ PA layers were formed on a PVA coated glass slide.

Sample	RMS Roughness [nm]
PVA coated glass slide	0.91 ± 0.25
LbL ₃₀ (acetone as final rinse solvent)	17 ± 1
LbL ₃₀ (methanol as final rinse solvent)	9.5 ± 0.8

The RMS roughness values, determined using the analysis software, indicate that lower surface roughness of LbL₃₀ was achieved by using methanol as the final rinse solvent compared to that when acetone was used (Table B1). Low LbL PA layer surface roughness, afforded by the methanol final rinse solvent, partnered with predictable PA layer growth (Figure 2 in the Chapter 5) suggests comparable removal of excess unreacted MPD by both final rinse solvents. This result is consistent with the prior reports suggesting that methanol and acetone are comparable final rinse solvents.¹

B.2. Data Summary

Water and salt transport data are summarized in Table B2. Water permeance, *A*, and salt rejection, *R*, data were measured as described in Chapter 4. Salt permeance, *B*, data were calculated from the measured *A* and *R* data using Equation 3 in Chapter 5.

Table B2: Water and salt transport data summary.

	PVA-Primed Support	LbL PA Layer on Bare Support			LbL ₃₀ on PVA-primed Support
		LbL ₁₀	LbL ₃₀	LbL ₅₀	
Water Permeance [L/m ² h – bar]	497	150	19	9	0.23
Salt Permeance [m/s]	2.4x10 ⁻³	1.3x10 ⁻²	6.9x10 ⁻⁴	5.5x10 ⁻⁵	1.6x10 ⁻⁷
Salt Rejection [%]	9.3	5	10	44	88.3

B.3. Dependence of the Overall Water Permeance on the Number of LbL Cycles

An overview of the series resistance model for water has been done in Chapter 3 and following section with discuss the analysis for determining the dependence of overall water permeance on the number of LbL cycles. If no primer is applied (i.e., the PA layer is deposited directly onto the microporous support), then it may be reasonable to set $A_{overall} = A_x$ provided that the resistance to water transport through the microporous support is negligible compared to that of the PA layer. The water permeance, A_x , of the PA layer depends on the number of LbL cycles, the PA layer growth rate, and the effective water permeability of the PA layer as:¹¹

$$A_x = \left(\frac{\bar{V}_w}{R_g T r} P_{w,x} \right) x^{-1} \quad (\text{B1})$$

Equation B1 can be linearized as:

$$\log[A_x] = \log \left[\frac{\bar{V}_w}{R_g T r} P_{w,x} \right] - \log[x] \quad (\text{B2})$$

Equation B2 is based on the constitutive equation for water flux through the PA layer (Equation 2 in Chapter 3) and the relationship between the PA layer water permeance and the thickness of the PA layer (Equation 6 in Chapter 3). Therefore, if the effective water permeability of the PA layer is a constant (i.e., is intrinsic to the polymer structure of the layer), the water permeance should scale according to Equation B2. Alternatively, deviations from the scaling relationship in Equation B2 could suggest defect formation in the PA layer for membranes prepared without the PVA primer (Figure B2). In Figure B2, the red line (slope = -1) was extrapolated from the LbL membrane prepared using 50 cycles (LbL₅₀) on the bare support (i.e., no PVA primer was used).

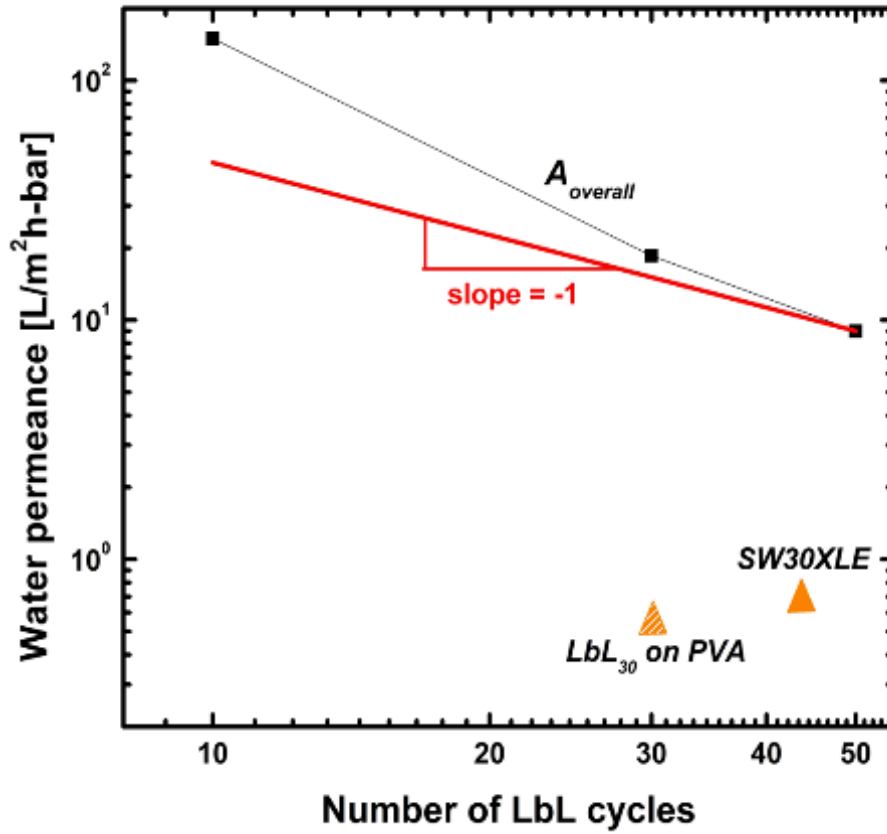


Figure B2: Overall water permeance data, as a function of the number of LbL cycles, for LbL membranes prepared without using the PVA primer (■) and an LbL membrane prepared by completing 30 PA deposition cycles on a PVA-primed support (LbL₃₀). The horizontal position of the commercially available SW30XLE membrane was determined by estimating the PA layer thickness of the membrane and calculating an equivalent number of LbL cycles using the growth rate data reported in Figure 2 of Chapter 5.

To perform a similar analysis on the PVA-primed support PA-TFCs, Equations 3-6 from Chapter 3 were combined to obtain an expression for the dependence of $(A_{overall})^{-1}$ on the number of LbL cycles:

$$\frac{A_0}{A_{overall}} = 1 + \frac{P_{w,0} r}{P_{w,x} h_0} x = 1 + m_1 x \quad (B3)$$

which can be linearized as:

$$\log(A_{overall}) = \log\left(\frac{A_0}{1 + \frac{P_{w,0} r}{P_{w,x} h_0} x}\right) = \log\left(\frac{A_0}{1 + m_1 x}\right) \quad (B4)$$

Equation B4 can be used to predict the dependence of $A_{overall}$ on the number of LbL cycles, which is useful for determining the contribution of the PVA layer to the overall resistance to water transport.

B.4. Analysis of Relative Mass Transfer Resistances (Water Transport)

To better understand the relationship between the overall resistance to water transport, $A_{overall}$, and that of the LbL formed PA layer, the contribution of the additional PVA primer layer to the overall water permeance must be determined. By employing the resistance in series model outlined above, we can use the deviation between the PA layer water permeance, A_x , and the overall water permeance, $A_{overall}$, to determine the contribution of the PVA primer to the overall mass transfer resistance of the membrane (i.e., if $A_{overall} = A_x$ then the PVA primer layer does not contribute meaningfully to the overall resistance to water transport). Using LbL₃₀ PA-TFC water permeance data, m_1 (Equation B4) was determined and used to predict J_w and subsequent $A_{overall}$ values for varied LbL cycle numbers. The predicted PVA-primed PA-TFC data were fit to both Equation B2 (bare support/limiting case PA-TFC model) and Equation B4 (PVA-primed PA-TFC model) to confirm that $A_{overall}$ is mostly dictated by the dependence on LbL cycles rather than the PVA primer layer (Figure B3).

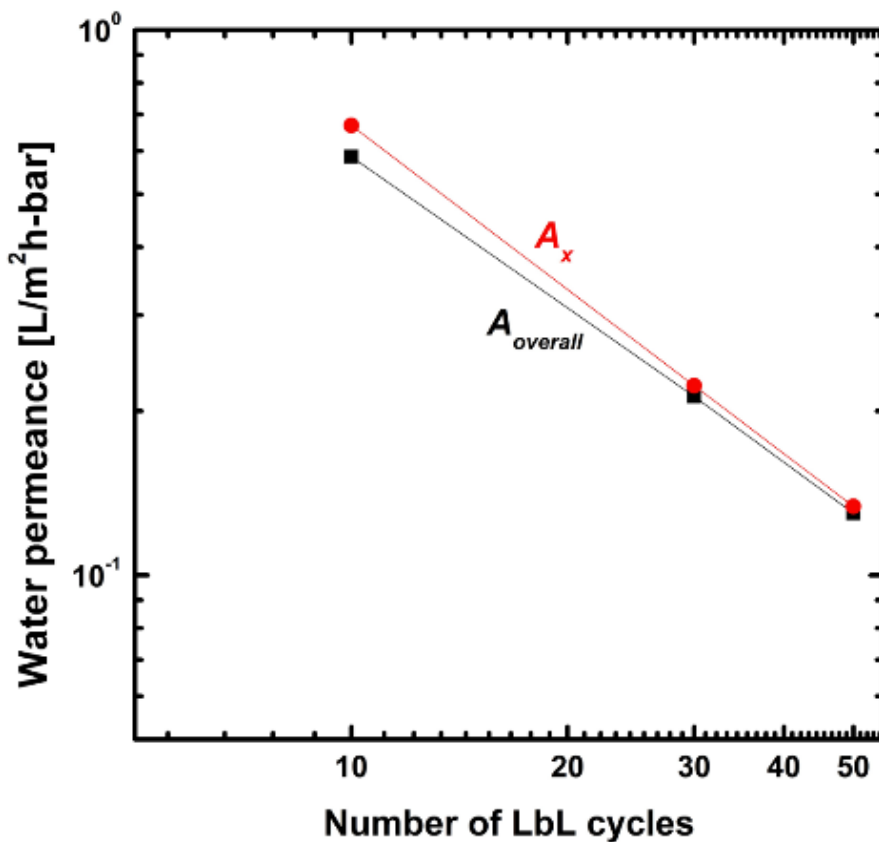


Figure B3: Water permeance versus the number of LbL cycles predicted for PVA-primed LbL PA-TFCs using the full resistance-in-series model ($A_{overall}$) and the limiting case (A_x). $A_{overall}$ and A_x are used to respectively define the appropriate water permeance indicator for the membrane system where, in the limiting case, the two are equal and the entire resistance to water transport is assumed to be due to the PA layer.

To determine the contribution of the PVA layer to $A_{overall}$, the metric $A_x/A_{overall}$ was determined for the LbL₃₀ PA-TFC membrane. If $A_x/A_{overall}$ equals unity, then the overall water permeance of the composite membrane is equivalent to that of the PA layer. In other words, deviations from $A_x/A_{overall} = 1$ suggest that the PVA primer layer contributes non-negligible mass transfer resistance to the overall composite membrane.¹¹ The water permeance of the 288 nm spin coated layer of PVA primer layer was measured to be $A_0 = 497 \text{ L/m}^2\text{h} - \text{bar}$. When $x = 30$ cycles of the LbL process was used to deposit a PA layer on the surface of a PVA-primed support membrane (i.e. LbL₃₀ on the PVA-primed support), the water permeance of the composite

membrane was measured to be $A_{overall} = 0.23 \text{ L/m}^2\text{h} - \text{bar}$. Using these values in Equation B4 results in $A_{30} = 0.23 \text{ L/m}^2\text{h} - \text{bar}$. As these values are equal it is reasonable to state that in this system the PA layer mass transfer resistance dominates that of the overall composite membrane. This analysis suggests that it is reasonable to apply the limiting case PA-TFC model to PVA-primed PA-TFCs made using LbL as the PVA primer layer does not contribute significantly to the overall resistance to water transport.

Using this framework and the experimentally measured $A_{overall}$ value, the water permeance corresponding to a PVA layer that would contribute no more than 5% to the overall water permeance (i.e. the ratio $A_x/A_{overall}$ would not exceed 1.05) was determined. This value is called $A_{0,min}$. To determine the corresponding maximum PVA layer thickness to obtain $A_{0,min}$, Equation B5 was solved using $A_{0,min}$. As there is an indirect relationship between A_0 and h_0 (Equation 5 from Chapter 3), the fixed product of $A_0 h_0$ and known $A_{0,min}$ can be used to solve for $h_{0,max}$ as:

$$A_0 h_0 = \frac{V_w P_{w,0}}{RT} \approx A_{0,min} h_{0,max} \quad (\text{B5})$$

where $P_{w,0}$ is assumed to be constant. The calculated values are summarized in Table B3.

Table B3: Analysis of the contribution of the PVA layer to the overall resistance to water transport using a LbL₃₀ on PVA-primed support membrane.

PVA Layer Thickness	A_0 [L/m ² h – bar]	$A_x/A_{overall}$
288 nm (h_0)	497	1.003
4000 nm ($h_{0,max}$)	35	1.05

B.5. Analysis of Relative Mass Transfer Resistances (Salt Transport)

Similar to water transport, the resistance in series model for salt transport is outlined in Chapter 3. As the salt rejection depends on both the resistance to water transport and salt transport, B_0 can be calculated based on experimentally measured salt rejection ($R_0 = 9.3\%$) and water

permeance ($A_0 = 497 \text{ L/m}^2\text{h} - \text{bar}$) data for the 288 nm PVA-primed PES support using Equation B5 as $2.4 \times 10^{-3} \text{ m/s}$. This value is approximately 4 orders of magnitude larger than the expected $\sim 10^{-7} \text{ m/s}$ value for commercial PA-TFCs. A similar PVA layer resistance contribution analysis was not performed for salt transport as it is reasonable to assume that a similar, if not smaller, contribution to the overall resistance to transport for the PVA layer would be observed for salt due to the larger size of hydrated ions as compared to water molecules.

Experimentally measured $A_{overall}$ and R_s data were used to calculate $B_{overall}$ using Equation 11 in Chapter 3. Similarly, B_0 was determined from data measured using the PVA-primed support. These salt permeance values were used to calculate the salt permeance of the PA layer, B_x (or B_{30} for 30 LbL cycles), using the series resistance model (Equation 8 in Chapter 3).

The calculated value of B_{30} was used along with the measured value of A_{30} to calculate a salt rejection value, $R_{s,30}$, using Equation B15 that results solely from PA layer permeance values. This salt rejection value was calculated to be $R_{s,30} = 90.4\%$. Notably, this value is within nearly 2% of the experimentally measured salt rejection value for the entire membrane ($R_s = 88.3\%$). This comparison suggests that nearly all of the mass transfer resistance to salt transport occurs in the PA layer, which is consistent with the use of PA layers as the selective salt rejecting layer in desalination membranes.

B.6. References

1. Chan EP, Lee JH, Chung JY, Stafford CM. *Rev Sci Instrum.* 2012;83(11) 114102.
2. Geise GM, Lee H-S, Miller DJ, Freeman BD, McGrath JE, Paul DR. *J Polym Sci Part B Polym Phys.* 2010;48:1685-1711.
3. Kong C, Shintani T, Kamada T, Freger V, Tsuru T. *J Membr Sci.* 2011;384(1-2):10-16.
4. Saha NK, Joshi S V. *J Membr Sci.* 2009;342(1-2):60-69.
5. Ghosh AK, Jeong BH, Huang X, Hoek EMV. *J Membr Sci.* 2008;311(1-2):34-45.
6. Johnson PM, Yoon J, Kelly JY, Howarter JA, Stafford CM. Molecular layer-by-layer

- deposition of highly crosslinked polyamide films. *J Polym Sci Part B Polym Phys*. 2012;50(3):168-173.
7. Chowdhury MR, Steffes J, Huey BD, McCutcheon JR. 2018;361(6403):682-686.
 8. Mavukkandy MO, McBride SA, Warsinger DM, Dizge N, Hasan SW, Arafat HA. *J Membr Sci*. doi: 10.1016/j.memsci.2020.118258
 9. Hermans S, Bernstein R, Volodin A, Vankelecom IFJ. *React Funct Polym*. 2015;86:199-208.
 10. Gu JE, Lee S, Stafford CM, Lee JS, Choi W, Kim BY, Baek KY, Chan EP, Chung JY, Bang J, Lee JH. *Adv Mater*. 2013;25(34):4778-4782.
 11. Choi W, Gu JE, Park SH, Kim S, Bang J, Baek KY, Park B, Lee JS, Chan EP, Lee JH. *ACS Nano*. 2015;9(1):345-355.

Appendix C: Supporting Information for Chapter 6

C.1. Determining the MOF Loading in wt% via TGA

Figure C1 shows the raw TGA scan for our PA coated PVA membranes made from varying MOF solution concentration. Samples of PA-coated PVA were used in place of the PA-TFN membranes discussed later to better isolate the MOF-containing PA layer from the greater composite membrane structure.

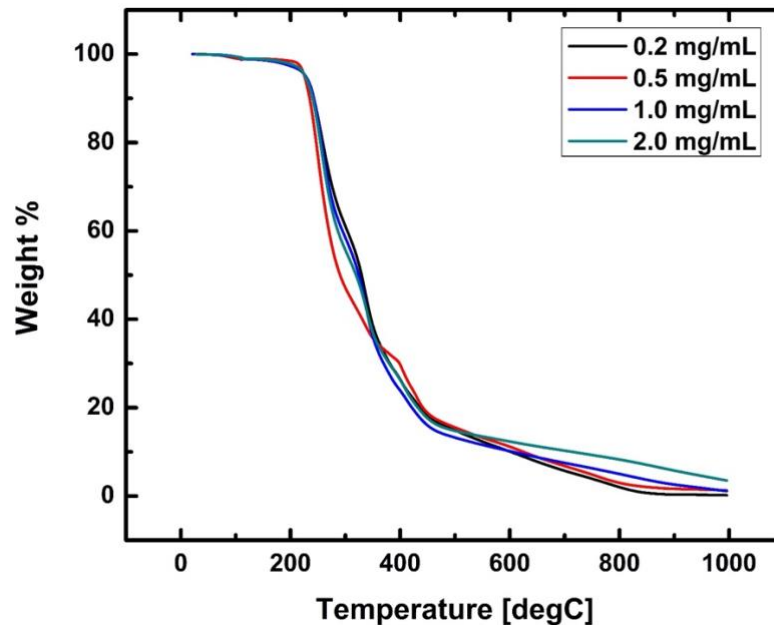


Figure C.1: TGA scans for UiO66-NH₂-containing PA layers deposited to PVA supports. Samples of ranging MOF solution concentration (0.2 mg/mL, 0.5 mg/mL, 1 mg/mL, 2 mg/mL) were tested from 25 C – 1000 C.

Since all organics are expected to have decomposed by the final scan temperature (1000 C), the final amount sample mass was used to determine the MOF loading at each MOF solution concentration using the relationship in Equation C1.

$$MOF \text{ Loading [wt\%]} = \frac{x [mg] \times 0.32}{Total \text{ Sample Mass [mg]}} \times 100 \quad (C1)$$

The final weight of the sample at 1000 C is represented as x and assumed to correspond to zinc present in UiO66-NH₂. It is important to note that the final sample weight is scaled by the final weight % of a UiO66-NH₂ TGA scan (32 wt%) to ensure we are similarly considering only the remaining zinc in the MOF as an indicator of the loading in the PA layer. The corresponding MOF loadings (wt%) at each MOF solution concentration (mg/mL) are shown in Table 1 in Chapter 6.

C.2. Data Summary

Water and solute transport data are summarized in Table C1. Water permeance, A , and solute rejection, R , data were measured as described in the materials and methods section of in Chapter 4. Solute permeance, B , data were calculated from the measured A and R data using Equation 4 and 6, for salt and dyes respectively, in Chapter 4.

Table C.1: Water and solute transport data summary for PA-TFN- 1.12 wt% UiO66-NH₂

	Water Permeance [L/m ² h – bar]	Solute Permeance [cm/s]				Solute Rejection [%]			
		MgSO ₄	Methyl Orange	Methylene Blue	Congo Red	MgSO ₄	Methyl Orange	Methylene Blue	Congo Red
PVA-Primed Support	497	2.23	0.37	4.22×10^{-2}	3.21×10^{-4}	0.89	3.63	21	93
PA-TFCM (no UiO66-NH ₂)	0.14	7.85×10^{-6}	2.77×10^{-5}	3.64×10^{-5}	5.14×10^{-6}	90	86	82	97
PA-TFNM (1.12 wt% UiO66-NH ₂)	0.64	4.65×10^{-4}	5.54×10^{-5}	2.83×10^{-4}	2.48×10^{-6}	52	85	54	99

C.3. Series Resistance Model for Water Transport

The series resistance model for water transport in LbL-made composite membranes is described in Chapter 4 (Equations 1-7). To determine if it can be applied to PA-TFN membranes made via LbL “sandwiched” synthesis, the PA layer specific resistance to water transport, A_x^{-1} , is calculated via Equation 4 in Chapter 3 and known water permeance values for the PVA primed

support ($A_0 = 497 \text{ L/m}^2\text{h} - \text{bar}$), shown in Table C1, and the PA-TFN membrane ($A_{overall}$) shown in Figure 4 in Chapter 6. The corresponding PA layer specific water permeance (A_x) is then plotted and compared to the experimentally obtained PA-TFN membrane water permeance for varying MOF loading (Figure C1).

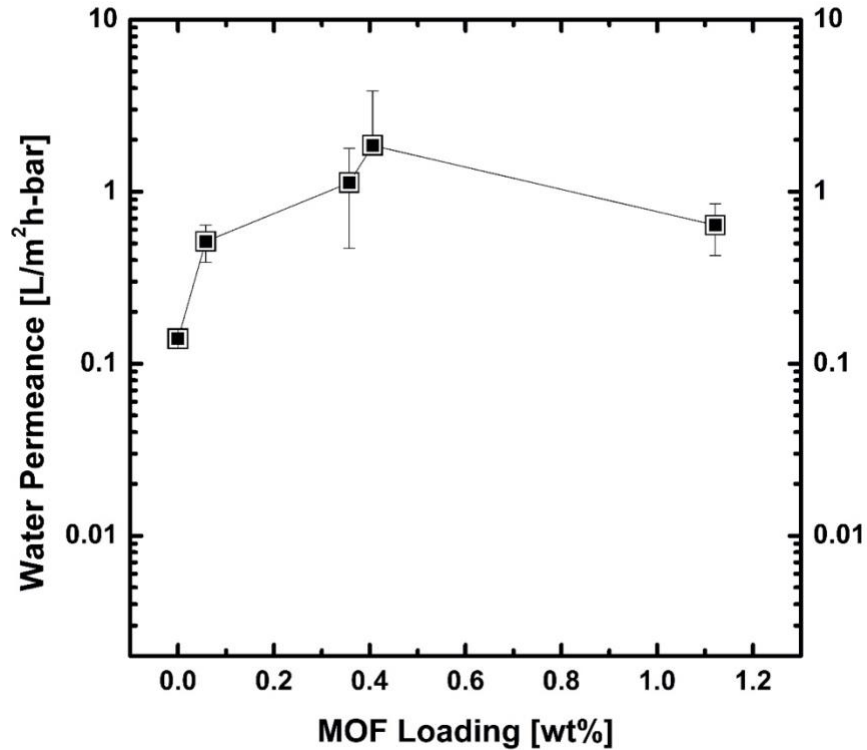


Figure C.2: Water permeance versus MOF loading (wt%) for composite membrane (filled black square) and PA layer (open black square) calculated using the resistance in series model described in Section C.3.

Figure C2 shows strong agreement between the PA layer specific water permeance (A_x) and the composite membrane water permeance ($A_{overall}$) suggested the experimentally obtained results provide a reasonable estimation of the PA layer specific water transport. This analysis was extended to dye solution water permeance for the highest MOF loading tested to ascertain if a similar agreement could be observed. Figure C3 shows that even in the dye solution system, the water permeance observed experimentally for the composite membrane is approximately equal to that of the individual PA layer. It is important to note that the resistance to mass transfer of

water is the only system explored in this study. This is because it has been shown in prior literature that the small deviation between PA layer and composite membrane resistances to mass transfer would translate into similar, if not smaller, situation with regard to salt and dye transport as hydrated ions and organic dyes are much larger than water molecules.¹

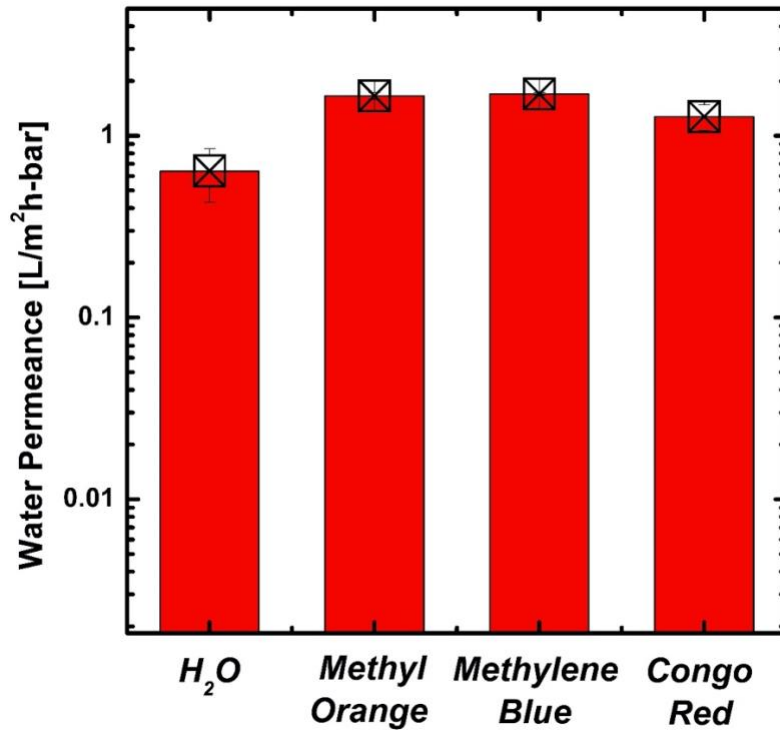


Figure C.3: Water permeance data for PA-TFN- 1.12 wt% UiO66-NH₂ for different solutes for the composite membrane (red bars) and PA layer (open black squares) calculated using the resistance in series model described in Section C.3

C.4. Determination of PVA Layer Contribution to Resistance to Water Transport

The contribution of the PVA layer to the overall mass transfer resistance to water was determined by comparing resistance to water transport of the PVA layer (A_0^{-1}) to the resistance to water transport for the composite membrane ($A_{overall}^{-1}$). Using the experimentally determined water permeance for the composite membranes (Figure 4 in Chapter 6) and PVA-primed support (Table C1) the ratio of the resistances to mass transfer of the PVA layer and the composite membrane ($A_0^{-1}/A_{overall}^{-1}$) were plotted in terms of percentage contribution to the overall

resistance to water transport (Figure C4). These values were compared to a cap of 5% contribution (i.e. the ratio $A_0^{-1}/A_{overall}^{-1}$ would not exceed 0.05) corresponding to a framework discussed elsewhere.¹

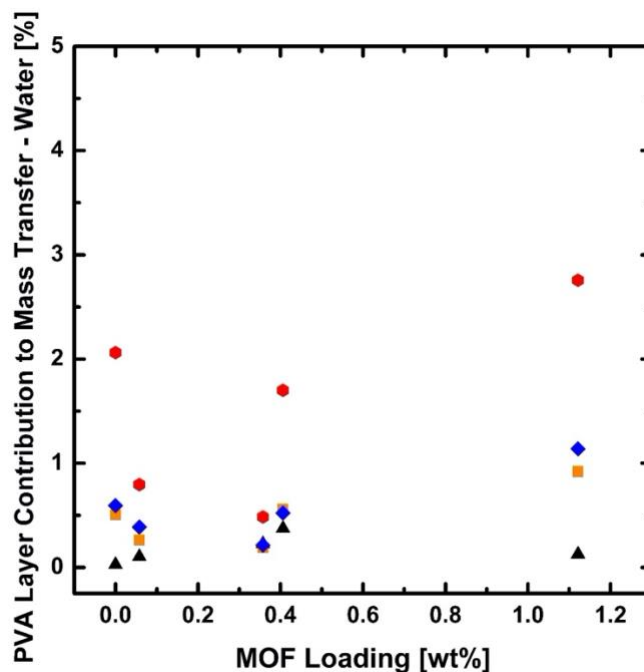


Figure C.4: PVA layer contribution to resistance to mass transport for water with varying MOF loading in weight%, calculated from the resistance in series model as described in Section C.4. Values for different solutes of interest are as follows: MgSO₄ (black triangles), methyl orange (orange square), methylene blue (blue diamond), congo red (red hexagon).

C.5. References

- (1) Agata, W.-A. S.; Thompson, J.; Geise, G. M. Layer-by-Layer Approach to Enable Polyamide Formation on Microporous Supports for Thin-Film Composite Membranes. *J. Appl. Polym. Sci.* n/a (n/a), 51201. <https://doi.org/https://doi.org/10.1002/app.51201>.

Vita

Saring Agata graduated from Phillips Exeter Academy (Exeter, NH) in 2012. Subsequently, Saring attended Columbia University, where she majored in Chemical Engineering and earned a Bachelor of Science in this field. Directly following her time at Columbia, Saring enrolled at the University of Virginia to pursue a Ph.D. in Chemical Engineering under the guidance of Prof. Geoffrey M. Geise. In 2019, Saring earned both a full endowed PhD fellowship from the National GEM Consortium as well as the UVA Engineering Sture G Olsson fellowship for excellent research and impact on the school of Engineering. Saring proceeded to earn her Doctor of Philosophy degree in Chemical Engineering in August of 2021.

Permanent email address: wsa2108@gmail.com

This dissertation was typed by Saring Agata